A quantum dot in a microcavity as a bright source of coherent single photons

Inauguraldissertation
zur
Erlangung der Würde eines Doktors der Philosophie
vorgelegt der
Philosophisch-Naturwissenschaftlichen Fakultät
der Universität Basel

von

Natasha Tomm

2021

Genehmigt von der Philosophisch-Naturwissenschaftlichen Fakultät
auf Antrag von

Prof. Dr. Richard J. Warburton

Prof. Dr. Philipp Treutlein

Asst. Prof. Dr. Wolfgang Löffler

Basel, den 22. Juni 2021

Prof. Dr. Marcel Mayor
Dekan

We can easily forgive a child
who is afraid of the dark.
The real tragedy of life
is when men are afraid of the light.

- Plato

PREFACE

As we advance into the “quantum era”, the development of processors able to efficiently simulate and compute complicated problems using fundamental quantum physics laws progresses speedily. Two common approaches for quantum information processing rely on either discrete *qubits* (the building blocks of a quantum processor) or dense *continuous variable* computing. Not only computing quantum information is important, but also establishing a communication channel between remote quantum processors is necessary. The networking packet must itself be quantum. This suggests employing elementary particles of light – photons – for quantum communication and networking, as nothing travels faster than the speed of light.

Single photons themselves can also be manipulated at ultra fast tempo to perform quantum algorithms. Contrarily to their localized counterparts, photons make for resilient qubits. Photons do not interact with other photons, and are not susceptible to decoherence resulting from electromagnetic or thermal noise. Millions of single photons can be produced per second, making possible their efficient implementation in gate operations and parallel processing using linear optics setups. These properties make them ideal candidates for applications in quantum communication and quantum information processing.

All these applications require, however, a source of single photons with ideal properties. The source should be on-demand, i.e. produce one single photon for every trigger event with very high – ideally 100% – probability. No other states of light should be created: the states should be pure single photon Fock-states. All photons emitted by the source should have exactly the same characteristics: they should be indistinguishable from one another. Finally, this technology should be scalable. These requirements are technically challenging to meet.

This thesis describes the experimental realization of a new platform for efficiently generating single photons with ideal properties. This work presents the record-efficiency single photon source to-date, and a detailed study of the important technical parameters necessary for this technological achievement. The document is strongly based on the publications resulting from this project.

In Chapter 1, an introduction to this thesis is presented, starting with the motivation for this work. The relevant physics and technical concepts that act as a foundation for this project are discussed. Alternative technologies and implementations of single photon sources are presented, acting as a comparative measure for our own results.

Chapter 2 discusses the technical parameters, important for designing a device able to produce single photons rapidly and on demand. We employ gated semiconductor quantum dots coupled to an open-access optical microcavity. The microcavity is formed by a ultra-low loss semiconductor mirror and a dielectric mirror, with optimized losses for maximum quantum efficiency of the system. The microcavity is characterized, yielding experimentally the expected optical properties. The experimental setup and optical microscope employed in the main experiments throughout this work are disclosed. The concepts of the single photon purity and indistinguishability are introduced, with a representation on how to measure and deduce them from experiments. Finally, an estimate on the possible end-to-end efficiency of the single photon source is calculated from all the designed and characterized parameters in the device.

In Chapter 3 the excitation mechanism of a two-level system mediated by a cavity with non-degenerate polarized modes is elucidated. In this work, we exploit a circular/cyclic transition in the quantum dot and couple it to a linearly polarized cavity mode. We excite the transition by launching short pulses of light via a detuned cavity mode, with orthogonal polarization. In this scheme the detuned cavity acts as a dispersive filter on the laser pulse, modifying its spectral components, and making the excitation mechanism non-trivial. We show that a near-unity population inversion can be achieved if the input laser is optimally detuned from the resonant frequency, and the influence of phonon-induced dephasing on the process.

Chapter 4 discusses the effect of optical losses at the surface of the gated semiconductor heterostructure. A highly reflective semiconductor distributed Bragg reflector (DBR) containing a gated region near the surface is combined with a highly reflective dielectric DBR. An ultra high $\mathcal{Q}$-factor cavity is expected from such assembly. In reality, modest values of $\mathcal{Q}$-factor, about 15 times smaller than expected, are measured near the stopband center of the semiconductor DBR. We use the open-access cavity as a sensor to probe the wavelength dependence of the $\mathcal{Q}$-factor. This analysis indicates an exponential dependence of the losses as a function of wavelength, indicating a Franz-Keldysh-like absorption, a consequence of surface charge states. A method to passivate the surface is developed and implemented. After passivation the measured $\mathcal{Q}$-factors correspond to the design values, apart from a small contribution from scattering losses, due to intrinsic surface roughness. The passivation layer is shown to have a dual role: extinguishing optical losses due to Frank-Keldysh-like absorption, and mitigating the scattering losses due to roughness. This result is essential to achieve high-quality low-loss semiconductor mirrors for applications, such as the efficient single photon source central to this thesis.

In Chapter 5, the experimental realization of a highly efficient single photon source is presented. The device envisioned and constructed in the previous chapters is experimentally tested. The tunability of the system allows for an individual characterization of the relevant parameters: the single-photon emission into the cavity mode β, and the extraction efficiency of the cavity η_{out}, which correspond to the designed values. Using a pulsed excitation laser, one observes Rabi oscillations. A record high end-to-end efficiency in single photon sources is achieved, presenting optimal single photon purity and indistinguishability of successively emitted photons. This work is also novel in achieving a maintained coherence of the system for unprecedented timescales, while generating single photons at MHz rates.

Finally, in Chapter 6 we investigate the mode-splitting of the fundamental resonances in a semiconductor optical cavity. Employing a microcavity formed by a high-reflectivity dielectric DBR and a semiconductor DBR assembled on top of a strain-piezo, we inquire the effect of uniaxial stress onto an induced birefringence in the semiconductor heterostructure. The microcavity functions as a sensor for the intrinsic crystal birefringence across a large spectral range. The photoluminescence of quantum dots embedded in the sample is used to gauge the absolute stress induced in the material. The dispersive behavior of the stress-induced birefringence allows for a quantitative description of the photoelastic effect in the sample. The control over the cavity's mode-splitting is essential for applications in cavity quantum electrodynamic experiments. For instance, in sources of polarized single photons, increasing the mode-splitting aids higher efficiencies. On the other hand, experiments relying on circularly polarized excitation schemes benefit of having degenerate linearly polarized modes.

We conclude this work in Chapter 7 by discussing prospects and further improvements for the presented single photon source, as well as presenting perspectives for future directions.

Contents

1

INTRODUCTION

"Nature isn't classical, dammit, and if you want to make a simulation of nature, you'd better make it quantum mechanical, and by golly it's a wonderful problem, because it doesn't look so easy"

- R. P. Feynman

At the beginning of the 20th century the first formulations of the quantum mechanical theory arose. The concept that nature organizes itself microscopically in a quantized indivisible manner led (and still leads) humanity not only to understanding fundamental processes in nature, but also to the development of technologies that have changed the world. About half a century later, with the development of the first transistors, the first digital technologies made way for the "information age". By the 1980s, a variety of quantum-related technologies had already touched, directly or indirectly, the lives of every human being on Earth. Around the same time, Richard Feynman proposed that, in order to compute or simulate nature, we need a computer that behaves the same way nature does,[1] otherwise finding a solution becomes an impossible task in a finite amount of time. In order to solve a classical-world problem with an n-dimensional space, n classical binary bits (which can be deterministically in either a 0 or 1 state at a given time) are necessary[i]. The quantum counterpart requires a search in a 2^n-dimensional space.[2] A discrete quantum bit (qubit) can be in a coherent superposition of both states, $|\Psi\rangle = \alpha\,|0\rangle + \beta\,|1\rangle$, where $|\alpha|^2$ and $|\beta|^2$ dictate the probability of measuring one or the other configuration. This inherent property is exactly what Feynman was searching for.

Fast forward to the present day, the implementation of qubits in a variety of quantum physical systems has been successfully achieved. A variety of two-level systems can be employed as qubits: a single spin which is either in a spin-up or spin-down configuration;[3] a charged particle (an electron or a hole) trapped in

---

[i] This is valid for a generic classical processor or computer implementing binary system

a double potential, like a double quantum dot – the charge is localized in either right or left potential minimum –;[3,4] an atom or ion that is in its ground or excited state, containing or not an extra charge;[5,6] a superconducting circuit encoding information in the directionality of the current flow;[7] or a photon that encodes its state in its polarization, color or time of arrival.[8] To this day, quantum advantage, defined as the ability of a quantum processor to solve a problem that no classical processor can solve in a feasible amount of time,[9] has been arguably demonstrated with superconducting[10] qubits[ii] and, more recently, with photons.[11]

Although many physical systems can be employed for quantum processing itself, the most obvious candidate to transport quantum information between remote processors is an optical photon. By nature, photons are the fastest traveling entity in the universe, moving at the speed of light. Due to their bosonic nature, photons are non-interacting among themselves, and they are weakly susceptible to environmental noise and losses. Encoding information in one of these quantum particles is relatively easy. The technology employed to manipulate these quantum particles is classical – lenses, mirrors, beam-splitters –, and they can be operated at room-temperature. Finally, photons are optimal entities to mediate interactions with other quantum nodes such as atoms,[12] ions,[5,13] color centers in crystals,[14,15] quantum dots,[8,16,17] and optomechanical systems.[18,19] In conclusion, single photons are arguably the best platform for networking remote quantum processors, they can be used themselves for discrete quantum information processing or as intermediaries in quantum gates[iii].

Given these advantages, a source that creates single photons on demand is of crucial interest.[8] This means that upon a trigger signal, the device should produce one (and only one) photon; if there is no trigger, no photon should be produced. The characteristic time associated with the emission of a photon, together with its emission probability, defines the source's *brightness.* Ideally, one would want to produce single photons with a very high repetition rate – higher than GHz – and in a deterministic fashion (with 100% probability). This goal is technologically very challenging to achieve. Furthermore, the source should have a high *single photon purity,* i.e. it should emit only single photon Fock-states. Finally, all consecutive photons emitted by the source should be completely identical to one another in color, wavepacket overlap

---

[ii] There has been debates whether this result configures true quantum advantage, or whether a classical super-computer could solve the proposed problem in a few days. A conclusive answer has not been reached.

[iii] Another technique for efficient quantum information processing proposed in 1999 is the one of *continuous variable quantum computing*, which relies on dense quantum modes, rather than discrete qubits. The focus of the discussion presented in this thesis is that of discrete qubit quantum computing.

and polarization: this is characterized by the single photon *indistinguishability*, quantified by the two-photon, or Hong-Ou-Mandel (HOM), interference visibility.[20] These properties are used to characterize a single photon source, achievable at different degrees for different technologies.

Up to this date, the first most commonly used technique to create single photons for commercial applications is to highly attenuate a laser beam, until there is a very small probability of having any photon-number larger than $|1\rangle$ going through the system. The clear downside of this method is that this is obtained at the cost of also highly diminishing the single-photon probability, limiting the efficiency to a few percent. Furthermore, the statistical properties of the output beam remain that of a coherent state, and therefore with classical characteristics.

The second most employed technique relies on spontaneous parametric down-conversion (SPDC), where an input laser beam is down-converted into two beams by a non-linear crystal. The detection of a photon in one of the beams heralds the presence of another single photon in the opposite beam. Sources relying on SPDC present high photon indistinguishability, with Hong-Ou-Mandel visibilities in the order of $\sim 95\%$.[21] The drawback is that the photon creation process is non-deterministic, and there is a trade-off in the process between single photon purity and efficiency. One can compensate the probabilistic process by multiplexing the heralded photons, increasing considerably the single photon source efficiency.[22] Still, the repetition rate at which such sources can be operated is limited by the multiplexing rate.

1.1 An artificial atom as a source of single photons

Any two-level system with an active optical transition between a ground state $|g\rangle$ and an excited state $|e\rangle$ is a natural source of single photons. Assuming that this two-level system is initially in the excited state, it will decay back to its ground state by spontaneously emitting a photon with an energy corresponding to the energy difference between $|e\rangle$ and $|g\rangle$, with respective photon frequency ω_0. This process, which can also be assisted by phonns or by a non-radiative decay channel, happens at a radiative decay rate γ. This rate is given by *Fermi's golden rule*,[23] and is therefore proportional to the density of states. If the decay rate of the two-level system is given by the inverse of the radiative lifetime τ_{rad}, it is said to be "transform limited":

$$\gamma = \frac{1}{\tau_{\text{rad}}} = \frac{n\omega_0^3}{3\pi\varepsilon_0\hbar c^3} \cdot \mu^2, \tag{1.1}$$

where n is the refractive index of the bulk medium the two-level atom is embedded in, ε_0 is the vacuum's electric permittivity, $\hbar$ is the reduced Planck's constant, c is the speed of light in vacuum, and μ is the optical transition's dipole moment. In a bulk medium photons are emitted into a continuum of modes; the optical power is dissipated following the emission pattern of an electrical dipole, with a density of photonic modes proportional to the frequency squared, ω_0^2, in free space.

Atoms[12, 24] and ions[13, 25] are examples of two-level emitters which are commonly used as sources of single photons. They are however challenging to single-out, trap and retain. The need for laser cooling and the additional preparation steps also add extra time and resource overheads. A notable feature of such systems is their long-lived transitions, generally making their wave-packet duration in the micro-second regime and limiting their single photon generation rate. Furthermore, timing jitter[iv] limits the HOM visibility to modest values[12, 13, 24, 25] below 80%.

Emitters in the solid-state are naturally trapped in space,[26] and behave as "artificial atoms". Semiconductor quantum dots (QDs) are nanometric islets of a smaller band-gap material within a material matrix with a larger band-gap energy. Figure 1.1a depicts a QD representative of the ones used in this thesis: a nanometric island of indium arsenide (InAs) is formed thanks to a strain-relaxation process during epitaxial growth of lattice-mismatched InAs over gallium arsenide (GaAs). The so-called Stranski-Krastanov[27] growth mechanism leaves behind a few monolayers of InAs (wetting layer) supporting the QDs. The latter are then capped with GaAs and planar, fully epitaxial growth, can resume.

Despite being formed by about 10^5 atomic nuclei, the ensemble behaves as a single atom with discrete atomic transitions,[16] as shown in Fig. 1.1b. A single electron in the conduction band and a single hole in the valence band form a bound electron-hole pair, an *exciton*, a representation of a two-level system. By embedding the QDs within a gated p-i-n diode structure (Fig. 1.1c), one can tunnel-couple the QD's energy levels to a Fermi reservoir, and deterministically load the QD with a number of charges via the Coulomb blockade effect, as schematically depicted in Fig. 1.1d. One can create not only a neutral exciton, so-called X^0, in an initially empty QD, but also negatively (positively) charged excitons X^{-N} (X^{+N}) if the QD hosts initially N extra electrons (holes).[16, 28, 29] Furthermore, the electric field between the gates in the diode can be modulated, allowing for a fine-tuning of the optical transition frequency in the QD via the DC quantum-confined Stark effect. Finally, QDs embedded in a gated heterostructure have been shown to present reduced noise compared to ungated

---

[iv] Usually, a cavity-enhanced Raman transition is employed to excite the atom or ion. The timing jitter arises from spontaneous emission back down to the initial state.

structures[30] leading to emission close to transform limited.[31] The low-noise environment is a keystone for the production of coherent single photons.

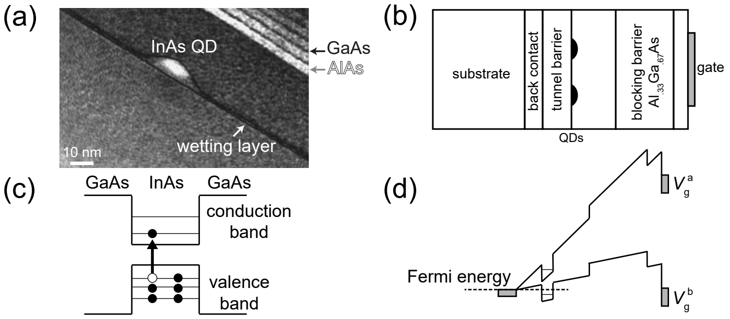

Figure 1.1: Self-assembled semiconductor quantum dots. (a) Dark-field transmission electron microscopy (TEM) image of a self-assembled InAs quantum dot embedded in a GaAs matrix. Layers of GaAs and AlAs form a short period super-lattice (SPS) above the quantum dot in the image, but can be grown with quarter-wave thicknesses to form a distributed Bragg reflector (DBR) below the quantum dots. Courtesy of Jean-Michel Chauveau and Arne Ludwig. (b) Energy level structure of an InAs QD in a GaAs matrix. Black dots represent electrons and white dot represents a hole. Upon excitation an electron is promoted to the conduction band and leaves a hole behind in the valence band; the bound electron-hole pair is called an exciton. (c) Semiconductor heterostructure comprising of a gated n-i-p diode with embedded QDs. (d) The conduction band edge is tuned upon application of two different voltages applied to the top gate of the heterostructure.

Contrarily to other solid-state emitters,[32–34] semiconductor QDs have large optical dipole moments ($\mu > 0.5\,\mathrm{nm} \cdot e$ in the infrared region of the spectrum[29,35]), very high[36] radiative efficiency $> 97\%$, and a relatively weak coupling to phonons, making them prominent candidates for efficient single photon sources. In the bulk semiconductor material, the QD emits single photons quasi-isotropically, and will hardly exit the high refractive index material due to total internal reflection at the interface with vacuum. Both the radiative decay rate and extraction of produced photons from the semiconductor material can be improved by placing these artificial atoms into nanophotonic structures such as photonic crystal cavities[36,37] and microcavities,[38–40] and exploiting the *Purcell effect*. These nanostructures act effectively as an optical cavity, enhancing the light-matter interaction.

1.2 Cavity-enhanced spontaneous emission

A cavity is a structure that confines the electromagnetic field into a small *mode volume* V. The confinement of the vacuum electric field E_{vac} modulates the local density of optical states. A Fabry-Perot resonator is a type of cavity consisting of two mirrors with reflectivities R_1 and R_2 separated by an effective distance L. Resonant light is confined between the two mirrors, eventually leaving the cavity with a decay rate given by[23,41]

$$\kappa = \frac{1}{\tau_{\mathrm{cav}}} = 2\pi \frac{c}{nL} \left(-\ln R_1 R_2\right) \simeq 2\pi \frac{c}{nL} \frac{1 - R_1 R_2}{\sqrt{R_1 R_2}}, \tag{1.2}$$

where τ_{cav} is the photon's lifetime in the cavity. The photon loss described by κ, the full-width at half maximum (FWHM) of the resonant mode of frequency ω_{cav}, is related to the cavity's *quality factor* $\mathcal{Q}$ via

$$\mathcal{Q} = \frac{\omega_{\mathrm{cav}}}{\kappa}. \tag{1.3}$$

When the QD and the cavity are in resonance, $\omega_{\mathrm{cav}} = \omega_0$, they couple with a *coherent coupling rate* g, given by

$$g = \frac{\mu E_{\mathrm{vac}}}{\hbar} = \sqrt{\frac{\omega_0}{2\hbar\varepsilon_0 n^2}} \cdot \frac{\mu}{\sqrt{V}}. \tag{1.4}$$

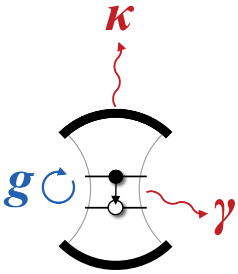

Figure 1.2: Two-level system in an optical cavity. The two-level system initially in the excited state decays, emitting a single photon, with a decay rate γ. The cavity supports a resonant optical mode that decays with a rate κ. When at resonance, the two-level system and the cavity couple with a coherent coupling rate g.

Figure 1.2 depicts the two-level system and cavity interaction, with the relevant parameters. In the weak-coupling regime, when it is not the case that $g \gg \kappa, \gamma$, the QD's spontaneous emission rate is enhanced by the Purcell factor

$$F_{\mathrm{P}} = \frac{4g^2}{\kappa\gamma}, \tag{1.5}$$

becoming $\Gamma = F_{\mathrm{P}} \cdot \gamma$. The probability that the QD (initially in the excited state) emits a photon into the optical mode defined by the cavity is given by the so-called β factor, $\beta = F_{\mathrm{P}}/(F_{\mathrm{P}} + 1)$. The cavity enhances the single photon spontaneous emission process and funnels the generated photons into the cavity mode. The photons finally exit the cavity with an extraction efficiency

$$\eta_{\mathrm{out}} = \frac{\kappa}{\kappa + \gamma}. \tag{1.6}$$

The overall quantum efficiency η, producing and collecting photons, is therefore given by the product[42] of β and η_{out}, i.e.

$$\eta = \frac{4g^2}{4g^2 + \kappa\gamma} \cdot \frac{\kappa}{\kappa + \gamma}. \tag{1.7}$$

For a QD in a Fabry-Perot type cavity, engineering γ and g is not always trivial. The most flexible parameter one can tailor in the system thus relates to the cavity decay rate κ. The maximal quantum efficiency for fixed γ and g is found at a condition $\kappa = 2g$. This relies on the assumption that, besides the intrinsic losses from the atom γ, the only loss channel in the system is the cavity itself.

The cavity itself has two loss channels, the two mirrors, via which the photons can escape. Ideally, one wishes to construct a system in which there is only one loss channel, via which the photons are collected. In order to construct such a system, one needs to minimize all other loss channels. In a real system, optical absorption and scattering at the surfaces of the device add up to undesired losses. The highly doped materials employed at the gates the p-i-n diode surrounding the QDs absorb light strongly, resulting in further losses.

If one assumes that the losses of the cavity are composed of two main channels, the optimal channel to be enhanced κ_{opt} (for instance the top mirror of a vertical cavity) and a second channel including all undesired losses κ_{loss}, then $\kappa = \kappa_{\mathrm{opt}} + \kappa_{\mathrm{loss}}$ and Eq. 1.7 becomes

$$\eta = \frac{4g^2}{4g^2 + (\kappa_{\mathrm{opt}} + \kappa_{\mathrm{loss}})\gamma} \cdot \frac{\kappa_{\mathrm{opt}}}{\kappa_{\mathrm{opt}} + \kappa_{\mathrm{loss}} + \gamma}. \tag{1.8}$$

For fixed γ, g and κ_{loss}, the quantum efficiency is a function of κ_{opt} and will be maximal by implementing a cavity design in which

$$\kappa_{\text{opt}} = \sqrt{(1 + \kappa_{\text{loss}}/\gamma)(4g^2 + \kappa_{\text{loss}}\gamma)}. \tag{1.9}$$

It is important to notice that κ_{loss} always results in a source of single photons with reduced efficiency: from Eq. 1.8 it is easy to see that $\eta \propto 1/(\kappa_{\text{opt}} + \kappa_{\text{loss}})$, and for any $\kappa_{\text{loss}} \geq 0$ we have $\frac{1}{\kappa_{\text{opt}}+\kappa_{\text{loss}}} \leq \frac{1}{\kappa_{\text{opt}}}$. Engineering the materials and the system in order to get rid of any undesired optical losses is an essential step to reach a near-deterministic single photon source.

1.3 Efficiently creating indistinguishable photons

In the solid-state, the quantum emitters couple their electronic states to the local environment. Noise caused by the nuclear spins,[30] fluctuating charges, and vibrational modes (phonons) in the matrix material lead to a reduced coherence in the QD's state.[43] In the case of QDs embedded in a diode structure, charge noise is highly suppressed.[30,31] The coupling of the QD to phononic modes however is more difficult to remedy and can have an impact in the properties of a single photon source.

The presence of high frequency phonons changes the excitation mechanism and can lower the inversion efficiency for a driven QD,[44,45] i.e. the probability Π of exciting the transition[v] can be less than unity. Lower frequency phonons also reduce the photon indistinguishability via two mechanisms: they induce the emission of photons detuned from the resonant transition, which are distinguishable from the resonantly-emitted photons; and they introduce dephasing in the QD's dipole moment, reducing the indistinguishability of consecutively emitted resonant photons.[43,46] Working in a high-Purcell-factor regime may help mitigate – but not eliminate – these effects, and a way of achieving unity indistinguishability is yet to be identified.

---

[v] The excitation of a two-level sytem can be understood as a π-rotation on the Bloch sphere from $|g\rangle$ to $|e\rangle$. In an ideal case, the path taken on the Bloch sphere to reach this rotation is a direct one, but it can be modified by a variety of factors.

1.4 Quantum information processing with optics

Achieving a near-ideal source of single photons brings us one step closer to fulfilling Richard Feynmann's aspiration. A *universal quantum computer* is a (yet hypothetical) physical system that is able to simulate *any* other quantum physical system in the universe. In general, a quantum computation involves three steps: initialization of a quantum system, some transformation or processing, and finally measurement or read-out stage. Quantum speedup compared to classical computing relies on circuits with initial states and operations based on quantum entanglement and quantum interference,[47] which are characterized by a negative *Wigner function*.[48] There are a few ways in which one can construct a universal quantum computer in the optical regime using linear-optical setups made up of a combination of beam-splitters, phase-shifters and photodetectors. One can, for instance use a remote quantum memory in combination with projective measurements;[49] or perform measurement-based processing, such as the *KLM protocol*[50][vi]. The latter requires feed-forward processing with fast readout detectors and active dynamical control of the optical elements in the setup. In order to move beyond the noise intermediate scale quantum computing limit, streams of consecutively entangled photons, so-called *cluster states*, are needed. Entangling single photons is itself not an ordinary task. The creation of an efficient source of cluster states is another step further in this journey.

There is, however, a class of problems that can be readily solved by employing an ideal single photon source, the class of *search and sampling*. A device designed for such kind of problems is not a universal quantum computer – it is not able to develop an answer to a question about any arbitrary physical system, but it is able to search or sample the probability distribution of a *specific* answer to the problem. In the photonic regime, such class of problems can be solved relying on quantum interference (instead of entangled photons), in a generalized HOM setup with M optical modes, instead of only two. Such a setup is schematically depicted in Fig. 1.3, and it is known as the *boson sampling* problem.[51] Similarly to one of the implementations of an optics-based universal quantum computer, the boson sampling problem is also based on a linear-optical setup. The fundamental difference is that this is a passive device. A stream of N single photons is launched into a linear optical setup with M (where $M \sim \mathcal{O}(N^2)$) optical modes to be probed by M photodetectors.[51] The setup itself contains $\mathcal{O}(M^2)$ optical elements (beam-splitters and phase-

---

[vi] For the KLM-protocol[50] the number of optical elements needed for each gate operation is at least 4 (for the simplest gate).

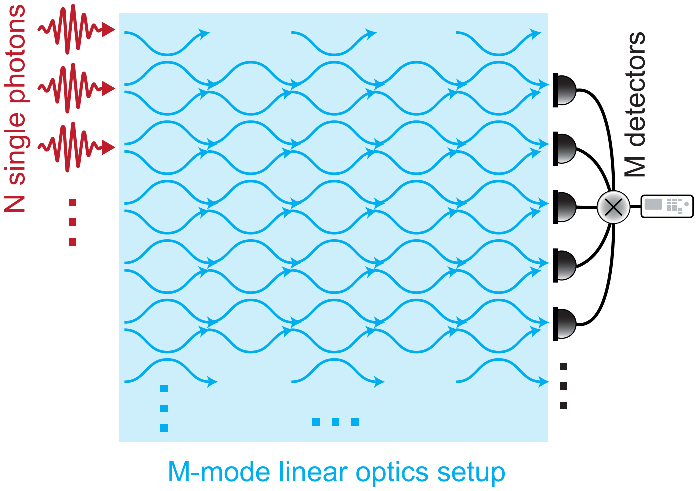

Figure 1.3: The problem of boson sampling. N indistinguishable single photons are launched into a linear-optical setup composed of beam-splitters and phase-shifters, representing a unitary transformation on the input. The photons will flow through the setup and interfere at each beam-splitter node, making each of the two output optical modes in the beam-splitter entangled. M photon-counting detectors sample the output modes.

shifters). Indistinguishable photons will undergo quantum interference at the beam-splitters and the output optical modes will be entangled. By selectively modifying the reflectivity at the beam-splitters and/or the polarization of the modes being probed, one can simulate different probability landscapes at the output of the device.

A variety of induced errors can disturb the quantum nature of the information processing in a linear-optics setup, and therefore make the output classically solvable[vii]. For the procedure to present a quantum speedup and not be able to be simulated in classical time, the initial state, the unitary transformations the initial state go through and the measurement must retain the negativity of the Wigner function.[47, 51, 53] If the input is classical or has a Gaussian probability distribution, the output state can always be simulated in polynomial time. Similarly for the measurement method: if it's a classical measurement, the input state and transformations operated on it do not matter, as what is measured is classical. It is not necessary that the unitary transformation performs a quantum operation. In fact, if both the input and the unitary transformation are quantum, there is still a chance that the output measured is classical, for

---

[vii] A computation of dimension n is said to be *classically solvable* if it is solvable in a polynomial time, $t(n) \propto n^k$. For certain classes of problems, the time complexity scales in exponential or factorial time, and are said to be not classically solvable problems.

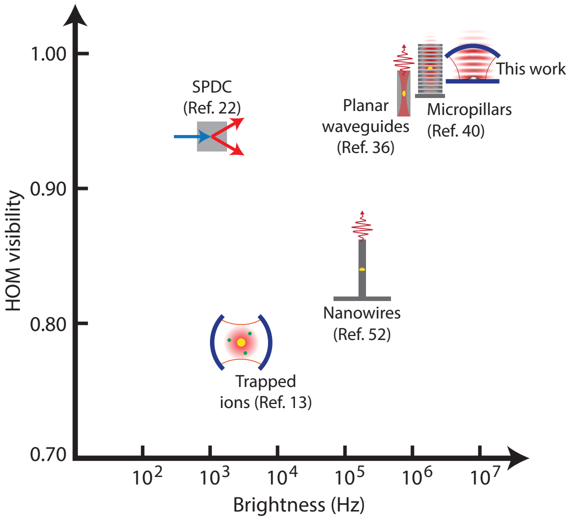

Figure 1.4: State-of-the-art single photon sources employing various nanophotonic structures.[13, 22, 36, 38, 40, 52] The plot outlines the different technologies as a function of source brightness (measured in single photons created per second) and HOM visibility.

example by taking as input *squeezed states of light* and letting the unitary transformation perform an anti-squeezing operation. If the input is quantum and the transformation is classical, which is the case for a linear-optical network, the probability distribution measured at the output can become intractable for classical computers for large systems, as long as the output retains its quantum character.

Of course, the transformation itself can be degraded due to losses and errors, in which case the output state can become classical. Specifically in the boson sampling algorithm, its quantum character is given by the interference of indistinguishable photons. The photons interacting throughout the setup must be “mode-matched”: they must be indistinguishable in color, polarization and time of arrival at each beam-splitter, otherwise it reduces to the classical light-beam interference case. If there are losses in the setup or in the input state, such that quantum interference is impaired, the output can be simulated classically. Overall in the boson sampling algorithm, the computation can be classically performed if the number of mode-mismatched photons reaching the photodetectors exceeds the number of mode-matched photons.[47, 53] For this reason, even for a perfect transformation (no losses and a perfect polarization matching) and measurement (photodetectors with 100% efficiency and zero dark-counts), a source of single photons with an efficiency of at least 50% is necessary, assuming these photons are perfectly indistinguishable.[47] The lower the indistinguishability between the input photons, the higher the requirements in terms of single photon production efficiency.[47] Figure 1.4 presents the state-of-the-art single photon sources sorted by brightness and indistinguishability. This work presents the realization of the first deterministic source of single photons to surpass the 50% efficiency threshold, paving the way to ideal single photon sources for quantum computing and quantum information processing.

2

TOWARDS AN IDEAL SINGLE PHOTON SOURCE: DESIGN AND PARAMETERS

Adapted from:

N. Tomm*, A. Javadi*, N. O. Antoniadis, D. Najer, M. C. Löbl, A. R. Korsch, R. Schott, S. R. Valentin, A. D. Wieck, A. Ludwig and R. J. Warburton,

“A bright and fast source of coherent single photons”,

Nature Nanotechnology **16**, 399 (2021)

2.1 Summary

The realization of a source of single photons with optimal properties is a challenging task. Quantum algorithm applications impose demanding prerequisites in terms of how rapidly and efficiently one can create and extract the photons from a source. Furthermore, the source should produce pure states, containing single photons only. Consecutively produced photons should be indistinguishable from one another. All these stipulations require a careful experimental design. Here, we the steps performed in designing and manufacturing a near-ideal single photon source are described. Single InAs quantum

dots are employed as a source of photons. An optical microcavity, optimally designed for maximum enhancement of photon production and extraction, is constructed and characterized. The single photons leave the microcavity in a Gaussian mode with a chosen linear polarization, and are collected into a single-mode fiber. A detailed description of the experimental conditions, including the optical microscope used to collect photons and the optical setups used to characterize the source, is provided. The properties of the collected photons are probed. A synchronous optimization of all material and setup parameters lead to a near-ideal single photon source.

2.2 Introduction

Semiconductor quantum dots (QD) can mimic the properties of a two-level system. When in the excited state, a QD can spontaneously decay back into its ground state emitting one single photon, with the energy equal to the fundamental energy gap. This process depends on the natural decay rate of the emitter γ is and non-directional. Spontaneous emission can be enhanced via the Purcell effect, if the QD is coupled (with a coupling rate g) to a resonant microcavity. The microcavity has a second role: to create a preferential escape channel for the emitted photons, acting as a “funnel” to collect them. The rate at which photons leave the cavity is κ, and depend on the reflection coefficients of the two mirrors. By considering only one of the mirrors as the preferred channel of collection κ_{opt}, and accounting all undesired optical losses with κ_{loss}, then a maximum quantum efficiency (producing and collecting photons) will be given at $\kappa_{\text{opt}} = \sqrt{(1 + \kappa_{\text{loss}}/\gamma)(4g^2 + \kappa_{\text{loss}}\gamma)}$. Minimizing all unwanted loss channels while maximizing the quantum efficiency requires a careful materials selection and technological implementation.

The step-by-step description on how to construct and characterize a system with optimized losses, for achieving a near-ideal single photon source, is elucidated here.

2.3 A microcavity for maximal quantum efficiency

2.3.1 $\mathcal{Q}$-factor design of a one-sided cavity

In order to construct a microcavity to be employed in an efficient single photon source, one has to carefully design its loss channels. Ideally, the cavity will only have one loss channel: the one port via which single photons are collected. This means that this "one-sided cavity" must be composed of one highly reflective "bottom" mirror with very small losses, and a "top" mirror with optimized losses.

The total loss rate in a resonant cavity κ can be quantified by determining the cavity's $\mathcal{Q}$-factor, which can be limited by undesired absorption in gated regions of the semiconductor heterostructure, surface-related absorption at the semiconductor-air interface, and scattering. This means that the total loss rate of the cavity κ has contributions from the preferred loss channel κ_{top} and the undesired channel κ_{loss} which accounts for all other losses: $\kappa = \kappa_{\text{top}} + \kappa_{\text{loss}}$.

The bottom mirror, a semiconductor distributed Bragg reflector (DBR), has a nominal design GaAs-(HL)^{46}-active layer with H (L) a quarter-wave layer (QWL) in GaAs (AlAs) at wavelength 940 nm. In practice, the layers become gradually thinner during growth, and the effective center of the stopband lies around $\lambda_{\text{C}} \sim 917\,\text{nm}$. The stopband's center wavelength and its oscillations in reflectivity can be very well described by postulating a linear change in thickness during growth.[54] The transmission loss is just 1 ppm; the absorption/scattering losses amount to 373 ppm.[54]

In order to assess the losses in the entire semiconductor heterostructure (including the free-carrier absorption in active layer) we probe the $\mathcal{Q}$-factor with an extremely reflective, extremely low-loss top mirror (transmitivity 116 ppm), as shown in Fig. 2.1. We measure, at $\lambda = 920\,\text{nm}$, $\mathcal{Q} = 450,000 \pm 45,000$, corresponding to $\kappa/(2\pi) = (0.72 \pm 0.07)\,\text{GHz}$. We argue that this measured quantity sets an upper bound for κ_{loss} in the constructed single photon source, i.e. $\kappa_{\text{loss}}/(2\pi) \leq 0.72\,\text{GHz}$, as all losses – except κ_{top} – are maintained constant. Now κ_{top} can be devised to achieve a maximum quantum efficiency.

The conceived microcavity $\mathcal{Q}$-factor was calculated using a one-dimensional transfer matrix simulation (The Essential Macleod, Thin Film Center Inc.). The top mirror, a dielectric DBR, is described using the design parameters

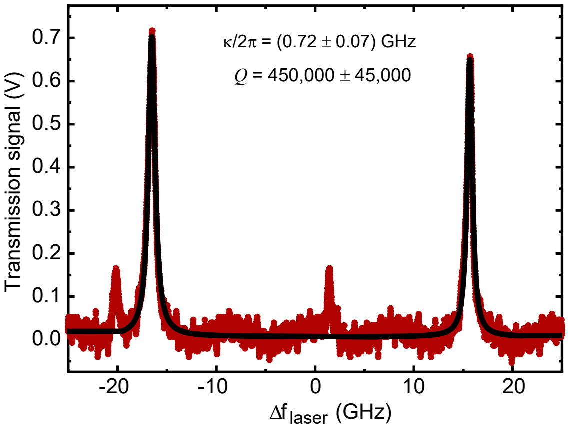

Figure 2.1: Upper bound of κ_{loss}. A microcavity composed of the semiconductor heterostructure and a high reflectivity top mirror (116 ppm transmission) yields a $\mathcal{Q}$-factor $4.5 \cdot 10^5$ near the center of the stopband, at $\lambda = 920\,\text{nm}$, corresponding to $\kappa/(2\pi) = 0.72 \pm 0.07\,\text{GHz}$. This value sets the upper bound of $\kappa_{\text{loss}}/(2\pi) \leq 0.72\,\text{GHz}$ in the experiment with a lower reflectivity top mirror with optimal design, making $\kappa_{\text{loss}}/\kappa_{\text{total}} \leq 3\%$, where $\kappa_{\text{total}} = \kappa_{\text{top}} + \kappa_{\text{loss}}$.

taking the manufacturer's values for the refractive index (mirror design: silica-(HL)^{7}H with H (L) a QWL in the high- (low-) index material at wavelength 920 nm, refractive indices 2.09 (1.48)). The transmission loss per round trip of the top mirror is 10,300 ppm. The simulated $\mathcal{Q}$-factor for the semiconductor DBR – GaAs active layer (6 QWLs) – air-gap (4 QWLs) – top mirror structure is about 15,200 at the center of the stopband, a value obtained for a cavity composed of two flat mirrors.

Another possible source of losses in a microcavity is diffraction losses at the DBR mirrors, also termed "side-losses" in the micropillar community.[55,56] The reflectivity of a DBR mirror depends significantly on the angle of incidence, and for a $\lambda/4$ stack, the reflectivity is maximized at the normal incidence. The field inside a planar cavity has a small angular spread in k-space, the reciprocal domain. This spread is centered around the normal angle and hence all the components of the field experience nearly the same reflectivity. For tightly confined modes, as is the case in a confocal microcavity, the angular spread in k-space expands, increasing the losses in the DBR mirrors and reducing the $\mathcal{Q}$-factor. We carried out finite-element numerical simulations (Wave-Optics Module, COMSOL Multiphysics) to probe the effect of the radius of the curvature R on the $\mathcal{Q}$-factor. Fig. 2.2a shows the $\mathcal{Q}$-factor as a function of the wavelength and R. Fig. 2.2b shows a cut-through of the data close to the center of the stopband at 920 nm. As expected, for small radii the $\mathcal{Q}$-factor is a strong function of R and drops to 4,600 at $R = 2.3\,\mu\text{m}$. At large radii

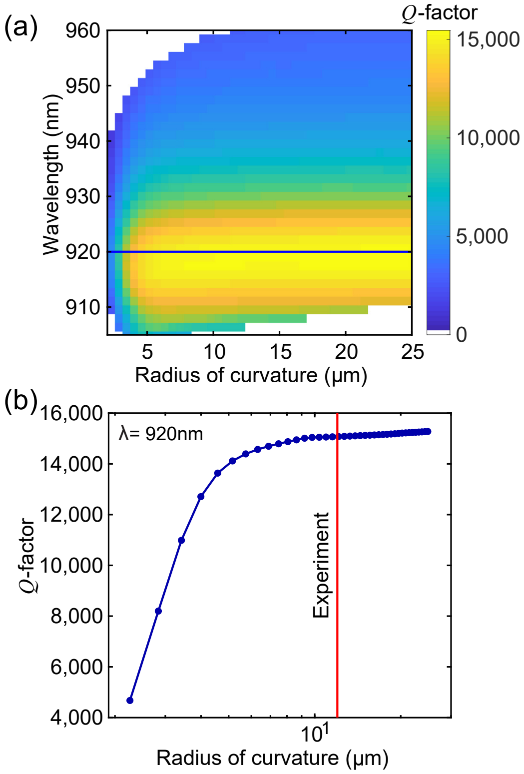

Figure 2.2: Effect of diffraction losses on the Q-factor. (a) Calculated Q-factor as a function of the wavelength and the radius of the curvature of the top mirror, for a microcavity composed of the bottom semiconductor DBR and a top 8-pair dielectric DBR. The Q-factor is maximum at the center of the stopband (close to 920 nm). (b) A cut-through of the data at the wavelength of 920 nm corresponding to the blue line in part (a). The Q-factor drops significantly for radii smaller than $6\,\mu$m signaling diffraction losses. For larger radii the Q-factor approaches 15,200.

($R > 6\,\mu$m), the Q-factor is a weak function of R, and saturates at a value of 15,200. We use a top mirror with $R = 11.98\,\mu$m in our experiments (see Fig. 2.4). We calculate a Q-factor of 15,000 for this R at the center of the stopband, very close to the value at large radii. Hence, we conclude that side losses are negligible in our experiment.

When further taking into consideration contributions from $\kappa_{\text{loss}}/(2\pi) = 0.72\,$GHz, bounded from below by the measurement performed in Fig. 2.1, the Q-factor calculated at the stopband center ($\lambda_{\text{C}} \approx 917\,$nm) with the designed top mirror reduces to approximately 14,500.

2.3.2 Semiconductor heterostructure

The heterostructure is grown by molecular beam epitaxy (MBE) and consists of an n-i-p diode with embedded self-assembled InAs quantum dots (QDs). This design allows for QD frequency tuning via the dc Stark effect as well as QD charging via Coulomb blockade. The n-i-p diode is grown on top of a semiconductor DBR, a planar bottom mirror, composed of 46 pairs of AlAs (80.6 nm thick)/GaAs (67.9 nm thick) quarter-wave layers with a center wavelength of nominally 940 nm (measured: 917 nm). Below the DBR, an AlAs/GaAs short-period superlattice (SPS) composed of 18 periods of 2.0 nm AlAs and 2.0 nm GaAs is grown for stress-relief and surface-smoothing.

From bottom to top (see Fig. 2.3a), the diode consists of an n-contact, 41.0 nm Si-doped GaAs, n^+, doping concentration $2 \cdot 10^{18}\,\text{cm}^{-3}$. A 25.0 nm layer of undoped GaAs acts as a tunnel barrier between the n-contact and the QDs. The self-assembled InAs QDs are grown by the Stranski-Krastanov process and the QD emission is blue-shifted via a flushing-step.[57] The QDs are capped by an 8.0 nm layer of GaAs. A blocking barrier, 190.4 nm of $Al_{.33}Ga_{.67}As$, reduces current flowing across the diode in forward-bias. The p-contact consists of 5.0 nm of C-doped GaAs, p^+ (doping concentration $2 \cdot 10^{18}\,\text{cm}^{-3}$) followed by 20.0 nm of p^{++}-GaAs (doping concentration $1 \cdot 10^{19}\,\text{cm}^{-3}$). Finally, there is a 54.6 nm-thick GaAs capping layer.

The layer thicknesses are chosen to position the QDs at an antinode of the vacuum electric field. The p-contact is centered around a node of the vacuum electric field to minimize free-carrier absorption in the p-doped GaAs. Coulomb blockade is established on times comparable to the radiative decay time for GaAs tunnel barriers typically $\lesssim 40$ nm thick. This is less than the thickness of a QWL thereby preventing the n-contact being positioned likewise at a node of the vacuum electric field. However, at a photon energy 200 meV below the bandgap,[58] the free-carrier absorption of n^+-GaAs ($\alpha \approx 10\,\text{cm}^{-1}$) is almost an order-of-magnitude smaller than that of p^{++}-GaAs ($\alpha \approx 70\,\text{cm}^{-1}$). The weak free-carrier absorption of n^+-GaAs is exploited in the design presented here by using a standard 25 nm thick tunnel barrier. The n-contact is positioned close to a vacuum field node, although not centered around the node itself.

After growth, individual $3.0 \times 2.5\,\text{mm}^2$ pieces are cleaved from the wafer. The QD density increases from zero to $\sim 10^{10}$ cm^{-2} in a roughly centimeter-wide stripe across the wafer. The sample used in the experiments presented here was taken from this stripe. Its QD density, measured by photoluminescence imaging, is approximately 7×10^6 cm^{-2}.

Separate ohmic contacts are made to the p^{++} and n^{+} layers. For the n-contact, the capping layer, the p-doped layers and part of the blocking barrier are removed by a local etch in citric acid. On the new surface, NiAuGe is deposited by electron-beam physical vapor deposition (EBPVD). Low-resistance contacts form on thermal annealing. To contact the p-doped layer, the capping layer is removed by another local etch. On the new surface, a Ti/Au contact pad (100 nm thick) is deposited by EBPVD. Although this contact is not thermally annealed, it provides a reasonably low-resistance contact to the top-gate on account of the very high p-doping (Fig. 2.3a).

After fabricating the contacts to the n- and p-layers, the contacts are covered with photoresist and a passivation layer is deposited onto the sample surface. A thin native oxide layer on the surface is removed by etching a few nm of GaAs in HCl. Following a rinse in deionized water, the sample is immersed in a bath of ammonium sulfide ($(NH_4)_2S$). Subsequently, the sample is transferred rapidly into the chamber of an atomic-layer deposition (ALD) setup. An 8 nm layer of Al_2O_3 is deposited using ALD at a temperature of 150°C. With the present heterostructure, this process is essential to reduce surface-related absorption: a low-loss microcavity is only achieved following surface-passivation.[59] An

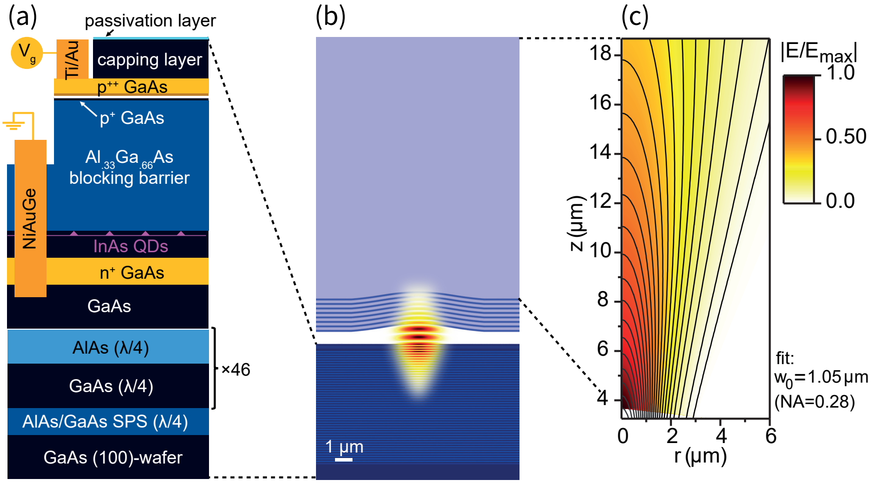

Figure 2.3: Heterostructure design and numerical simulation of the microcavity. (a) The semiconductor heterostructure consists of a DBR and an n-i-p diode structure with embedded self-assembled InAs QDs. (b) Numerical simulation of the vacuum electric field $|E_{\mathrm{vac}}|$ confined by the microcavity (image to scale). (c) Color-scale plot: normalized electric field within the SiO_2 substrate supporting the "top" mirror. Contour lines: fit of a Gaussian beam to the calculated normalized electric field. The fit yields a beam waist of $w_0 = 1.05\,\mu$m corresponding to a numerical aperture of NA $= 0.279$. $|E_{\mathrm{max}}|$ is the maximum electric field amplitude in this particular domain.

advantage of the surface passivation lies in the fact that it prevents the native oxide of GaAs from re-forming after its removal: it provides a stable termination to the GaAs heterostructure.[60] Following the surface-passivation procedure and photoresist stripping, the NiAuGe and Ti/Au films are wire-bonded to large Au pads on a sample holder. Using silver paint, macroscopic wires (twisted pairs) are connected to the Au pads.

When applying a voltage across the gates of this n-type device, the neutral exciton, X^0, is observed at intermediate biases. The negatively-charged trion, X^-, is observed at more positive bias, and the positively-charged trion, X^+ at more negative voltages. This particular device presents a small leakage current at the X^- voltage, making it more appropriate to work with X^+ instead. Given a source of holes, n-type devices exhibit Coulomb blockade of positively-charged excitons.[28] The X^0 and X^+ can both be excited by the same laser pulse. The splitting $E(X^+) - E(X^0)$ varies from QD to QD in a range between 606 GHz (QD1) to 143 GHz (QD3). We speculate that at lower voltages, the QD is initially empty. On exciting an X^0 the electron tunnels out rapidly leaving a single hole, allowing the X^+ transition. Should the QD lose its residual hole for any reason, the process repeats very rapidly.

2.3.3 Curved mirror fabrication

The top mirror is fabricated in a 0.5 mm thick fused-silica substrate. An atomically-smooth crater is machined at the silica surface via CO_2-laser ablation.[61, 62] We achieve craters with a similar radius of curvature as described in Ref.,[62] but with a shallower profile by substituting the focusing lens in the ablation setup by a lens with NA = 0.67.

The profile of the fabricated crater is measured by a confocal laser scanning microscope (Keyence Corporation), as shown in Fig. 2.4a. From the two-dimensional height profile, two principal axes can be identified, and the profile parameters can be extracted (Fig. 2.4b). The radius of curvature of this crater is $R = (11.98 \pm 0.02)\,\mu$m and the sagittal height $s = (0.41 \pm 0.02)\,\mu$m. The two principal axis present an asymmetry of 4.5% in radius of curvature. After laser ablation, the crater is coated with 8 QWL-pairs of Ta_2O_5 (refractive index $n = 2.09$ at $\lambda = 920\,$nm) and SiO_2 ($n = 1.48$ at $\lambda = 920\,$nm) layers (terminating with a layer of Ta_2O_5) by ion-beam sputtering at a commercial company (Laseroptik GmbH), see Fig. 2.3b.

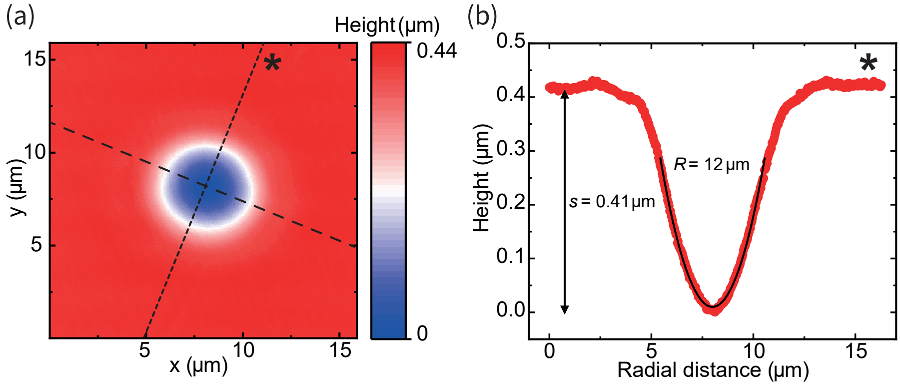

Figure 2.4: Geometrical characterization of the curved mirror. Following CO_2-laser machining, the fabricated crater's profile is measured with a confocal laser scanning microscope. (a) Height map of the crater determined with sub-nm resolution. From the height map, the two principal planes are extracted by fitting a two-dimensional Gaussian function to the data. (b) By evaluating the height information along the two principal axes, it is possible to extract the crater's parameters such as the radius of curvature $R = (11.98 \pm 0.02)\,\mu\text{m}$, sagittal height $s = (0.41 \pm 0.01)\,\mu\text{m}$, and asymmetry of 4.5%.

2.3.4 Microcavity characterization

The microcavity is a highly miniaturized Fabry-Perot type resonator. A fundamental mode is resonant for a given laser frequency at a particular microcavity length. In order to determine the $\mathcal{Q}$-factor of the microcavity, a dark-field measurement is performed, as shown in Fig. 2.5a. Given the spectral tunability of the microcavity, its $\mathcal{Q}$-factor can be determined for a wide wavelength range within the stopband of the mirrors, centered around $\lambda_C \approx 917\,\text{nm}$, as shown in Fig. 2.5b.

Fig. 2.5a shows such a measurement performed on a fundamental mode at $\lambda = 922\,\text{nm}$. The fundamental mode splits into two modes, each linearly polarized, with opposite polarizations, H and V. The mode-splitting $f_V - f_H$ is -34.6 GHz. The H and V axes align with the crystal axes of the semiconductor wafer. This points to the physical origin of the mode-splitting: a small birefringence in the semiconductor. A thorough discussion on the topic is reported in Chapter 6. The birefringence is probably induced by a very small uniaxial stress. The splitting of the fundamental microcavity mode into two separate modes together with the linear, orthogonal polarizations of these two modes are exploited in the experiment to achieve high efficiencies in our experiment, as discussed in Chapter 3. The mode-splitting is, therefore, an important

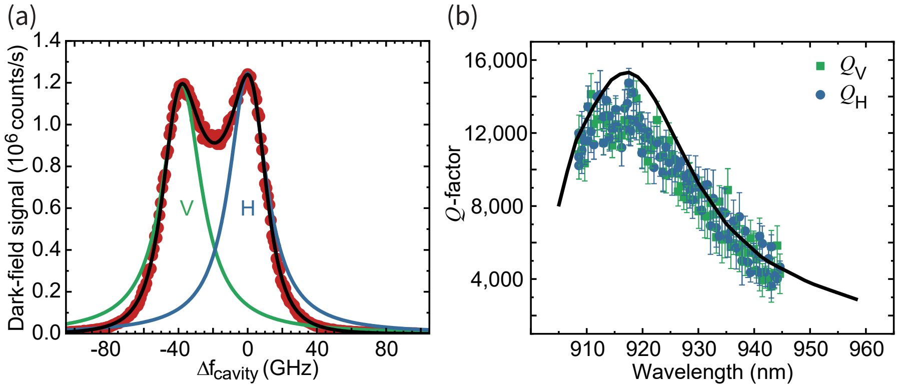

Figure 2.5: $\mathcal{Q}$-factor of the microcavity. (a) Signal versus optical frequency expressed as a detuning with respect to the upper-frequency resonance. The microscope operates in dark-field mode with principal axes lying at 45 degrees to the principal axes of the microcavity. The wavelength is $\lambda = 922\,\text{nm}$. The fundamental mode splits into two modes both with linear polarization, one H-polarized, the other V-polarized. The H- and V-axes correspond to the crystal axes of the GaAs wafer. The transmission data (red dots) are fitted to a double-Lorentzian function squared (black line) yielding in this measurement $\mathcal{Q}$-factors for the two polarized modes: $\mathcal{Q}_{\text{H}} = 11,900 \pm 1,000$ and $\mathcal{Q}_{\text{V}} = 12,800 \pm 1,000$. The mode-splitting $f_V - f_H$ is -34.6 GHz. (b) A measurement of $\mathcal{Q}_{\text{H}}$ (blue points) and $\mathcal{Q}_{\text{V}}$ (green points) can be extracted across a wide spectral range, demonstrating good agreement between calculated and experimental $\mathcal{Q}$-factors. We note that there is no systematic difference between $\mathcal{Q}_{\text{H}}$ and $\mathcal{Q}_{\text{V}}$.

parameter. Performing this measurement at different locations on the sample yields a spread in mode-splittings. For the quantum dots investigated in Chapter 5, QD1 to QD6, the splitting lies between -34.6 (QD6) and -50 GHz (QD1).

The $\mathcal{Q}$-factors of both H- and V-polarized modes are extracted from the dark-field spectrum (exemplified in the green and blue curves in Fig. 2.5a) yielding $\mathcal{Q} = 12,600 \pm 1,000$ ($\kappa/(2\pi) = 25.9\,\text{GHz}$) at $\lambda = 917\,\text{nm}$. This is very close to the value expected by design, 14, 200. The small difference between the calculated and experimental $\mathcal{Q}$-factors may well arrive from imperfect knowledge of the optical thicknesses in the two DBRs, or contributions from a small amount of roughness at the GaAs surface (refer to Chapter 4). The finesse is $\mathcal{F} = 506 \pm 50$, and determined by microcavity scanning at a fixed wavelength. Unlike the mode-splitting, the $\mathcal{Q}$-factors have no variations within the error bar from position to position in the sample.

The microcavity does not have a monolithic design and is potentially susceptible to environmental noise, vibrations and acoustic noise. The microcavity is operated in a helium bath-cryostat. The cryostat is shielded from vibrational noise by an active damping stage and from air-borne acoustic noise by an acoustic enclosure (see Sec. 2.4). Using the microcavity itself as a noise sensor shows that environmental noise is significant only when operating with a finesse above $10,000$,[62] corresponding to a $\mathcal{Q}$-factor of approximately 10^5 with the present design. Here, the $\mathcal{Q}$-factor is approximately 10^4 and the experiment is not troubled by residual environmental noise.

2.3.5 Properties of the output mode

A numerical simulation of the microcavity mode was used to determine the parameters of the output beam of the microcavity, notably the beam waist. The calculated beam in the SiO_2 substrate, i.e. in the region above the top mirror (Fig. 2.3c), is fitted to a Gaussian beam[63] of the form

$$|E(r,z)| = |E_0| \frac{w_0}{w(z)} e^{-r^2/w^2(z)} \tag{2.1}$$

with waist radius at z given by

$$w^2(z) = w_0^2 \left(1 + \left(\frac{z}{z_\mathrm{R}}\right)^2\right). \tag{2.2}$$

$z_\mathrm{R} = n\pi w_0^2/\lambda_0$ is the Rayleigh range in the medium (refractive index $n = 1.4761$ is taken for SiO_2). The fit taking w_0 (and $|E_0|$) as fit parameters results in $w_0 = 1.05\,\mu$m. This corresponds to a numerical aperture of $\mathrm{NA} = \lambda_0/(\pi w_0) = 0.279$.

2.4 Experimental setup

2.4.1 Optical setup

In the experiment, the microcavity and one lens, the objective lens, are mounted inside a helium bath-cryostat ($T = 4.2\,$K). A window enables free optical-beams to propagate from an optical setup at room temperature to the microcavity system at low temperature,[54, 62, 64, 65] as shown in Fig. 2.6. The top-mirror of the microcavity is fixed at the top of a titanium “cage”, inside which the

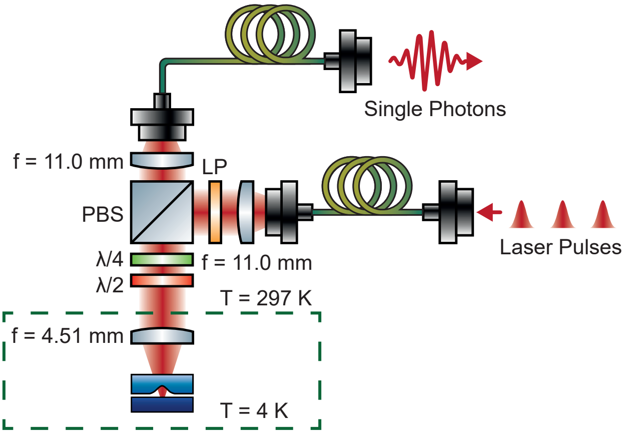

Figure 2.6: The optical setup. The microcavity system resides in a cryostat at $T = 4.2\,\mathrm{K}$. Light is coupled in and out of the microcavity with a polarization-based dark-field microscope. The objective lens is placed inside the cryostat along with the microcavity; the rest of the microscope is located outside the cryostat. Laser light enters via a single-mode optical fiber and is collimated with an $f = 11$ mm lens, passing through a linear-polarizer (LP). The input is reflected by a polarizing beam-splitter (PBS); the polarization axis of the excitation, the V-axis, is set by the half-wave plate ($\lambda/2$). The PBS and a quarter-wave plate ($\lambda/4$) suppress the coupling of unwanted back-reflected laser light into the collection arm. H-polarized single photons generated by the emitter are transmitted through the PBS and focused into the final single-mode optical fiber.

sample, mounted on a piezo-driven xyz nano-positioner, is placed.[54,62,64,65] The nano-positioner allows for full *in situ* spatial (x,y) and spectral (z) tuning of the microcavity. The titanium cage sits on another xyz nano-positioner, which allows for positioning of the microcavity relative to the objective lens, an aspheric lens of focal length $f_{\mathrm{obj}} = 4.51\,\mathrm{mm}$ (355230-B, NA = 0.55, Thorlabs Inc.), leading to close-to-perfect mode matching of the microcavity and the microscope.

The microscope has a polarization-based dark-field capability.[66] As shown in Fig. 2.6, laser light is input into the microscope via a single-mode fiber. The beam is collimated by a $f_{\mathrm{fiber}} = 11\,\mathrm{mm}$ aspheric lens (60FC-4-A11-02, Schäfter + Kirchhoff GmbH). A linear polarizer (LP) guarantees the polarization-matching of the input beam to a polarizing beam-splitter (PBS) which reflects the light towards the microcavity. A half-wave plate allows the axis of the polarization to be rotated: the output state is chosen to match one of the principal axes of the microcavity, the V-axis. The light is then coupled into the microcavity by the objective lens. The same lens collects the microcavity output. H-polarized light is transmitted by the PBS and focused by a lens (60FC-4-A11-02, Schäfter

+ Kirchhoff GmbH) into a single-mode optical fiber (780HP fiber, Thorlabs Inc). In the dark-field scheme, the suppression of V-polarized laser light is optimized by adjusting an additional quarter-wave plate in the main beam-path. Confocal detection is crucial. For pulsed excitation, an extinction ratio up to 10^6 is achieved (for continuous wave excitation, it is up to 10^8) and remains stable over many days of measurement.[66]

The estimation of the microcavity beam waist (Sec. 2.3.5) was used to optimize the fiber-coupling efficiency by selecting an appropriate aspheric lens in front of the optical fiber. The objective lens (355230-B, NA = 0.55, Thorlabs Inc.) has a focal length $f_{\mathrm{obj}} = 4.51\,\mathrm{mm}$. Its NA is considerably larger than the NA of the microcavity in order to minimize clipping losses. The lens coupling the output into the final optical fiber should be chosen to ensure mode-matching with the single-mode in the fiber. The fiber has a nominal mode-field radius of $w_1 = (2.71 \pm 0.27)\,\mu\mathrm{m}$ at $\lambda = 920\,\mathrm{nm}$ (780HP fiber, Thorlabs Inc.). The focal length for optimum fiber-coupling is $f_{\mathrm{fiber}} = f_{\mathrm{obj}} \cdot w_1/w_0 = (11.6 \pm 1.2)\,\mathrm{mm}$. Thus, an $f_{\mathrm{fiber}} = 11\,\mathrm{mm}$ aspheric lens was chosen for the experiments.

The mode-locked laser (Mira 900-D picosecond mode, Coherent GmbH) operates at a repetition rate of 76.3 MHz. The spectral width lies in the range between 60 and 100 GHz corresponding in the transform-limited case to temporal widths between 5 and 3 ps, respectively, and depends on the exact locking condition of the laser. The temporal width is the full-width-at-half-maximum of the intensity.

Source of loss	Throughput
Surface of cavity's top mirror	$(96.00 \pm 0.25)\%$
Objective lens	$(99.00 \pm 0.18)\%$
Cryostat optical window	$(99.00 \pm 0.18)\%$
Half-wave plate	$(98.91 \pm 0.78)\%$
Quarter-wave plate	$(98.69 \pm 0.78)\%$
2x PBS	$(92.00 \pm 1.10)\%$
Focusing lens	$(99.00 \pm 0.50)\%$
Fiber surfaces	$(92.00 \pm 0.18)\%$
Fiber-mode matching	$(89.66 \pm 2.79)\%$
η_{optics}	$(69.00 \pm 3.58)\%$

Table 2.1: Optical throughput of experimental setup.

In order to estimate the throughput of the optical system, i.e. η_{optics}, the following room-temperature experiment is conducted: a single-mode optical fiber (780HP fiber, Thorlabs Inc.) outputs laser light into free-space, which is collimated by an aspheric lens with effective focal length 18.40 mm (C280TMD-B, Thorlabs Inc.). We measure the power out-coupled from this fiber, P_1. We then add all the optical components (Fig. 2.6) and couple the light optimally into a second optical fiber and measure the out-coupled power from this second fiber, P_2. This gives us an estimation of losses in the microscope head: P_2/P_1. This estimation gives the absorption losses in the full set-up: clipping losses, the reflection losses – the fibers lack anti-reflection coatings – and also any wavefront distortions which limit the in-coupling to the second fiber. We find $\eta_{\text{optics}} = (69.0 \pm 3.6)\%$. The detailed measured optical throughput estimated for each element is provided in Table 2.1.

2.4.2 Calibration of detectors

Two photon-counting detectors were used to perform experiments in this work, a superconducting NbTiN-nanowire single-photon detector (SNSPD) unit (EOS 210 CS Closed-cycle, Single Quantum B.V.) optimized for operation at 950 nm; and a near-infrared optimized, fiber-coupled silicon avalanche photodiode (APD, model SPCM-NIR, Excelitas Technologies GmbH & Co. KG). In order to determine the efficiency of single-photon creation in this work, a careful calibration of the detectors' efficiencies was performed.

The measurement relies on a setup with a free-space laser beam (out-coupled from an optical fiber with angled facet), a set of calibrated neutral density filters (NDs) that can be placed in and out of the beam path, and a second optical fiber into which the beam is coupled (in-coupling via an angled facet). The frequency f of the laser light is determined precisely prior to measurement with a interferometric device (HighFinesse Laser and Electronic Systems GmbH). For an optical power P, the photon flux is $\frac{\mathrm{P}}{hf}$ where h is Planck's constant.

With the NDs removed from the beam's path, the optical power emerging out of the second fiber is measured with a calibrated silicon photodiode (Sensor Model S130C, Power measuring console PM100D, Thorlabs Inc.). The attenuating NDs are subsequently placed into the beam's path in order to avoid saturating the photon-counting detectors. The photon rate out of the fiber is then measured using both the SNSPD and the APD. The efficiency of each detector is given by the ratio of the measured count-rate to the known photon flux.

The efficiency of the SNSPD is determined to be η_{SNSPD} =(82±5)%. This value matches closely the specifications provided by the manufacturer of 83% at a wavelength of 940 nm. The efficiency of the APD is η_{APD} =(42±3)% with an angled facet directly in front of the detector (FC-APC type fiber). The efficiency is slightly higher, η_{APD} =(44±3)%, with a flat facet directly in front of the detector (FC-PC type fiber). The errors in the measurements arise from 4% in the calibration of the NDs, 1.5% in the calibration of the NDs, 3% nominal error of the silicon photodiode, and shot noise in the detectors (1.0%).

We note that for the APD, due to the dead-time of the detector (typically $\sim 20\,\mathrm{ns}$), a linearity correction factor must be applied to count rates above 200 kHz. This correction factor scales quadratically from 1 at 200 kHz to 3.32 at 25 MHz. For the experiments performed in this work, the appropriate correction factor was applied to take this effect into account. The SNSPD has a nominal dead-time $\leq 15ns$, and it nominally responds linearly to count rates below $\sim 60\,\mathrm{MHz}$. We operate way below this threshold to avoid latching of the detectors, when using multiple detectors simultaneously.

2.5 Single photon coherence and purity

A high degree of indistinguishability of the single photons is essential for quantum computing algorithms relying on linear optical processing and measurement. This property is quantified by the so called Hong-Ou-Mandel (HOM) visibility. For successive single photons produced by the same source, the HOM visibility is sensitive to the coherence of the excitonic transition of the quantum emitter. We describe the experimental setup, and outline the procedure to extract the visibility of the HOM interference.

Figure 2.7 shows the optical setup for the HOM measurements. The combination of a half-wave plate and a polarizing beam splitter (PBS) is used to realize a variable beam-splitter. Three fiber-based wave-retarders are utilized to match the polarization of the light at the inputs of the fiber beam-splitter, and hence maximize the classical visibility of the interferometer $(1 - \varepsilon)$. In order to quantify the interference between the two photons, the time delay between the "clicks" (auto-correlation measurement) on the two detectors is measured in the case when the classical visibility of the interferometer is maximized (we name this measurement $\mathrm{HOM}_{\parallel}$). A second half-wave plate can be inserted into the beam path to make the photons from the two arms distinguishable and hence yield what we name $\mathrm{HOM}_{\perp}$. The raw visibility of the HOM interference is calculated as the ratio of the area underneath the curve around zero delay A respective for the two measurements, $V_{\mathrm{raw}} = 1 - \frac{A_{\parallel}}{A_{\perp}}$.

The single photon purity, another important property to be quantified for a single photon source, is measured by using only one of the optical paths in the HOM interferometer (and blocking the other arm after the PBS). The auto-correlation value $g^{(2)}(\tau)$ at a difference in time-of-arrival $\tau = 0$ depends on the probability of having other states of light other than a pure single photon

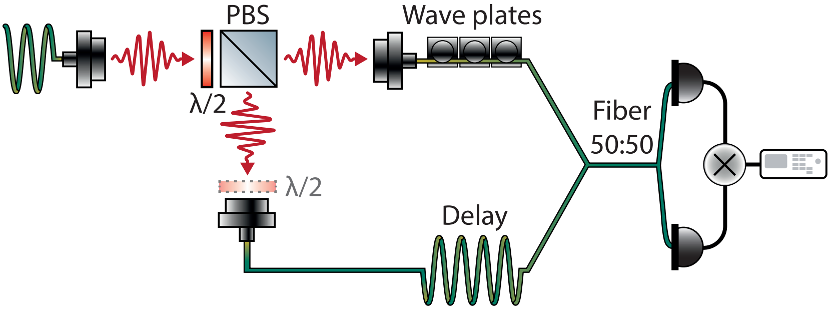

Figure 2.7: Interferometric optical setup used for Hong-Ou-Mandel visibility measurements. The setup incorporates a variable beam-splitter realized by a half-wave-plate ($\lambda/2$) and a polarizing beam-splitter (PBS), that is used to equalize the signal intensity through both optical paths. A set of wave-retarders is used to match the polarization of light to the delayed arm, maximizing the classical visibility of the interferometer. A fiber-based beam-splitter is used to perform the quantum interference experiment.

Fock state $|1\rangle$. If P_2 is the probability of creating two photons with one laser pulse, P_1 the probability of creating a single photon and P_0 the probability of creating the vacuum state, the state produced by the source can be described by $|\Psi\rangle = \sqrt{P_0}\,|0\rangle + \sqrt{P_1}\,|1\rangle + \sqrt{P_2}\,|2\rangle$. At zero-time delay,

$$g^{(2)}(0) = \frac{\langle \hat{a}^\dagger \hat{a}^\dagger \hat{a}\hat{a}\rangle}{\langle \hat{a}^\dagger \hat{a}\rangle^2}, \tag{2.3}$$

where $\hat{a}$ is the photon annihilation operator. Applying this to our state $|\Psi\rangle$,

$$\begin{aligned} g^{(2)}(0) &= \frac{2P_2}{(P_1+P_2)^2} \\ &= \frac{2P_2}{P_1^2} \qquad \text{for } P_2 \ll P_1. \end{aligned} \tag{2.4}$$

For an ideal single photon source, the probability of creating two photons is $P_2 = 0$, resulting in $g^{(2)}(0) = 0$. In reality, the finite excitation pulse length allows for a small probability of re-exciting the two-level system and having a re-emission process.

Imperfections in the HOM setup as well as the finite value of single photon purity $g^{(2)}(0)$ influence the measured V_{raw}. These imperfections can be accounted for in order to determine the “true” overlap V of two single photon states produced by the source, i.e. V can be calculated from V_{raw}.

The HOM interference between subsequent photons is measured by launching

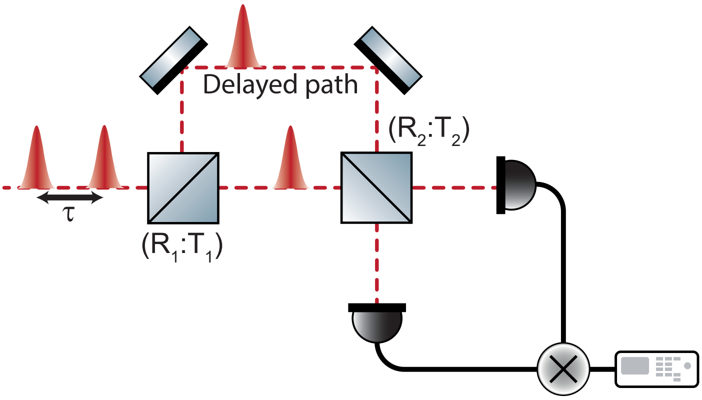

Figure 2.8: Mach-Zehnder interferometer. Two pulses of light separated by a time τ enter the interferometer via the first beam-splitter, with reflectivity:transmissivity (R_1:T_1). The early pulse of light takes the optically delayed path (with delay = τ), the later pulse takes the shorter path. The two pulses interfere at the second beam-splitter, with reflectivity:transmissivity (R_2:T_2).

the stream of single photons into a Mach-Zehnder interferometer with a variable arm. The variable arm introduces an added delay τ between the two paths, which coincides with the time interval between the two input light pulses. The optical elements in the interferometer, schematically depicted in Fig. 2.8, might not be balanced, i.e. the reflection r_j and transmission t_j coefficients of the two beam-splitters $j = 1, 2$ in the setup might not be 50%. This imbalance must be taken into account in order to estimate the "true" HOM visibility. Note that $R_j = r_j^2$, $T_j = t_j^2$, and if there are no absorption losses, then $|r_j|^2 + |t_j|^2 = R_j + T_j = 1$.

As illustrated in Fig. 2.9, the 2-photon interference can be described by transforming two input states at ports A and B of the second beam-splitter in the Mach-Zehnder interferometer to an output state at ports C and D via a transformation matrix

$$\begin{pmatrix} \hat{a}_C \\ \hat{a}_D \end{pmatrix} = \begin{pmatrix} t_2 & i\,r_2 \\ i\,r_2 & t_2 \end{pmatrix} \begin{pmatrix} \hat{a}_A \\ \hat{a}_B \end{pmatrix} \tag{2.5}$$

where $\hat{a}_i$ (with $i = A, B, C, D$) are the photon annihilation operators for the four ports of the beam-splitter and i is the imaginary unit. Solving Equation 2.5 yields

$$\begin{cases} \hat{a}_A = t_2\,\hat{a}_C - i\,r_2\,\hat{a}_D \\ \hat{a}_B = t_2\,\hat{a}_D - i\,r_2\,\hat{a}_C \end{cases}$$

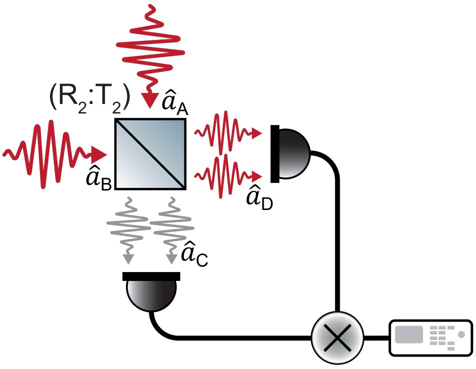

Figure 2.9: Schematic of Hong-Ou-Mandel 2-photon interference. Two optical modes are launched onto the two ports A and B of a beam-splitter. If the input states are composed of indistinguishable single photons and the beam-splitter has a perfect 50:50 (R_2:T_2) ratio, quantum interference occurs and the two input photons will either exit port C or D simultaneously with a 50:50 probability.

equivalently,

$$\begin{cases} \hat{a}_A^\dagger = t_2\,\hat{a}_C^\dagger + i\,r_2\,\hat{a}_D^\dagger \\ \hat{a}_B^\dagger = t_2\,\hat{a}_D^\dagger + i\,r_2\,\hat{a}_C^\dagger . \end{cases} \tag{2.6}$$

Mapping out the creation of a single-photon Fock state on each of the ports A, B implies

$$\hat{a}_A^\dagger\,\hat{a}_B^\dagger\,|0\rangle_A\,|0\rangle_B = |1\rangle_A\,|1\rangle_B \rightarrow (t_2\,\hat{a}_C^\dagger + i\,r_2\,\hat{a}_D^\dagger)\,(t_2\,\hat{a}_D^\dagger + i\,r_2\,\hat{a}_C^\dagger)\,|0\rangle_C\,|0\rangle_D\,,$$

making the output state

$$|\text{out}\rangle = (T_2 - R_2)\,|1\,1\rangle_{CD} + i\,\sqrt{2}\,r_2\,t_2\,|2\,0\rangle_{C\,D} + i\,\sqrt{2}\,r_2\,t_2\,|0\,2\rangle_{C\,D}\,. \tag{2.7}$$

We are interested in the probability of measuring coincident counts at the detectors placed at ports C and D. This is calculated via the probability of having an output state $|1\,1\rangle_{CD}$, which is given by the squared of the first term of Equation 2.7, resulting in

$$A_{\parallel}^{\text{quantum}} = (T_2 - R_2)^2 = 1 - 4\,R_2\,T_2. \tag{2.8}$$

If, instead, a classical state (for example, a coherent state $|\alpha\rangle$) or fully distinguishable photons are launched into input ports A and B, the probability of measuring coincidence counts at the two detectors is simply given by

$$A^{\text{classic}} = A_{\perp} = R_2^2 + T_2^2 = 1 - 2\,R_2\,T_2. \tag{2.9}$$

The HOM interference signal differs, therefore, from the lossless classical result. Imperfections in classical interference visibility $(1-\varepsilon)$ also deteriorate the true quantum interference visibility V via $(1-\varepsilon)^2 V$. We can rewrite the quantum interference probability taking into account both these contributions:

$$A_{\parallel}^{\text{quantum}} = \underbrace{1 - 2\,R_2\,T_2}_{\substack{\text{lossless}\\ \text{classical result}}} - \underbrace{(1-\varepsilon)^2}_{\substack{\text{visibility}\\ \text{imperfections}}}\ V\,2R_2T_2. \tag{2.10}$$

Furthermore, an imperfect single photon purity $g^{(2)}(0) \neq 0$ damages the quantum interference. In the optical setup (Fig. 2.8) the first and second beamsplitters have reflectivity (transmitivity) R_1 (T_1) and R_2 (T_2) respectively. The probability of having the input of two consecutive light pulses $|\text{in}\rangle = |1\rangle\,|1\rangle$ is P_1^2. A coincidence event will occur only in the case the early photon takes the delayed optical path and the late photon takes the shorter path. Then, for N input-pairs detected,

$$A_{\parallel}^{|11\rangle} = N\,P_1^2\,R_1T_1\,(T_2 - R_2)^2 = N\,P_1^2\,R_1T_1\,(1 - 4R_2T_2). \tag{2.11}$$

In the case of an imperfect single photon source, a pair of input pulses can contain $|2\rangle$ states. Under the assumption that if one of the pulses contains a two-photon state, the paired pulse is necessarily a vacuum state, $|\text{in}\rangle = |2\rangle\,|0\rangle$ or $|\text{in}\rangle = |0\rangle\,|2\rangle$, the probability of having such input state is $2P_0P_2 \approx 2P_2 \approx g^{(2)}(0)\,P_1^2$ (from Equation 2.4). It is important to notice that a coincidence event will only occur if both photons in the $|2\rangle$ state take the same route. Assuming further that the two photons in the two-photon pulse are completely distinguishable,[67]

$$A_{\parallel}^{|20\rangle,|02\rangle} = N\,g^{(2)}(0)\,P_1^2\,(1 - 2R_1T_1)\,(2R_2T_2). \tag{2.12}$$

The measured HOM is given by the contribution of both these signals, but only the $A_{\parallel}^{|11\rangle}$ interference is damaged by imperfections,

$$\begin{aligned} A_{\parallel} = N\,P_1^2\,\big[R_1T_1\,(1 - 2R_2T_2 - (1-\varepsilon)^2\,V\,2R_2T_2) \\ + 2g^{(2)}(0)\,(1 - 2R_1T_1)\,R_2T_2\big]. \end{aligned} \tag{2.13}$$

Our HOM interferometer setup is designed such that the first variable beam-splitter is adjusted to balance out the second beam-splitter in the Mach-Zehnder via

$$\begin{aligned} R_1 &= \frac{1}{2} + \delta \qquad & R_2 &= \frac{1}{2} - \delta \\ T_1 &= \frac{1}{2} - \delta \qquad & T_2 &= \frac{1}{2} + \delta, \end{aligned} \tag{2.14}$$

with $\delta \ll 1$, such that $R_1T_1 = R_2T_2 = RT$. Finally, the quantum ($A_{\parallel}$) and classical ($A_{\perp}$) signals reduce to:

$$\begin{cases} A_{\parallel} = N\, P_1^2 \left[RT\,(1-2RT)(1+2g^{(2)}(0)) - (1-\varepsilon)^2\, V\, 2R^2T^2\right] \\ A_{\perp} = N\, P_1^2\ RT\,(1-2RT)(1+2g^{(2)}(0)) \end{cases} \tag{2.15}$$

Finally, from $V_{\text{raw}} = 1 - \frac{A_{\parallel}}{A_{\perp}}$, we obtain the corrected HOM visibility

$$V = \frac{1}{(1-\varepsilon)^2}\left(1+2g^{(2)}\left(0\right)\right)\left(\frac{R^2+T^2}{2RT}\right)V_{\text{raw}}. \tag{2.16}$$

Assuming further that R and T are close to 50%,

$$V = \frac{1}{(1-\varepsilon)^2}\left(1+2g^{(2)}\left(0\right)\right)\left(1+2\left(R-T\right)^2\right)V_{\text{raw}}. \tag{2.17}$$

We characterized the optical setup and extracted $R = 0.495 \pm 0.001$, $T = 0.505 \pm 0.001$ and $(1-\varepsilon) = 0.995 \pm 0.0025$. The correction due to the imbalance in the beam-splitter is negligible as the splitting ratio is close to 0.5:0.5 such that the main contributions to the correction arise from the limited visibility of the interferometer and the small but finite $g^{(2)}(0)$ of the source.

In principle, further corrections arise in the case $P_2 \ll P_1$ but $P_1 \geq P_0$, as can be achieved in a very efficient single photon source. An additional HOM signal arises when a two-photon and a single-photon pulse are created successively. In practice however, the HOM setup has a low throughput and hence the assumption $P_2 \ll P_1 \ll P_0$ is reasonably fulfilled in the HOM measurements.

2.6 QD-microcavity coupling

In order to estimate the QD-microcavity coupling, a finite-elements method (Wave-Optics Module, COMSOL Multiphysics) is used to compute the vacuum electric field amplitude $|E_{\text{vac}}(r,z)|$ confined by the microcavity (Fig. 2.3b).

The model assumes axial symmetry about the optical axis ($(x, y) = 0$). We use a 1 μm thick perfectly index-matched layer at all outer boundaries of the simulation to prevent internal reflections. The model takes a top mirror with radius of curvature $R = 11.98\,\mu$m and sagittal height $s = 0.41\,\mu$m, exactly the mirror used in the experiments (see Sec. 2.3.3). At the location of the QDs ($z = z_{\mathrm{QD}}$) in the exact anti-node of the microcavity mode ($r = 0$), the field is $|E_{\mathrm{vac}}(0, z_{\mathrm{QD}})| = 35,000$ V/m. A QD at these wavelengths has an optical dipole of $\mu/e = 0.71$ nm where e is the elementary charge.[29] The X^+ consists of two degenerate circularly-polarized dipole transitions (at zero magnetic field). We consider the interaction of one of these circularly-polarized dipoles with a linearly-polarized microcavity mode. The predicted QD-cavity coupling is therefore $\hbar g = \mu \cdot E_{\mathrm{vac}}(0, z_{\mathrm{QD}})/\sqrt{2}$ yielding $g/(2\pi) = 4.2$ GHz. This dipole moment implies a natural radiative decay rate of $1.72\,\mathrm{ns}^{-1}$, equivalently $\gamma/(2\pi) = 0.27$ GHz (assuming the dipole approximation in an unstructured medium). The calculated Purcell factor is therefore $F_{\mathrm{P}} = 4g^2/(\kappa\gamma) = 11.4$.

Experimentally, the Purcell factor and coupling g can be determined by measuring the radiative decay rate of the emitter in and out of resonance with the cavity, as shown in Fig. 2.10. The natural radiative decay rate γ can be determined by gradually tuning the microcavity out of resonance with the QD, extrapolating the decay rate to large detunings. This gives $\gamma/(2\pi) = 0.30$ GHz.

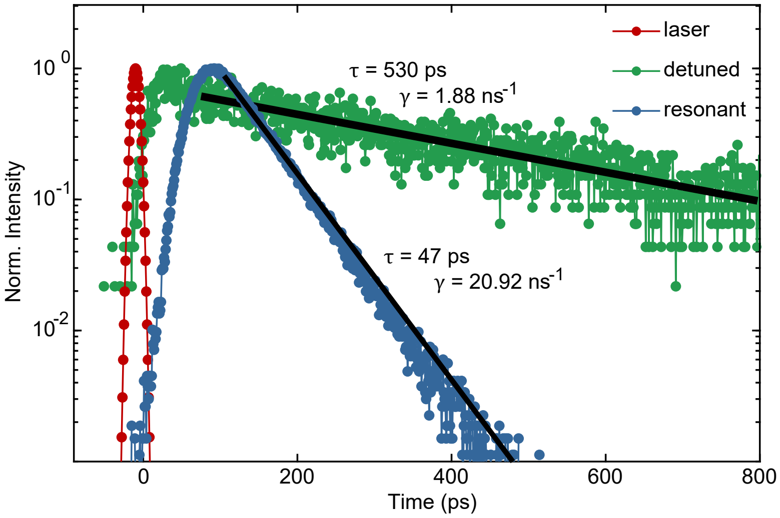

Figure 2.10: Lifetime measurement of a semiconductor quantum dot. A laser pulse (red points) with pulse width between 3 and 5 ps is used to drive the QD into its excited state. The QD decays to its ground state with a spontaneous emission rate γ. The blue and green data points show the spontaneous emission signal of a QD resonantly coupled to a microcavity and detuned from it, respectively.

This agrees well with the estimate above. On resonance, the total decay rate increases to 3.33 GHz. In the experiment however, the polarization-degeneracy of the microcavity is lifted (see Sec. 2.3.4) and the QD exciton, an X^+, interacts with both microcavity modes. We focus on the resonance with the H-polarized mode. We determine the contribution to the total decay rate from the presence of the V-polarized microcavity mode by fitting the total decay rate as a function of microcavity detuning to two Lorentzians (Chapter 5, Fig. 5.2b). We subtract the contribution from the V-polarized mode and the free-space modes at the resonance with the H-polarized mode, giving a decay rate of $\gamma_{\mathrm{H}}/(2\pi) = 2.87$ GHz. This is the decay rate contribution we would expect if the V-polarized mode were highly detuned, in other words if the microcavity mode-splitting were very large. In this limit, a circularly-polarized dipole interacting with a single linearly-polarized microcavity mode, a comparison can be made with the calculated properties of the microcavity. The Purcell factor arising from the H-polarized mode alone is therefore $F_{\mathrm{P}}^{\mathrm{H}} = \gamma_{\mathrm{H}}/\gamma = 9.6$, close to the calculated value (11.4). Using $F_{\mathrm{P}}^{\mathrm{H}} = 4g^2/(\gamma\kappa)$ and taking $\kappa/(2\pi) = 25.9$ GHz, we determine $g/(2\pi) = 4.3$ GHz, close to the calculated value. (Exact agreement is not expected as the QD dipole fluctuates from QD to QD.) We can conclude that, first, the vacuum field in the real microcavity is compatible with the value calculated from the microcavity's geometry; and second, that the lateral tuning of the microcavity enables the QD to be positioned at the anti-node of the vacuum field.

2.7 Conclusion

By carefully designing and fabricating a QD-cavity system, the creation of an ideal single photon source is within reach. Upon characterization, the natural decay rate of the QD exciton is found to be $\gamma/(2\pi) = 0.3$ GHz. The cavity mode is split in frequency into two linear polarizations, and the cavity decay rate is $\kappa/(2\pi) = 25.9$ GHz. The Purcell factor measured for the linear polarization (H) at which the photons are collected is $F_{\mathrm{P}}^{\mathrm{H}} = \gamma_{\mathrm{H}}/\gamma = 9.6$, yielding a coupling rate $g/(2\pi) = 4.3$ GHz. These parameters would imply a quantum efficiency $\eta \approx 88\%$. Finally, the throughput of the entire optical system was measured, $\eta_{\mathrm{optics}} = 69\%$, implying a final efficiency of 60%.

A final aspect of the single photon creation process is missing. The assumption taken is that the quantum emitter is certainly in the excited state at the beginning of the process, i.e. a laser pulse will, with 100% probability, perform a π-rotation on the Bloch sphere. This assumption is not necessarily true. A laser pulse with finite time width interacts with the cavity, which acts as a spectral filter. Furthermore, the experiments are performed at a finite temperature, meaning that the influence of phonons in the solid state may influence the excitation mechanism. With this process understood, a single photon creation process with high end-to-end efficiency is conceivable.

3

EXCITATION OF A TWO-LEVEL SYSTEM WITH SHORT PULSES

Adapted from:

N. Tomm*, A. Javadi*, N. O. Antoniadis, D. Najer, M. C. Löbl, A. R. Korsch, R. Schott, S. R. Valentin, A. D. Wieck, A. Ludwig and R. J. Warburton,

“A bright and fast source of coherent single photons”,

Nature Nanotechnology **16**, 399 (2021)

3.1 Summary

The efficient generation of polarized single photons can be implemented by using an unpolarized transition in a semiconductor quantum dot coupled to a microcavity with two non-degenerate orthogonal linearly polarized modes. This method enables near-ideal collection of polarized single photons avoiding losses associated with cross-polarized excitation schemes. The excitation mechanism in this scheme is non-trivial, as the laser pulses interact with the quantum emitter via a detuned cavity mode, which acts as a dispersive filter onto the pulse. We demonstrate that a detuned cavity-mediated excitation can lead to up to 97% population inversion probability for a range of optimal laser detunings

from the quantum dot's resonance, being solely limited by phonon-induced dephasing.

3.2 Introduction

The on-demand generation of single photons is a key development for applications in quantum information processing, and is an ongoing pursuit. Semiconductor quantum dots (QDs) are commonly employed as natural sources of single photons due to their high quantum efficiency and facility to be integrated into optical cavity nanostructures. Impressive results in terms of single photon creation presenting high efficiency, high purity and photon indistinguishability have been shown with a variety of platforms, such as photonic crystal cavities,[36] micropillars[39] and open microcavities.[38] The focus lies in implementing optimally designed devices to maximize the creation of single photons into a well-defined optical mode. Great effort has been spent in studying and remedying undesired optical losses and implementing a variety of schemes to obtain maximum quantum efficiency. Coherent control of the QD's transition guarantees the generation of pure and indistinguishable single photons. In the solid-state environment in which the QD resides, vibrational modes induce dephasing of the QD's state, leading to incoherent population inversion and the generation of distinguishable photons.[43, 46]

In the usual picture where a pulse of coherent light is launched upon the QD, close-to-unity population inversion probability is obtained under resonant excitation. In this case, the generated single photons are separated spatially from laser background using a cross-polarization microscope.[66] In this scheme, the excitation beam is launched in one linear polarization and the single photons are collected into the orthogonal polarization. This scheme however results in a loss of half of the single photons, at best, in the case the cavity mode is degenerate. Alternatives to strict resonant excitation can be exploited to create polarized single photons with high indistinguishability. Non-resonant excitation schemes, such as using a phonon-assisted mechanism[68, 69] or dichromatic laser pulses,[70] allow spectral filtering of the laser background from the generated single photons, and can achieve near-unity population inversion. Very high excitation efficiency has also been achieved with chirped pulses of light, in rapid adiabatic passage schemes.[71, 72]

An efficient technique to generate polarized single photons under resonant excitation is to use a charged exciton state, an inherently unpolarized transition of the QD at zero magnetic field, in a cavity that has its fundamental mode split into two linearly polarized orthogonal modes.[38, 73] The laser pulse is launched, for instance, via a V-polarized cavity mode and the spontaneous emission process is accelerated into the H-polarized cavity mode, avoiding losing 50% of the photons at the cross-polarized microscope. Since the polarized cavity mode used for excitation is detuned from the QD, this excitation mechanism may divert from the "usual" picture of a Gaussian-shaped pulse of light resonantly interacting with a two-level system.

3.3 Cavity-mediated population inversion

We exploit this technique using a positively charged trion X^+ of a semiconductor QD and a tunable open microcavity, composed of a semiconductor distributed Bragg reflector (DBR) as the "bottom" mirror and a curved dielectric DBR as the "top" mirror. The bottom mirror is a 46-pair AlAs($\lambda/4$)/GaAs($\lambda/4$) DBR grown on a [001] GaAs substrate. The top mirror comprises a microcrater with a radius of curvature 12 μm ablated into a silica substrate. The crater is coated with 8-pair $SiO_2(\lambda/4)/Ta_2O_5(\lambda/4)$, Ta_2O_5-terminated, dielectric DBR where the layers. InAs QDs are grown within an n-i-p diode heterostructure, allowing the QD charge to be controlled via the Coulomb's blockade.[38, 54] The open-nature of the microcavity allows to bring the cavity in resonance with any QD in the sample within the stopband of the mirrors. The fundamental cavity mode is split into two linear H- and V-polarized modes, detuned by approximately 50 GHz. The mode-splitting is a consequence of a small birefringence between the two crystalline directions orthogonal to the growth direction in the semiconductor sample. The cavity loss-rate κ is designed such that the main decay channel is via the top mirror, $\kappa = \kappa_{\text{top}} + \kappa_{\text{loss}}$, where κ_{loss} comprises all other loss channels except the desired channel κ_{top}. Experimentally, we determine $\kappa/(2\pi) = 25\,\text{GHz}$ with $\kappa_{\text{loss}}/(2\pi) = 0.72\,\text{GHz}$. As schematically depicted in Fig. 3.1a, we launch short pulses of light into the cavity, with its polarization aligned to one of the polarized cavity modes. The QD is resonantly coupled to the cavity mode orthogonally polarized to the laser and the generated single photons are emitted preferentially into this mode. All experiments are performed at a temperature T=4 K.

In the general case, a resonant short pulse of light will drive a two-level system (TLS) – for instance a QD's transition – around the Bloch-sphere, inverting its population from the ground state $|g\rangle$ to the excited state $|e\rangle$, as depicted in Fig. 3.1b, where the black dots indicate the path traveled around the sphere. By increasing the pulse area, a coherent drive of the population is achieved, as shown in Fig. 3.1c, solid gray line. For pulse areas corresponding to odd multiples of π, the population of an ideal TLS is driven deterministically into the excited state, and for even multiples of π the population ends in the ground state with unitary probability. One can adiabatically drive the population of the TLS into the excited state by using chirped laser pulses.[71, 72] In this case, the TLS interacts with different light frequency components present in the pulse at different instants in time, resulting in an "indirect" rotation of the transition around the Bloch sphere, as shown in Fig. 3.1b by the blue dots.

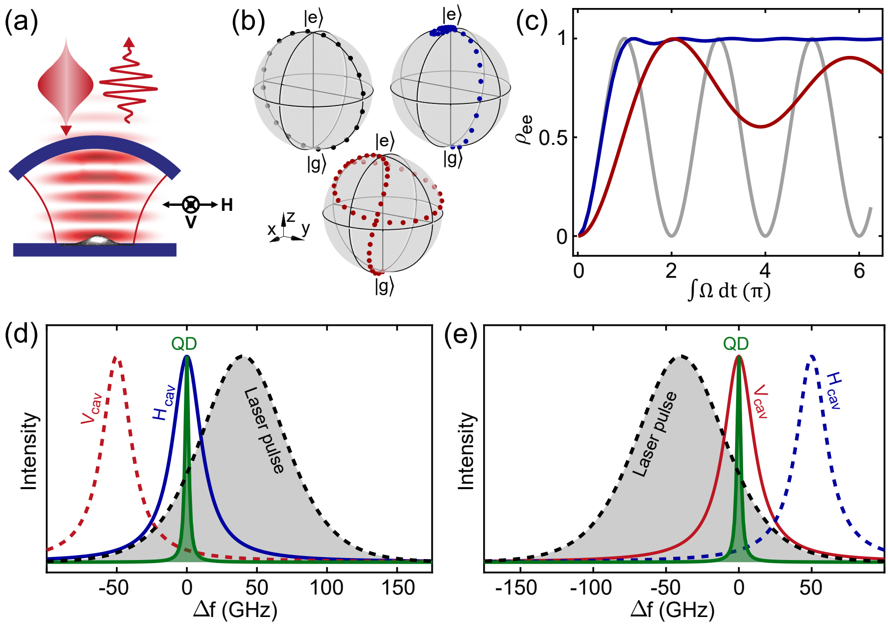

Figure 3.1: Cavity-mediated excitation mechanism with short pulses of light. (a) Schematic picture of a semiconductor QD coupled to a one-sided tunable microcavity. The cavity's fundamental mode is split into two non-degenerate H- and V-polarized modes. Short pulses of light are launched into the cavity and excite the quantum dot, which emits single polarized photons that exit the cavity through the top mirror. (b) Bloch-sphere representation of the QD's state when interacting with a resonant Gaussian pulse of light (black dots), a chirped pulse of light (blue dots) and a cavity-filtered pulse of light (red dots). (c) Density operator element of the excited state ρ_{ee} as a function of pulse area for excitation with a resonant pulse (gray line), a chirped pulse (blue line) and a cavity-filtered pulse (red line). (d) A Gaussian-shaped pulse of light with a temporal width t_p is linearly polarized and interacts with the QD mediated via a detuned cavity mode with the same linear polarization as the laser. In the case the QD is resonantly coupled to the high-frequency H-polarized cavity mode, the laser pulse center frequency is optimally blue-detuned. (e) If the QD is resonantly coupled to the low-frequency V-polarized cavity mode, the laser pulse center frequency is optimally red-detuned.

The population inversion probability, however, tends to gravitate around the excited-state pole, making it nearly insensitive to pulse area variations, as can be seen in Fig. 3.1c, blue solid line.

In the case of a detuned cavity-mediated excitation, a Gaussian-shaped pulse is convoluted with the time-response of the cavity itself. Effectively, the cavity acts as a dispersive filter, altering the spectral profile of the pulse, such that in the frequency domain it can no longer be described by a Gaussian profile. The time-evolution of the TLS's state excited by such pulse is shown in Fig. 3.1b,c in red. A full population inversion into the excited state can be obtained, but an incomplete depletion of the population happens. Naturally, the degree of spectral distortion, or modulation of the laser frequency components, depends on the original pulse's spectrum (center frequency f_L and temporal width t_p), its detuning to the excitation cavity mode $f_L - f_{\text{cav}}$, and how strongly the cavity filters it, i.e. its linewidth κ. Let's take the case in which the TLS is resonantly coupled to the higher-frequency H-polarized cavity mode, as depicted in Fig. 3.1d, and the laser pulsed is launched via the lower-frequency V-polarized cavity mode. In order to effectively excite the QD, the filtered laser pulse must retain the resonant frequency component at a considerable amplitude. This is achieved by having the original input pulse's center frequency blue-detuned from the V-polarized excitation cavity mode. In the opposite scenario, when the QD is resonant with the lower-frequency V-polarized cavity mode, and the laser is launched via the H-polarized cavity mode, the input pulse's center frequency should be red-detuned, as shown in Fig. 3.1e. These two scenarios are spectrally equivalent from the TLS's perspective.

3.4 Exciting a QD with detuned filtered pulses

We measure the polarized photon emission probability from a QD coupled to the microcavity. In Fig. 3.2a we show the scaled signal when the QD is at resonance with the high-frequency H-polarized cavity as a function of cavity detuning Δf_{cav} and the square-root of the input laser power $\sqrt{\text{Power}}$. The photon-counts in the data set are scaled taking into account the losses in the optical setup ($\eta_{\text{optics}} = 69\%$), the detector's efficiency ($\eta_{\text{APD}} = 42\%$), and the attenuation factor – we purposely attenuate the counts to avoid non-linearities in the photodetectors. The laser pulses, with temporal width t_p (full-width at half maximum of the intensity) typically between 3 and 5 ps, are filtered by the red-detuned V-polarized cavity mode. A set of different detunings Δf_L between the original laser pulse's central frequency f_L and the QD $f_0 = \omega_0/(2\pi)$ are used. When the laser is blue-detuned, $\Delta f_L > 0$, one observes the fingerprint of

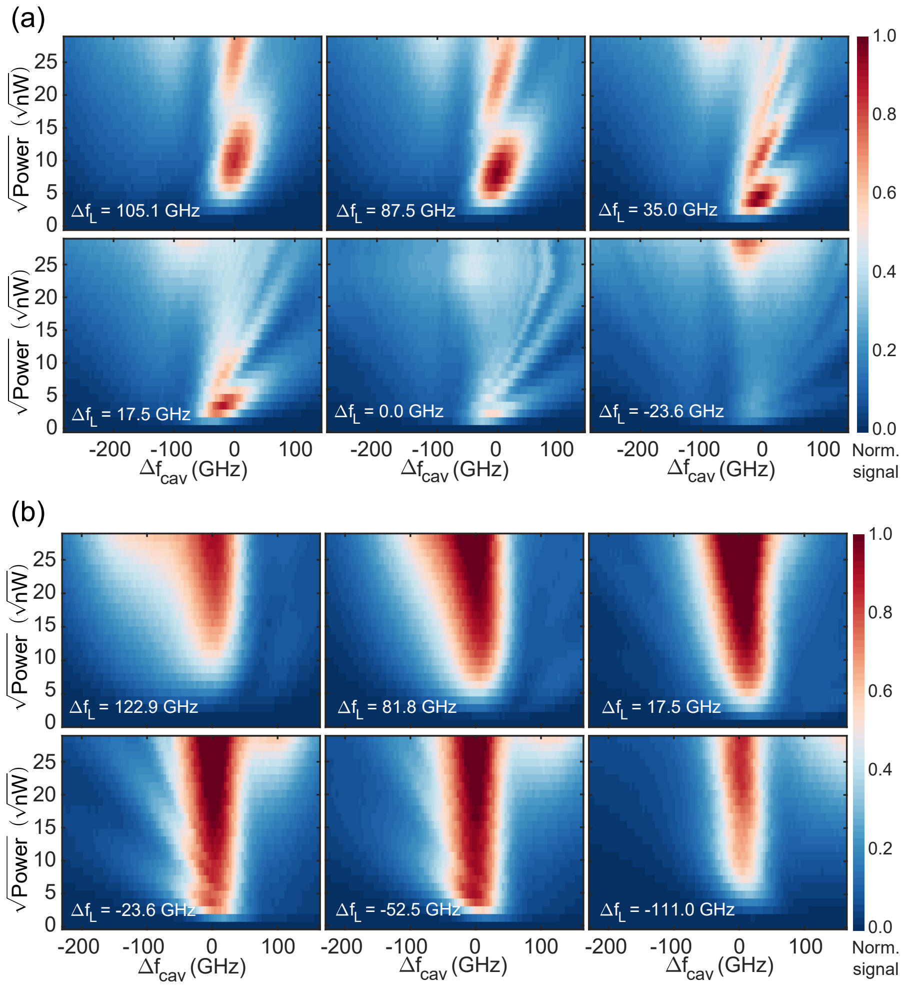

Figure 3.2: Photon emission signal from a QD excited via a detuned-cavity filtered pulse. The data is scaled accordingly to the known losses in the experimental setup. The experiment is conducted for a variety of laser detunings $\Delta f_L = f_L - f_0$, indicated in the plots. The data shows the emission probability as a function of the square-root of the input laser power and cavity detuning Δf_{cav} from the QD's resonant frequency in the case the QD is resonantly coupled to the (a) high-frequency H-polarized cavity mode or (b) low-frequency V-polarized cavity mode.

Rabi rotations for increasing powers. At resonance and for negative detunings, $\Delta f_L \leq 0$, the photon emission probability decreases drastically. We repeat the experiment in the opposite scenario, when the QD emits into the low-frequency V-polarized cavity mode and the laser is filtered by the blue-detuned H-polarized cavity mode (Fig. 3.2b). In this case, the oscillatory behaviour is less pronounced and only present in the case the laser is red-detuned $\Delta f_L > 0$.

The population drive resembles that of an adiabatic passage. The symmetry breaking in the system's evolution points to the presence of another mechanism at play.

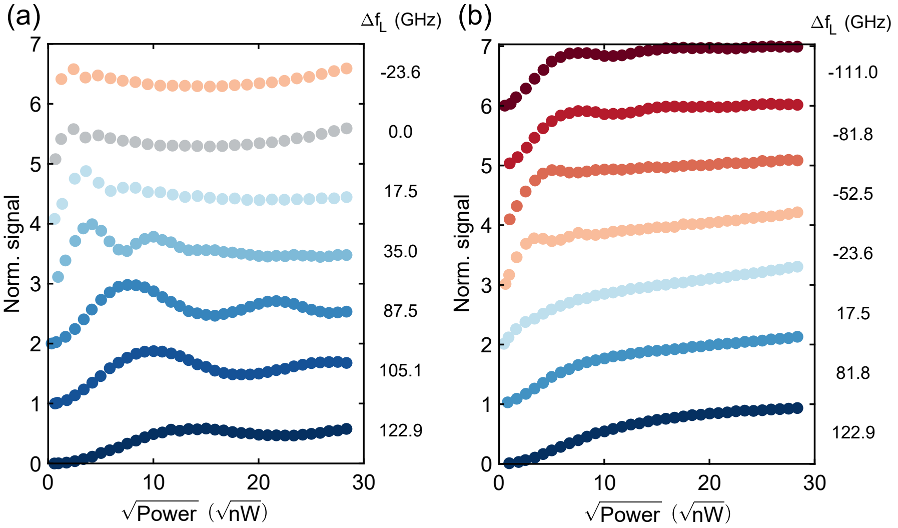

Figure 3.3: QD signal versus square root of laser power for zero microcavity-X^+ detuning, for different laser detunings. The data corresponding to each laser detuning is scaled to the known losses in the system and it is offset by one unity from each other for better visualization. The signal indicates the photon emission probability when the QD is resonantly coupled to the (a) high-frequency and (b) low-frequency cavity modes.

This emission behavior can be understood by considering phonons in the solid-state environment of the QD, and its influence on the population inversion evolution. In Fig. 3.3 it's presented the scaled photon counts evolution as a function of $\sqrt{\text{Power}}$ when the QD transition and collection cavity are at resonance $\Delta f_{\text{cav}} = 0$. We perform the experiment for different laser detunings Δf_L. In the case the QD resonantly emits via the higher-frequency cavity (Fig. 3.3a) a near unitary excitation probability can be achieved within a range of optimal blue-detuning of the laser (35 GHz$\lesssim \Delta f_L \lesssim$87.5 GHz), at the implementation of a π-pulse. The oscillations are quickly damped towards intermediary values as the laser power increases, when phonon-induced dephasing plays a more significant role (Fig. 3.4a). In the case when the QD is coupled preferentially to the lower-frequency cavity (Fig. 3.3b) near-ideal population inversion at an equivalent π-power is obtained for a range of red-detuned laser frequencies (-81.8 GHz$\lesssim \Delta f_L \lesssim$-52.5 GHz). In this configuration, the oscillations are quickly damped towards a value of unity for increasing laser powers, a very different behavior than the one observed in the previous configuration. Should a phonon of appropriate frequency be absorbed during the excitation process

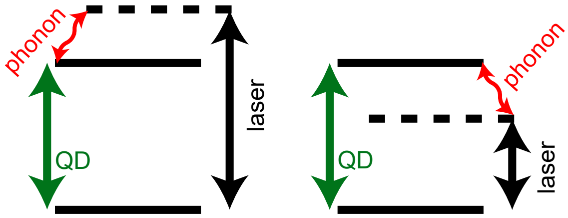

Figure 3.4: Schematic of the excitation mechanism with a laser detuned from the resonance frequency of the QD. (a) A laser pulse with spectral component of higher frequency will induce the emission of a phonon. (b) A laser pulse with spectral component of lower frequency requires the absorption of a phonon for efficient excitation.

in the latter configuration, as depicted in Fig. 3.4b, the signal would also be damped towards intermediate values. However, at the low-temperatures at which we operate, such phonons do not exist.

Notably, even though the state evolution of the transition presents an asymmetric behavior in the case the QD is coupled to a red- or blue-detuned cavity mode, we clearly show that an efficient near-deterministic population inversion can be obtained with a filtered pulse in both cases. We also experimentally demonstrate that, when exploiting the cavity-mediated excitation mechanism, the maximum excitation probability is not obtained at a strict "resonant" excitation.

3.5 Filtered pulse excitation mechanism

We describe the interaction between a TLS resonantly coupled to an H-polarized cavity and a driving electric field $\overline{E(t)} = \frac{\overline{E_0(t)}}{2}(e^{i\omega_L t} + e^{-i\omega_L t})$, where $\overline{E_0(t)}$ is a slowly varying envelope function. The laser field of frequency ω_L interacts with the TLS via a second cavity mode, V-polarized, with frequency ω_{cav}. The laser pulse itself is detuned by an angular frequency $\Delta_L = \omega_L - \omega_0$ from the H-polarized cavity mode and the TLS. The Hamiltonian describing this interaction is given by

$$\hat{H} = \hbar g \left(\hat{a}_H^\dagger \hat{\sigma}_- + \hat{a}_H \hat{\sigma}_+ \right) + \hbar \left(\overline{E(t)} \cdot \overline{\mu} \right) \left(e^{i\omega_0 t} \hat{\sigma}_+ + e^{-i\omega_0 t} \hat{\sigma}_- \right), \tag{3.1}$$

where ω_0 is the frequency related to the energy difference between the excited

$|e\rangle$ and ground states $|g\rangle$ of the TLS, $\overline{\mu}$ is the dipole moment of the TLS, $\hat{\sigma}_- = |g\rangle\langle e|$ and $\hat{\sigma}_+ = |e\rangle\langle g|$ are the lowering and raising operators of the TLS respectively. g is the coherent coupling constant between the H-polarized cavity and the TLS, $\hat{a}_H$ is the annihilation operator of the H-polarized cavity mode.

The electric field is best described in the frequency domain. Assuming the laser pulses are modulated in time by $\overline{E_0(t)}$ with a Gaussian profile with an intensity full-width at half maximum of t_p, the Fourier transform of the laser field reads

$$E(\omega) = \frac{1}{2}\left(E_0(\omega+\omega_L) + E_0(\omega-\omega_L)\right), \tag{3.2}$$

where $E_0(\omega) = e^{-t_p^2\cdot\omega^2/8\ln 2}$ is the Fourier transform of $E_0(t)$, and only has significant amplitude around zero frequency. This allows us to rewrite Eq. 3.1 as

$$\hat{H} = \hbar g\left(\hat{a}_H^\dagger\hat{\sigma}_- + \hat{a}_H\hat{\sigma}_+\right) + \hbar\,\Delta\omega_0\,\hat{a}_H^\dagger\hat{a}_H + \frac{\hbar}{2}\left(\mathcal{F}^{-1}\{\Omega(\omega-\omega_0)\}\,\hat{\sigma}_+ + h.c.\right), \tag{3.3}$$

where $\Omega(\omega)$ is the Fourier transform of $2\overline{E(t)}\cdot\overline{\mu}$.

The cavity acts as a dispersive spectral filter on the laser pulse. Let's consider the case where a time-dependent laser field goes through a filter with linewidth κ. In this case, in the frequency domain we can simply write $\Omega(\omega)$ as a product of the Fourier transform of the laser pulse $E(\omega)$ and the spectral response function of the filter $T(\omega)$. The time domain response of the cavity is

$$T(t) = e^{-\kappa t/2}\cos(\omega_{cav}t)H(t), \tag{3.4}$$

where $H(t)$ is the Heaviside function. This allows us to infer the spectral response of the cavity:

$$T(\omega) = \frac{\kappa}{\kappa + 2i\cdot(\omega-\omega_{cav})} + \frac{\kappa}{\kappa+2i\cdot(\omega+\omega_{cav})}. \tag{3.5}$$

Employing Eqs. 3.2 and 3.5, we arrive at the general form of $\Omega(\omega-\omega_0)$:

$$\begin{aligned}\Omega(\omega-\omega_0) = &\frac{\kappa\, E_0(\omega+\omega_L-\omega_0)}{\kappa+2i\cdot(\omega+\omega_{cav}-\omega_0)} + \frac{\kappa\, E_0(\omega+\omega_L-\omega_0)}{\kappa+2i\cdot(\omega-\omega_{cav}-\omega_0)}\\ &+\frac{\kappa\, E_0(\omega-\omega_L-\omega_0)}{\kappa+2i\cdot(\omega+\omega_{cav}-\omega_0)} + \frac{\kappa\, E_0(\omega-\omega_L-\omega_0)}{\kappa+2i\cdot(\omega-\omega_{cav}-\omega_0)}.\end{aligned} \tag{3.6}$$

Under the rotating wave approximation, $\omega + \omega_L$ can be neglected, such that only the first term in Eq. 3.6 contributes to the dynamics of the TLS.

The leakage through the H-polarized cavity mode can be modeled using the Lindblad operator $\hat{\mathcal{L}} = \sqrt{\kappa}\hat{a}$. Phonons play a significant role in the dynamics of a pulse-driven QD, as the instantaneous Rabi frequency can be as high as several Terahertz, where the exciton-phonon coupling is strongest. One can include the effect of phonons on the TLS dynamics by using the Bloch-Redfield master equation,[74–76] Eq. 3.7, assuming a weak coupling of the TLS-cavity system to the environment. In this case, the influence of the environment can be accounted for as a perturbative term in the master equation. In the eigenvalue basis of the TLS-cavity system, the time evolution of the density matrix elements ρ describing the TLS is

$$\frac{d}{dt}\rho_{ab}(t) = -i\omega_{ab}\rho_{ab}(t) + \sum_{cd} \mathcal{R}_{abcd}\, \rho_{cd}(t), \tag{3.7}$$

where the indices a, b, c, d label the elements of the density matrix in the $|g\rangle$ and $|e\rangle$ basis, and $\mathcal{R}_{abcd}$ is the time-independent Bloch-Redfield tensor

$$\mathcal{R}_{abcd} \propto \sum_{\alpha\beta} S_{\alpha\beta}(\omega). \tag{3.8}$$

Here, $S_{\alpha\beta}(\omega) = \int_{-\infty}^{\infty} d\tau e^{i\omega\tau} g^{(1)}(\tau)$ is the noise-power spectrum associated with each system-environment interaction term, a function of the environment's first order correlation function $g^{(1)}(\tau)$. In Eq. 3.8, the α relates to the system operators through which the environment couples to the system, and β are indices related to the environment operators. One can assume that the system-environment operators are Hermitian and that cross-correlations between different environment operators are negligible, making the Bloch-Redfield tensor simply

$$\mathcal{R}_{abcd} \propto \sum_{\alpha} S_{\alpha}(\omega). \tag{3.9}$$

We use the Python package Qutip [77,78] to set up and solve the equations of motion based on the Hamiltonian in Eq. 3.3. Finally, the photon emission probability is calculated as $\int \kappa \left\langle \hat{a}_{\mathrm{H}}^{\dagger} \hat{a}_{\mathrm{H}} \right\rangle dt$. The behavior of the population inversion for the TLS varies significantly depending on the detuning of the laser Δ_L. We note that, depending on the parameters κ, Δ_L, and the mode-splitting between H- and V-polarized cavities, a near-optimal inversion is possible even in the presence of dephasing, reaching excitation efficiencies on the order of $\sim 97\%$. In the absence of phonons, a complete inversion would be possible for the same optimal parameters.

In Fig. 3.5 the black solid line is a calculation of the photon emission probability as a function of excitation power. In this simulation the V-polarized excitation cavity is red-detuned from the TLS and the H-polarized collection cavity by 50 GHz. We use $\kappa/(2\pi) = 25$ GHz, as determined experimentally in Chapter 2, and $t_p = 5.2$ ps, a typical value for the pulsed lasers used in the experiments. In this case, the optimal center frequency of the laser is blue-detuned relative the TLS, and in this case $\Delta_L/(2\pi) = 32$ GHz. We compare that to experimental data, the red dots in Fig. 3.5. Here the repetition rate of the laser is 76.3 MHz, and we account for the optical losses in the optical setup to compare fairly experiment and model. One can see good agreement between the model and the experimentally observed phenomenon. The blue dashed line presents the modeled Rabi rotations in the absence of phonons. A calculated inversion

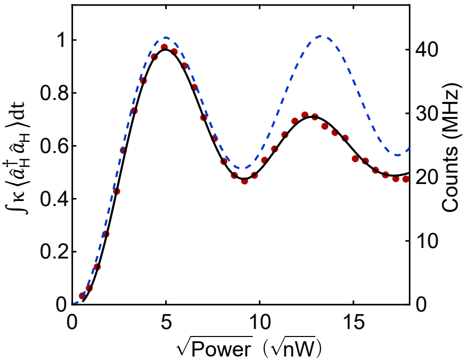

Figure 3.5: Calculated photon emission probability of a two-level system driven by filtered optical pulses. The photon emission probability $\int \kappa \left\langle \hat{a}_{\mathrm{H}}^{\dagger} \hat{a}_{\mathrm{H}} \right\rangle dt$ observed in the case the QD transition is resonantly emitted via the higher-frequency H-polarized cavity mode as a function of the excitation power. The red dots correspond to the scaled counts accounting for detector efficiency and estimated losses from the system. The solid black line corresponds to the simulation, using $\Delta_L/(2\pi) = 32$ GHz, $\kappa/(2\pi) = 25$ GHz and a detuning of -50 GHz between the V-polarized excitation cavity and the TLS. The dashed blue line is the theory calculated with the same parameters, but in the absence of dephasing.

probability $\Pi = 96.3\%$ is extracted for this data set.

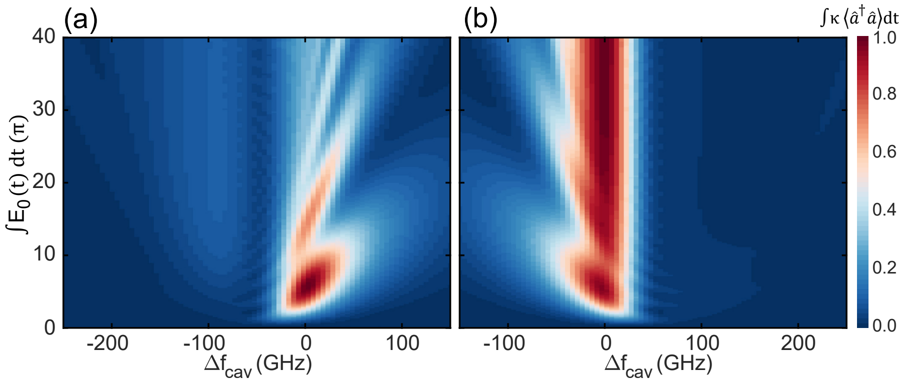

Figure 3.6: Calculated photon emission probability of a two-level system excited by a filtered short pulse of light. The photon emission probability $\int \kappa \left\langle \hat{a}^\dagger \hat{a} \right\rangle dt$ out of the collection cavity as a function of its detuning from the TLS, Δf_{cav}, and the excitation pulse area $\int E_0(t)dt$. For this simulation, $\kappa/(2\pi) = 25\,\text{GHz}$ and the two orthogonal cavity modes are detuned from each other by 50 GHz. The calculated case when the TLS is in resonance with the (a) high-frequency H-polarized cavity mode, where $\Delta_L/(2\pi) = 30\,\text{GHz}$ with pulse length $t_p = 4.4$ ps; and (b) low-frequency V-polarized cavity mode, where $\Delta_L/(2\pi) = -30\,\text{GHz}$ with pulse length $t_p = 3.6$ ps.

We show in Fig. 3.6 that we also reach a qualitative agreement between experiment and the theory for the photon emission probability as a function of cavity detuning Δf_{cav} and excitation pulse area $\int E_0(t)dt$. In Fig. 3.6a we present the calculation in the case when the QD is in resonance with the higher-frequency H-polarized cavity mode, for a blue-detuned laser ($\Delta_L/(2\pi) = 30\,\text{GHz}$) with pulse length $t_p = 4.4$ ps. At resonance, a very clear damping of the Rabi rotations can be observed as a function of increased pulse area, in very good agreement with the experimentally observed case shown in Fig. 3.2a. A very different profile is observed in the opposite case, when the QD emits photons into the lower-frequency V-polarized cavity mode, as seen in Fig. 3.6b, where the laser is red-detuned by $\Delta_L/(2\pi) = -30\,\text{GHz}$ and $t_p = 3.6$ ps. Here, at resonance, the photon emission probability tends to plateau as the excitation pulse area increases, as correspondingly observed in the experimental data presented in Fig 3.2b. Both the model and the experimental data show a clear asymmetry in the photon emission process in the case the QD is excited via a red- or blue-detuned laser light that interacts with the emitter mediated via a blue- or red-detuned cavity mode, respectively. This asymmetry is the direct consequence of a phonon-assisted excitation mechanism at low temperature.

3.6 Conclusion

The probability of population inversion of a QD upon excitation with short pulses of light is commonly assumed unitary. We show that if the QD is placed inside of an optical cavity, the cavity acts as a dispersive filter, effectively modifying the spectral contributions in the light pulses. When exciting a QD with a highly modified light pulse, the effective path on the Bloch sphere towards excited and ground states is not a direct one.

Here we elucidate the role of the cavity as a spectral filter on the excitation mechanism of a QD. We base our calculations on the experimental conditions. The fundamental cavity mode is split into two orthogonally H- and V-polarized modes detuned from each other. The circularly polarized excitonic transition in the QD is at resonance with either the higher- or lower-frequency cavity mode, and the excitation pulse is aligned in polarization with the opposite polarized cavity mode.

Contrarily to the textbook case, where the maximum population inversion is obtained under strict resonance conditions of the laser with the QD, we show that a distinct detuning between laser and QD is necessary for optimal population inversion. In the case the QD is at resonance with the blue-detuned cavity mode, the laser itself should be blue-detuned from the QD resonance for optimal rotation. In the opposite case, when the QD is resonantly coupled to the red-detuned cavity mode, the laser should itself also be red-detuned from the QD transition for maximal photon emission probability. In both cases the photon emission probability reaches values close to one, although the Rabi rotations present quite different behaviors. For optimal laser detunings, the excitation-induced dephasing causes only a slight decrease of about 3% in the excitation efficiency.

Both cases present equivalent population inversion probabilities at the best implementation of a π-pulse. The scenario in which the QD is coupled to the lower-frequency cavity mode, and laser pulses are launched via a higher-frequency cavity mode resembles the excitation mechanism in rapid adiabatic passage schemes, with a near-unitary plateau for increasing laser powers. This type of behavior could be exploited to generate polarized single photons in a more stable manner, by using a laser power above the plateau threshold, avoiding therefore susceptibility to laser power variations.

4

Surface-related optical loss in a semiconductor microcavity

Adapted from:

D. Najer*, N. Tomm*, A. Javadi, A. R. Korsch, B. Petrak, D. Riedel, V. Dolique, S. R. Valentin, R. Schott, A. D. Wieck, A. Ludwig and R. J. Warburton,

“Suppression of surface-related loss in a gated semiconductor microcavity”,

Physical Review Applied **15**, 044004 (2021)

4.1 Summary

We present a surface passivation method that reduces surface-related losses by almost two orders of magnitude in a highly miniaturized GaAs open microcavity. The microcavity consists of a curved dielectric distributed Bragg reflector (DBR) with radius $\sim 10\,\mu$m paired with a GaAs-based heterostructure. The heterostructure consists of a semiconductor DBR followed by an n-i-p diode with a layer of quantum dots in the intrinsic region. Free-carrier absorption

in the highly doped n- and p-layers is minimized by positioning them close to a node of the vacuum electromagnetic-field. The surface, however, resides at an anti-node of the vacuum field and results in significant loss. These losses are much reduced by surface passivation. The strong dependence on wavelength implies that the main effect of the surface passivation is to eliminate the surface electric field, thereby quenching below-bandgap absorption via a Franz-Keldysh-like effect. An additional benefit is that the surface passivation reduces scattering at the GaAs surface. These results are important in other nano-photonic devices which rely on a GaAs-vacuum interface to confine the electromagnetic field.

4.2 Introduction

Concepts in cavity quantum-electrodynamics (QED) can be implemented using semiconductors. A semiconductor based microcavity can be created using a micropillar,[39, 79, 80] a photonic crystal cavity,[81, 82] a whispering-gallery resonator,[60] and an open microcavity.[54, 64, 65] Quantum dots within these structures mimic atoms. In the limit of a single quantum dot (QD), a single-photon source can be realized by exploiting the weak-coupling regime of cavity-QED.[8] The strong-coupling regime of cavity-QED has been accessed with three different microcavity platforms.[54, 79, 81]

In all these semiconductor-based applications of cavity-QED, minimizing the absorption and scattering losses in the microcavity is very important. For single-photon sources operating in the weak-coupling regime, an efficient photon extraction from the microcavity is essential.[39, 80] In the strong-coupling regime, a coherent exchange between an exciton in the QD and a photon in the micro-cavity is only possible if the exciton-photon coupling exceeds the rate of photon loss. Typically, this requires the development of low-mode volume, high $\mathcal{Q}$-factor microcavities. A recurring theme in the development of such microcavities is the role of the GaAs surface. At the semiconductor surface, the symmetry of the lattice is broken. The GaAs surface is quite complex – there are a number of possible surface reconstructions, and a thin oxide layer typically forms on exposure to air.[83] Reducing surface-related absorption is crucial in the development of GaAs-based cavity-QED.

Recently, considerable success in implementing cavity-QED was reported with a QD in an open microcavity.[38, 54, 64, 65] The “bottom” mirror is a semiconductor distributed Bragg reflector (DBR), the “top” mirror a curved, dielectric DBR. The position of the bottom mirror can be tuned *in situ* with respect to the top mirror, allowing a single QD to be brought into resonance with the microcavity mode. In the latest developments, the QDs are embedded in an n-i-p diode.[38, 54] Both n- and p-doped GaAs result in free-carrier absorption.[58] To minimize the absorption within the microcavity, the n- and p-doped layers are made as thin as possible and are positioned close to the node of the vacuum electric field. This technique, positioning an absorbing layer at a vacuum field node, can also be used to reduce losses at the GaAs surface. But in this case, it involves a serious compromise. If there is a node at the surface, the largest vacuum electric field lies in the vacuum-gap and not in the GaAs material on account of interferences in the device. This reduces considerably the coupling of a QD to the vacuum electric field. An acceptably large coupling is only possible if there is a vacuum field anti-node at the surface. Success with the n-i-p devices in an open microcavity was only possible after passivating the surface.[38, 54] The role played by the passivation is elucidated here.

We probe the surface-related absorption in a GaAs open microcavity. The main diagnostic tool is a measurement of the wavelength dependence of the $\mathcal{Q}$-factor. With an untreated surface, we find that the $\mathcal{Q}$-factor is modest, approximately 10^4 at the stopband center, much lower than the value expected from the mirror designs. Following surface passivation, we find that the $\mathcal{Q}$-factor increases to $\simeq 10^6$ at the stopband center, close to the value expected from the mirror designs. This shows that, first, the dominant loss mechanism in the untreated case is related to the GaAs surface, and second, that surface passivation remedies this loss. For the untreated surface, the $\mathcal{Q}$-factor has a very strong dependence on wavelength, increasing rapidly on tuning to lower wavelengths. By comparing the $\mathcal{Q}$-factor to the result of model calculations, we find that we can account quantitatively for the $\mathcal{Q}$-factor by ascribing the loss to absorption in the capping layer, the final 55-nm-thick GaAs layer of the heterostructure. The absorption in the capping layer is an exponential function of the photon energy, pointing to Franz-Keldysh-like absorption induced by a strong electric field at the surface.[84–88] In turn, this demonstrates the main role of the surface passivation layer in this device: it reduces the surface electric field, thereby much reducing the Franz-Keldysh (F-K) absorption. The standard analytic result for the F-K effect describes the absorption at the unpassivated surface but with an electric field much higher than in the standard picture (mid-gap pinning).

4.3 The open, tunable microcavity

The microcavity[62, 64] consists of a curved dielectric DBR – the template is produced by CO_2-laser ablation[61] – paired with an "nip-DBR" semiconductor heterostructure. The InAs QDs are embedded in the intrinsic part of the n-i-p diode; the diode resides on top of a semiconductor DBR, Fig. 4.1a. We employ two dielectric top DBRs. The first (DBR-I) is composed of 22 pairs of $SiO_2(\lambda/4)$ and $Ta_2O_5(\lambda/4)$ (where λ depicts the wavelength in each material) and is terminated with SiO_2. The stopband center[i] is 973 nm. The second (DBR-II) is composed of 15 pairs of $SiO_2(\lambda/4)$ and $Ta_2O_5(\lambda/4)$, Ta_2O_5 terminated, and has its stopband center at 930 nm. The semiconductor DBR consists of 46 pairs of AlAs($\lambda/4$) and GaAs($\lambda/4$). The heterostructure is a 1.5λ-layer of GaAs including doped layers acting as top-gate (p^{++}, 10^{19} cm^{-3}) and back-gate (n^{+}, $2 \cdot 10^{18}$ cm^{-3}). The QD layer is placed at an antinode of the vacuum electric field (at a distance λ below the surface). The intrinsic region between QDs and back-gate acts as tunnel barrier for electrons and ensures that the QDs operate under Coulomb blockade at low temperature.[16] Using a piezo-based xyz nano-positioner, the microcavity features full *in situ* tunability at cryogenic temperatures.

A measurement of the $\mathcal{Q}$-factor across the stopband of the nip-DBR (Fig. 4.1b) reveals possible sources of loss in the heterostructure due to the fact that the standing wave inside the cavity shifts with wavelength (Fig. 4.1c). For instance, losses in the capping layer depend on the exact wavelength: at a wavelength-detuning of $(-30, 0, 30)$ nm with respect to the nip-DBR's stopband center, the calculated modal confinement factor (MCF – defined as the vacuum electromagnetic-energy confined in the layer-of-interest divided by the zero-point energy, $\hbar\omega/2$, i.e. the total energy of the vacuum-field mode.) of the capping layer is $(0.9\%, 6.2\%, 0.9\%)$, respectively. Therefore, if the dominant loss mechanism in the microcavity takes place within the capping layer then the change in MCF will result in a strong dependence of the $\mathcal{Q}$-factor across the stopband. Furthermore, by characterizing the mirrors carefully and by simulating the entire structure with transfer-matrix calculations, measurements of the $\mathcal{Q}$-factor not only reveal the location of the dominant loss process but can also be used to determine the loss quantitatively.

---

[i] Note that in this work, we define the stopband center as the mean value of the two wavelengths at the local minima (with $R < 90\%$) of the calculated reflectance spectrum that are closest to the maximum mirror reflectance (Fig. 4.1b).

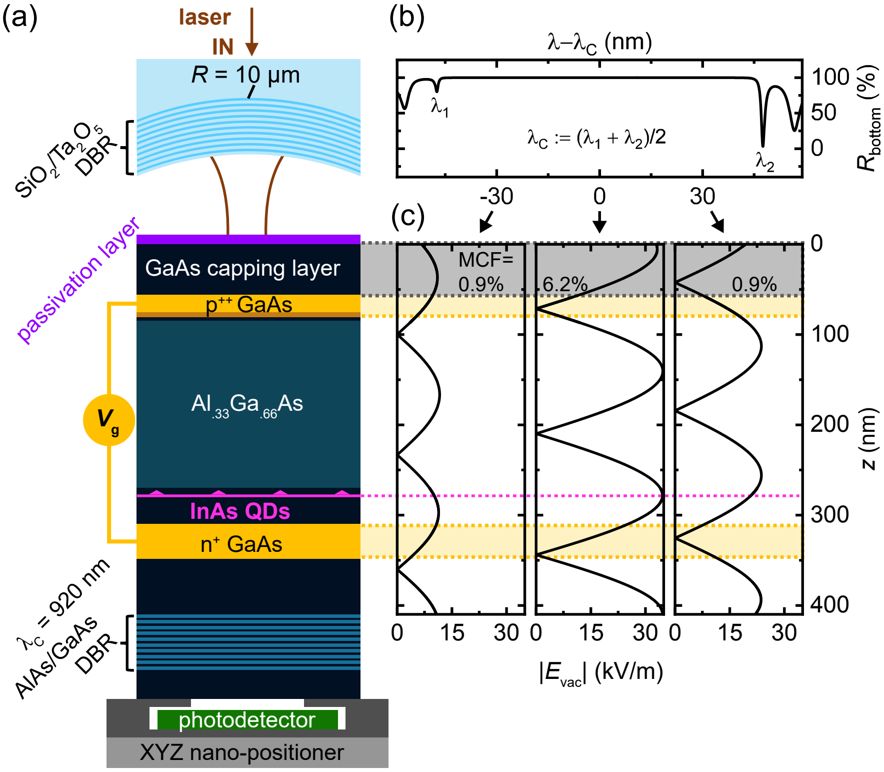

Figure 4.1: Ultrahigh $\mathcal{Q}$-factor optical microcavity as sensitive probe of surface-related absorption. (a) Schematic of the microcavity involving a curved dielectric-DBR and an n-i-p heterostructure with self-assembled InAs QDs on top of a semiconductor DBR ("nip-DBR"). (b) Simulated reflectance of the nip-DBR with stopband center $\lambda_C = 920\,\text{nm}$. (c) Calculated vacuum-field amplitude across the heterostructure for three different wavelengths $(-30, 0, +30)\,\text{nm}$ with respect to the stopband center. As the antinodes of the vacuum-field shift in position with wavelength thereby changing the modal confinement factor (MCF) in the GaAs capping layer, surface-related absorption in the capping layer (10^{-10}–$10^{-8}\,\text{cm}^{-1}$) can be probed via the microcavity by measuring its $\mathcal{Q}$-factor across the stopband. Note that at λ_C, where the coupling to the QDs is maximized, free-carrier absorption in the highly doped p- and n-gates is minimized by placing them close to a vacuum-field node. Note also that the highly reduced vacuum-field at $\lambda - \lambda_C = -30\,\text{nm}$ arises as at this wavelength, the largest vacuum electric-field is located in the vacuum gap.

4.4 GaAs surface passivation

Surface passivation of GaAs replaces the native oxide with a thin Al_2O_3 layer.[60,89] The surface passivation recipe follows in part one of the procedures described in Ref.[90] As a first cleaning step, the processed semiconductor sample (already containing Au contact pads) is successively immersed in acetone, isopropanol and ethanol inside an ultrasonic bath at $T = 40\,^\circ\mathrm{C}$. To prevent surface treatment of the contact pads, they are covered by a manually applied drop of photoresist (AZ1512HS, Microchemicals GmbH) and baked for 10 min at $T = 100\,^\circ\mathrm{C}$. At room temperature, the sample is dipped into an HCl solution (25%) for 1 min in order to remove the native oxide.[90,91] The sample is then rinsed with deionized water for $\sim 1\,\mathrm{s}$ and immediately immersed in an $(NH_4)_2S$ solution (20%) for 10 min. This procedure passivates the surface with sulfur,[92,93] preventing the native oxide from reforming. The S-layer is however not robust. For this reason, it is removed and replaced with an Al_2O_3 layer. To achieve this, on emerging from the $(NH_4)_2S$ solution, the sample is blown dry with nitrogen and immediately transferred into an atomic-layer deposition (ALD) chamber (Savannah 100, Cambridge NanoTech Inc.).

The following ALD recipe is chosen to deposit $\sim 8\,\mathrm{nm}$ of Al_2O_3 onto the sample surface: $T = 150\,^\circ\mathrm{C}$, first pulse 50 ms (water), wait 12 s, second pulse 40 ms (TMA), wait 10 s; the cycle is repeated 80 times. The Al_2O_3 layer acts as diffusion barrier for oxygen,[94] thus preventing reoxidation of the etched GaAs surface.

After surface passivation, the remaining challenge is to remove the photoresist that has been cross-linked due to the high temperature, $T = 150\,^\circ\mathrm{C}$, inside the ALD chamber. The use of *N*-methyl-2-pyrrolidone (NMP) at elevated temperatures was shown to remove successfully the cross-linked photoresist. The sample is immersed in NMP for 9–20 h (20 h yielded a better result) at $T = 40\,^\circ\mathrm{C}$ and then successively cleaned for 5 min in NMP, acetone, isopropanol and methanol inside an ultrasonic bath at $T \sim 56\,^\circ\mathrm{C}$. As a final step, a polymeric strip coating (First Contact, Photonic Cleaning Technologies) is used to remove any final residues from the sample surface.

4.5 Individual mirror characterization

Each DBR has a high reflectance for wavelengths within the stopband. Outside the stopband, there are oscillations in the reflectivity as a function of wavelength. These oscillations are sensitive to the exact layer thicknesses in the particular mirror – this dependence is exploited to characterize the layers in each DBR.

As depicted in Fig. 4.2, the cavity's top and bottom mirrors are characterized at $T = 4.2\,\mathrm{K}$ by a broadband light-source (white light-emitting-diode or halogen lamp) and a dark-field confocal microscope.[30] The light from the source is coupled into a single-mode optical fiber, the output of which is collimated and focussed onto the sample surface with an objective lens (NA=0.55). Cross-polarizing elements are used in the beam path to reject all but the light reflected from the sample surface. The detection fiber is connected to a spectrometer. The reflected light from a metallic mirror, the Au contact pad in the case of the nip-DBR, is used to record a reference spectrum. The nip-DBR's reflectance spectrum is obtained by dividing its reflected spectrum by the reference spectrum. Due to the absence of a metallic reference surface on top of the dielectric DBR-I in Fig. 4.2a, an exponential fit of the reference spectrum from Fig. 4.2b is used instead and the maximum reflectance is normalized to one.

Via 1D transfer matrix methods (Essential Macleod, Thin Film Center Inc.) the design layer thicknesses can be refined in order to fit the reflectivity oscillations outside the stopband. The obtained models for each DBR (red solid lines in Fig. 4.2) provide a convincing description of these oscillations. These mirror descriptions are then used to simulate the cavity performance, in particular the $\mathcal{Q}$-factors and transmittance values at resonance as a function of the vacuum-gap between the mirrors (Sec. 4.10). The slight discrepancy between experiment and model arises from the difficulty of recording precisely a reference spectrum for the white-light source.

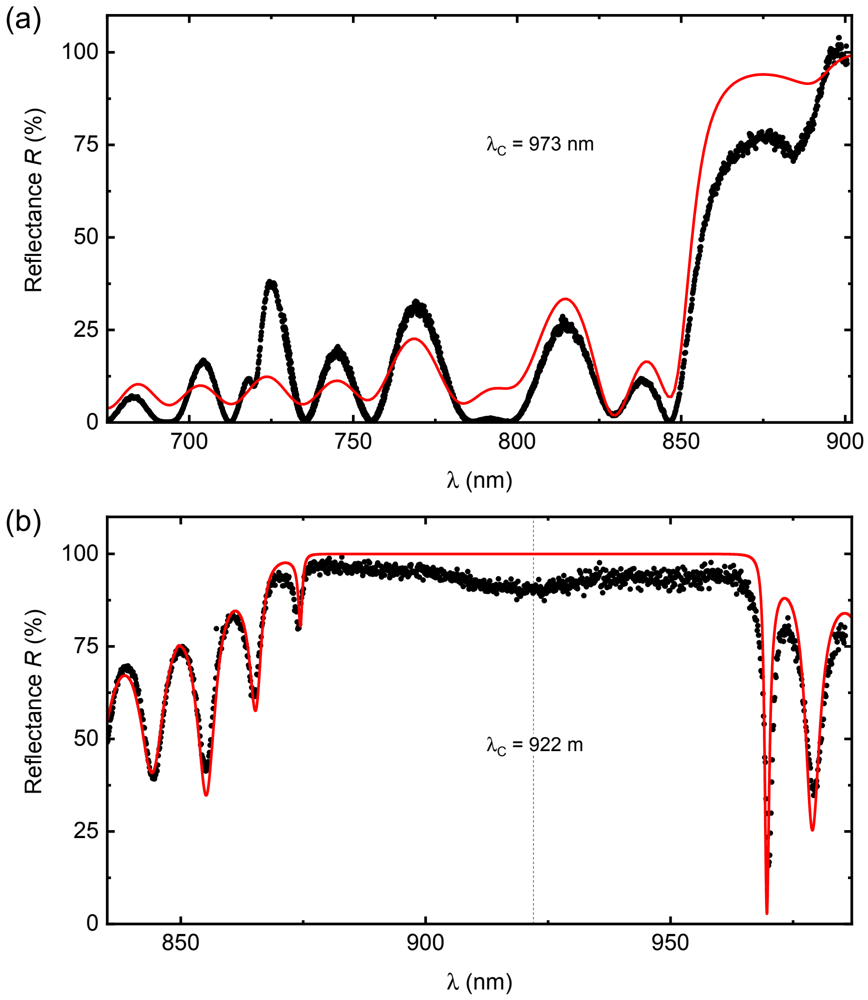

Figure 4.2: Mirror characterization via reflection measurements. Each mirror is investigated by recording the spectrum of white light reflected off the sample using a dark-field confocal microscope.[30] Via 1D transfer matrix methods (Essential Macleod), the designed layer thicknesses can be refined to fit the experimentally observed oscillations. (a) Dielectric DBR-I. The reflected signal is recorded on a flat surface away from the curved part of the mirror and normalized by the white-light spectrum. (b) Unpassivated nip-DBR. Here, the reflectance spectrum is obtained by normalizing the reflected signal from the mirror by the reflected signal from a Au contact pad (by moving the piezo-nanopositioner laterally by a few microns).

4.6 Microcavity characterization: $\mathcal{Q}$-factors

A microcavity is constructed using passivated and unpassivated semiconductor-DBRs and a curved dielectric DBR (radius of curvature $\sim$ 7–16 μm) similar to the ones characterized in Fig. 4.2. Via narrowband-laser transmission-measurements, each microcavity is characterized by determining its $\mathcal{Q}$-factor across the stopband of the semiconductor DBR. The transmission signal is measured as a function of laser frequency keeping the cavity length fixed (Fig. 4.3a). To change the cavity's resonance frequency, the mirror separation is changed by means of the Z nano-positioner.

A $\mathcal{Q}$-factor is obtained for every pair of longitudinal (TEM_{00}) modes at the minimum mirror separation ($\sim$ 2–4 μm, depending on wavelength and mirror-crater depth[62]) by fitting a double-Lorentzian. Fig. 4.3a,b show the results for an electrically-contacted passivated sample[ii] (black dots), an electrically-uncontacted unpassivated sample (blue triangles) as well as an electrically-contacted unpassivated sample (red squares), paired with DBR-I as top mirror. Without passivation, the $\mathcal{Q}$-factor is around 10^5 for the electrically-uncontacted unpassivated sample at the stopband center, and too low to measure precisely for the electrically-contacted unpassivated sample. At a red-shift of 10 nm from the stopband center, the $\mathcal{Q}$-factor for the electrically-contacted unpassivated sample is on average $3.8 \cdot 10^4$, and $1.28 \cdot 10^5$ for the electrically-uncontacted unpassivated sample (Fig. 4.3a.). These values are much smaller than the values expected from the DBRs – they signify that there is a significant loss mechanism. Around the stopband center, where the coupling to the QD layer is maximized ($\lambda_\text{C} = 915$–925 nm), the $\mathcal{Q}$-factors are strongly decreased by this loss mechanism – the loss impacts significantly the performance of a QD in the microcavity.

As the wavelength approaches the red-end of the stopband, the $\mathcal{Q}$-factors for the unpassivated samples increase. There is a pronounced asymmetry with respect to the stopband center: the $\mathcal{Q}$-factors fall monotonically as the wavelength shifts to the blue with respect to the stopband center. These results imply that the loss mechanism is a strong function of wavelength.

After passivation, the $\mathcal{Q}$-factor around the stopband center increases. At a red-shift of 10 nm from the stopband center, the $\mathcal{Q}$-factor increases to a very large value, $6.34 \cdot 10^5$ (Fig. 4.3a). Furthermore, the dependence of the $\mathcal{Q}$-factor

---

[ii] Note that the measured $\mathcal{Q}$-factors obtained with an electrically-contacted passivated sample and with an electrically-uncontacted passivated sample were similar. The latter are not shown in Fig. 4.3b.

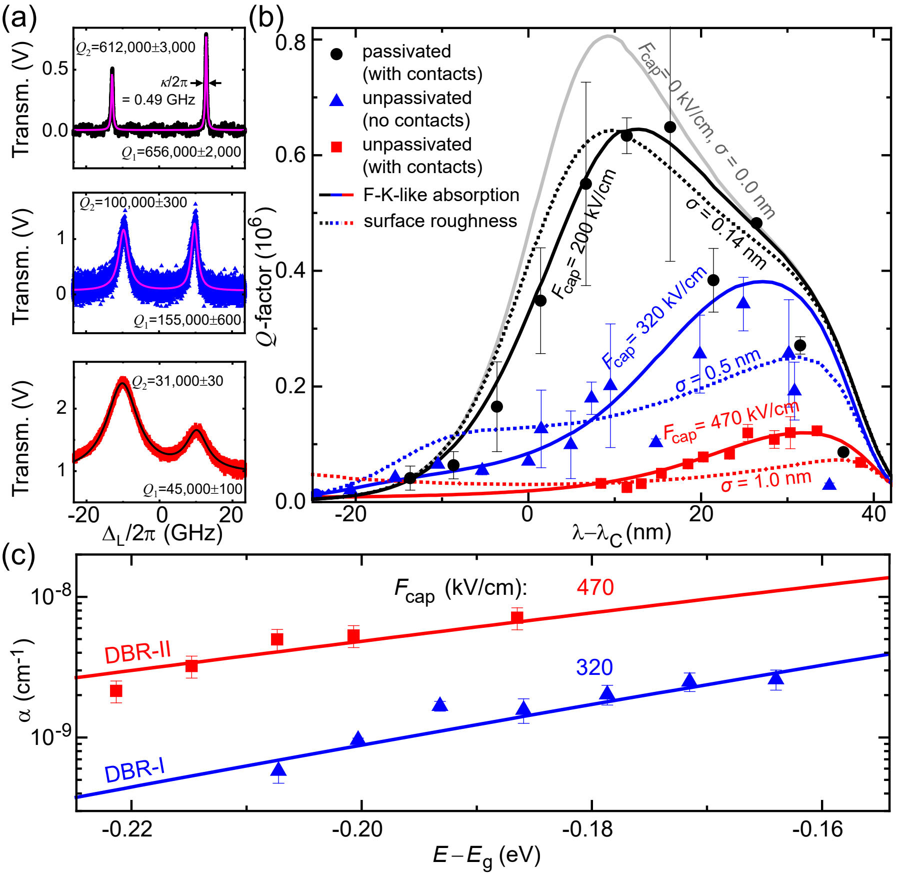

Figure 4.3: Microcavity characterization via $\mathcal{Q}$-factor measurements using: DBR-I paired with passivated nip-DBR with contacts (black dots), two unpassivated nip-DBRs without contacts (blue triangles); DBR-I (II) paired with five (one) unpassivated DBRs with contacts (red squares). (a) Measured transmission signal as a function of laser detuning at $\lambda - \lambda_C \sim 10$ nm at fixed mirror separation. The $\mathcal{Q}$-factor is determined by a double-Lorentzian fit (solid lines). (b) Evaluated $\mathcal{Q}$-factors for several wavelengths. Mean values and standard deviations originate from data from two cavity modes, and up to six measurements. Two surface-loss mechanisms are modeled: absorption and scattering. The solid lines are calculated $\mathcal{Q}$-factors taking into account free-carrier absorption (absorption coefficients from Ref.[58]) and F-K absorption[87, 88] for electric fields in the capping layer $F_{\text{cap}} = (200, 320, 470)$ kV/cm. The dotted lines are calculated taking into account surface scattering [95] only. For the passivated case, the black dotted line is modeled with a roughness at both the GaAs-alumina and alumina-vacuum interfaces $\sigma = (\sigma_{\text{GaAs-Al2O3}}, \sigma_{\text{Al2O3-vac}})$, and found to be $\sigma = (0.14, 0.14)$ nm; alternatively $\sigma = (0.0, 0.55)$ nm yields similar results. In the unpassivated cases, the blue and red dotted lines are modeled with $\sigma_{\text{GaAs-vac}} = 0.5$ nm and $\sigma_{\text{GaAs-vac}} = 1.0$ nm at the GaAs-vacuum interface, respectively. Gray solid line is model without any surface losses. (c) By comparing measured and simulated $\mathcal{Q}$-factors, and assuming that the scattering losses are negligible, the absorption coefficient α can be deduced as a function of photon energy. α is fitted to the F-K result using F_{cap} as fitting parameter.

on wavelength is much more symmetric with respect to the stopband center. In fact, the decrease on the blue-side reflects the decrease in reflectivity of the dielectric mirror which, for fabrication reasons, has a maximum reflectivity at a wavelength of 973 nm.

The passivation procedure changes the properties of the surface but leaves the rest of the microcavity unchanged. The drastic increase of the $\mathcal{Q}$-factors after surface passivation leads therefore to the conclusion that the losses limiting the $\mathcal{Q}$-factors of unpassivated microcavities are related to the semiconductor surface. Specifically, the loss, either an absorption or scattering mechanism, originates at the GaAs surface itself or in the GaAs layer immediately below the surface.

These results were verified in a second experiment employing a different piece of wafer material from the nip-DBR. The passivation was carried out in a separate run; the cavity was constructed with DBR-II as top mirror. The results are shown in Fig. 4.4. The results follow closely those of the first experiment, with the advantage that the $\mathcal{Q}$-factors could be determined also on the blue side of the stopband center.

To quantify the loss, the entire microcavity is modeled (see Sec. 4.10) using accurate descriptions of the two DBRs, including the free-carrier absorption in the doped layers in the heterostructure. Absorption is added to the capping layer (GaAs between the p-doping and the surface) and adjusted to match the experimentally determined $\mathcal{Q}$-factors at each wavelength. This is a robust procedure as the surface-related loss dominates other loss channels. The extracted absorption coefficients α from this procedure are plotted as a function of wavelength in Fig. 4.3c.

In both cases shown in Fig. 4.3c the absorption coefficients α are extremely small. From a measurement point of view, the microcavity represents a very sensitive platform for detecting very weak absorption or scattering events. In a single-pass experiment, these losses would be very difficult to detect. Significantly, we find that α depends exponentially on photon energy in the unpassivated case, a dependence that rules out scattering or broad-band absorption as the main loss mechanism at the surface, as these processes would have a much weaker dependence on wavelength. Instead, the exponential dependence points to below-gap absorption in an electric field.

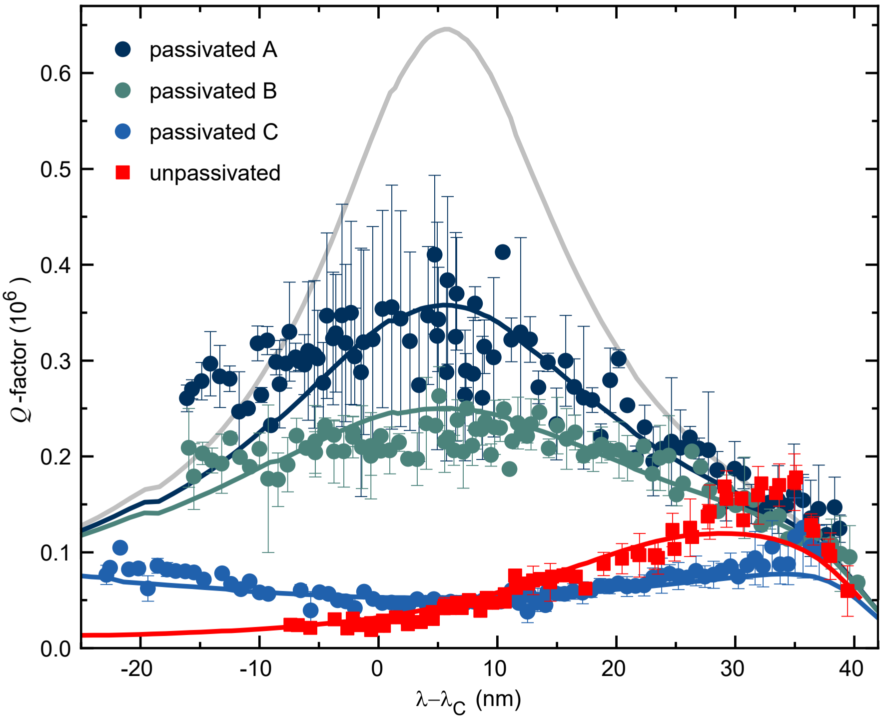

Figure 4.4: Determination of surface-related losses via $\mathcal{Q}$-factor measurements using DBR-II with an nip-DBR. We probe the double role of surface passivation. Four positions in the contacted sample are probed: three passivated areas (circles) A, B, C and an unpassivated region (red squares). Mean values and standard deviation result from the measurements on the two cavity modes. We implement a mixed model to fit the data: F-K-like absorption and reasonable values of surface roughness are probed together. For the passivated regions, surface roughness alone explains the observed data. We estimate a roughness $\sigma = (\sigma_{\text{GaAs-Al2O3}}, \sigma_{\text{Al2O3-vac}})$ for each region: at region A $\sigma = (0.5, 0.5)\,\text{nm}$, alternatively $\sigma = (0.0, 1.0)\,\text{nm}$; at region B $\sigma = (0.25, 0.8)\,\text{nm}$, alternatively $\sigma = (0.0, 1.4)\,\text{nm}$; at region C $\sigma = (0.5, 3.0)\,\text{nm}$, alternatively $\sigma = (0.0, 3.75)\,\text{nm}$. For the unpassivated region, surface roughness alone cannot account for the $\mathcal{Q}$-factor dependence on wavelength alone: with a surface roughness of $\sigma_{\text{GaAs-vac}} = 0.3\,\text{nm}$, an electric field $F_{\text{cap}} = 400\,\text{kV/cm}$ is still needed to fit data.

4.7 Investigation of loss via surface roughness

In order to confirm that the measured losses on the heterostructure with doping are indeed a consequence of the doped layers, and to quantify losses via surface scattering, we compare our results to a microcavity consisting of a semiconductor heterostructure without doping. The heterostructure in this case is a λ-layer of GaAs (with embedded InAs QDs in the center) on top of a 33-pair AlAs/GaAs DBR[64, 65, iii] It is a high-quality sample but may not match the ultra-high quality of the semiconductor heterostructure with doping. Initially, we repeat the mirror characterization procedure described above and find a suitable model for the semiconductor layer thicknesses (Fig. 4.5a). Subsequently, we pair this mirror with the dielectric top mirror DBR-I.

Figure 4.5b depicts the measured $\mathcal{Q}$-factors as a function of wavelength for the semiconductor heterostructure without doping. The $\mathcal{Q}$-factor reaches approximately 10^5 at the stopband center, and remains constant within measurement error over a wavelength range of approximately 20 nm. This behaviour is quite different to that of the unpassivated semiconductor heterostructure with doping (Fig. 4.3b,c, Fig. 4.4). The conclusion is that the strongly wavelength dependent loss process is related to the doping.

In the absence of losses, the heterostructure-without-doping – top mirror combination should yield a $\mathcal{Q}$-factor of 2×10^5 in the stopband center, about a factor of two higher than that determined experimentally (Fig. 4.5b, gray solid line). The wavelength-dependence of the $\mathcal{Q}$-factor (Fig. 4.5b) is, as before, a useful diagnostic of the scattering process. We find that in this case, scattering alone at the GaAs-vacuum interface can account for the measured $\mathcal{Q}$-factors, with a surface roughness $\sigma_{\text{GaAs-vac}} = 0.5\,\text{nm}$ (Fig. 4.5b red solid line). We simulate as well the possible outcome of passivating the undoped sample, with $\sigma = (\sigma_{\text{GaAs-Al2O3}}, \sigma_{\text{Al2O3-vac}}) = (0.5, 0.5)\,\text{nm}$, shown in Fig. 4.5b red dotted line: the addition of a thin alumina layer would diminish the effect of surface scattering due to surface roughness, increasing slightly the expected $\mathcal{Q}$-factor.

A surface roughness σ translates into a total integrated scatter (TIS) of TIS $\approx (4\pi\sigma/\lambda)^2$ (Ref.[96]) and can be modeled by an extinction coefficient k (for the 1D transfer matrix methods) according to Ref.,[95]

$$k = \frac{\pi(n_1 - n_2)^2(n_1 + n_2)d}{\lambda\sqrt{8(n_1^2 + n_2^2)}}, \tag{4.1}$$

where $d = 2\sigma$, n_1 and n_2 are the refractive indices of the two layers surrounding the scatter layer, and λ is the free-space wavelength. Including this loss in the simulations reproduces the measured $\mathcal{Q}$-factors convincingly. Furthermore, atomic force microscopy (AFM) measurements (tapping mode, Bruker Dimension 3100) indicate that surface roughness is present in different amounts

---

[iii] We note that the semiconductor heterostructure without doping was not grown with the same MBE as the semiconductor heterostructure with doping.

across samples, as shown in Fig. 4.6. The undoped wafer presented a root-

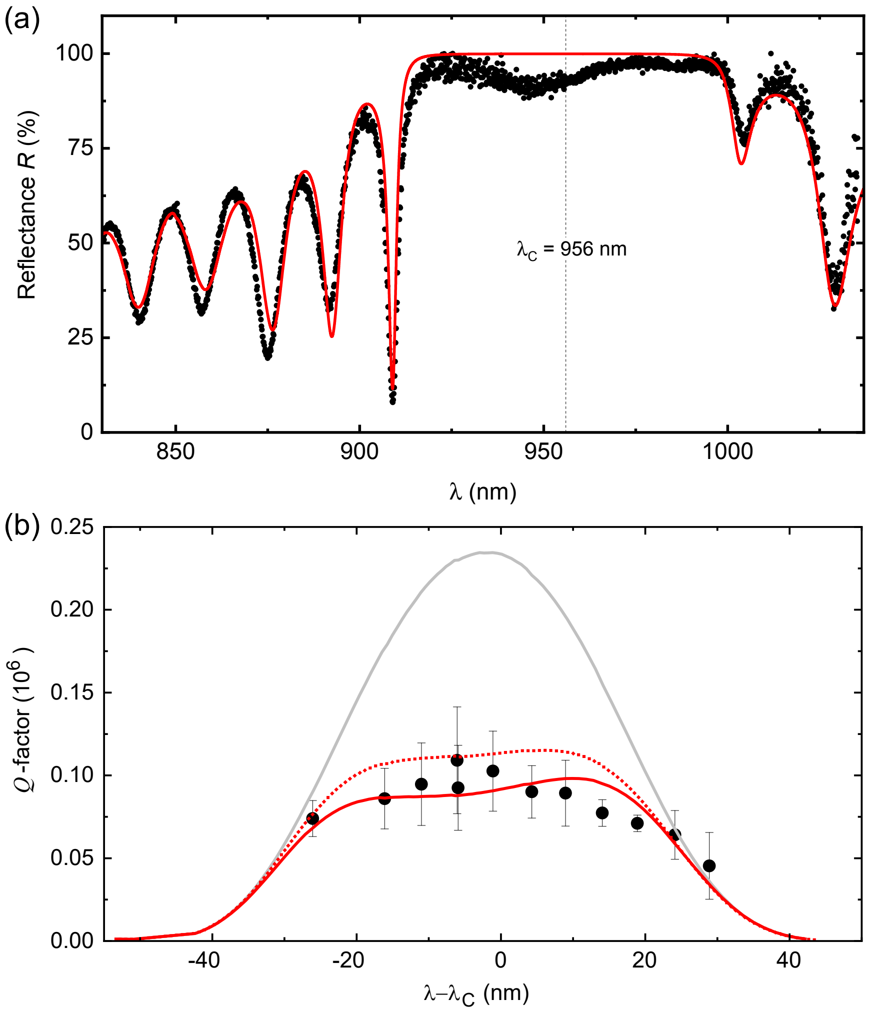

Figure 4.5: Undoped semiconductor heterostructure: reflectance and $\mathcal{Q}$-factor measurements. (a) Reflectance measurement of a semiconductor heterostructure without doping ($\lambda_C = 956\,\mathrm{nm}$) at $T = 4.2\,\mathrm{K}$. The heterostructure contains a λ-layer of GaAs on top of 33 pairs of AlAs($\lambda/4$)/GaAs($\lambda/4$). A layer of QDs is included at the center of the GaAs layer. In order to record a reference spectrum, parts of the sample were covered by an Au film using electron-beam evaporation. (b) $\mathcal{Q}$-factor of a microcavity at $T = 4.2\,\mathrm{K}$ consisting of this heterostructure without doping paired with a dielectric top mirror DBR-I, experiment (points) and simulation with a surface roughness $\sigma_{\mathrm{GaAs\text{-}vac}} = 0.5\,\mathrm{nm}$ (red solid line). The red dotted line is the expected $\mathcal{Q}$-factor on passivating the surface with a 8.0 nm-thick Al_2O_3 layer. Gray solid line corresponds to expected $\mathcal{Q}$-factor without any surface losses.

mean-square (rms) surface roughness $0.3 \leq \sigma \leq 0.7$ nm, the unpassivated bare sample (without contacts) presented $0.2 \leq \sigma \leq 0.9$ nm, the unpassivated contacted sample $0.4 \leq \sigma \leq 7.3$ nm, and the passivated sample $0.3 \leq \sigma \leq 1.9$ nm. The native surface roughness at the GaAs-vacuum interface, right after growth of the samples, is on the order of 0.15 to 0.30 nm. However, increased roughness is caused by processing of the samples – e.g. via passivating, cleaning and gluing, bonding. We speculate that in the unpassivated contacted samples, presented high values of surface roughness might be induced by remnant traces of photoresist from the processing procedure (which in turn have a lowering scattering power than pure GaAs, due to the reduced refractive index).

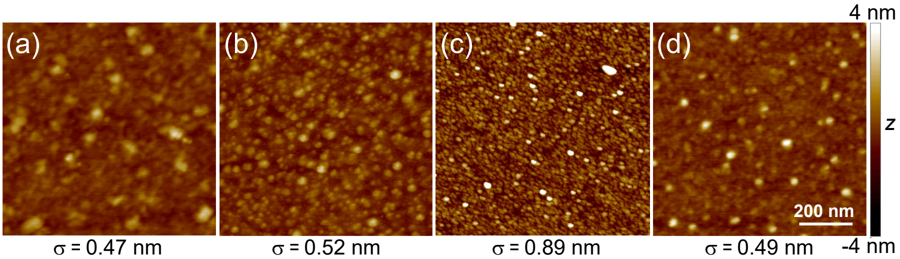

Figure 4.6: Atomic force microscropy (AFM) images of different semiconductor samples. Each image depicts the same scan area of $0.8 \times 0.8\,\mu\mathrm{m}^2$ (obtained in tapping mode) and scale bar from a height of -4 to $+4$ nm. (a) Piece of passivated wafer. The rms surface roughness measured on several similar sample locations lies in the range $0.3 \leq \sigma \leq 1.9$ nm. (b) Piece of unpassivated bare wafer. Range of surface roughness for similar sample locations is $0.3 \leq \sigma \leq 0.7$ nm. (c) Unpassivated sample with contacts. Similar samples present $0.4 \leq \sigma \leq 7.3$ nm. (d) Piece of unpassivated bare wafer from a semiconductor DBR without n- and p-type layers. Different sample locations presented surface roughness ranging between $0.2 \leq \sigma \leq 0.9$ nm.

The passivated doped sample also provided an opportunity to test the applicability of the TIS result for loss at a rough interface. The $\mathcal{Q}$-factors measured with DBR-II at three different passivated regions of the sample presented a weak dependence on wavelength, in contrast to the results in the unpassivated region. The model with $\sigma = (0.5, 0.5)$ nm, $\sigma = (0.25, 0.8)$ nm and $\sigma = (0.5, 3.0)$ nm respectively for regions A, B and C reproduce these $\mathcal{Q}$-factors precisely, with reasonable values of roughness at each interface (Fig. 4.4). Furthermore, the model captures the symmetric influence of roughness on the $\mathcal{Q}$-factor with respect to the stopband center. This results from the reduction in the MCF at the sample's surface, as presented in Fig. 4.1c. Agreement between the $\mathcal{Q}$-factors and the simulation gives us confidence that the description of loss via surface scattering is quantitatively correct.

The conclusion from this measurement and analysis is that, not only passivating the surface quenches surface-related absorption, but also has the beneficial aspect of reducing loss via surface scattering. The original GaAs surface and the passivated surface have a similar range of values of surface roughness. In the passivated case, the surface loss via scattering is about 60% with respect to that of the unpassivated sample. The passivation procedure creates a layer with an intermediate refractive index: it avoids the large jump in refractive index at a GaAs-vacuum interface. This reduces the total scattering loss.

In the case of the doped unpassivated sample, the wavelength dependence of the $\mathcal{Q}$-factors is too strong to be accounted for with scattering loss (Fig. 4.3b and Fig. 4.4). A different mechanism is clearly at play.

4.8 Microscopic explanation for the nip-DBR losses

We give a possible microscopic explanation for the losses in the investigated nip-DBR structure and why surface passivation significantly reduces them. In Fig. 4.7a, the calculated valence- and conduction-band edges in the heterostructure are shown, a solution to the 1D Poisson equation (obtained via the nextnano software). In the unpassivated case, we simulate the mid-gap Fermi-level pinning at the surface via a Schottky barrier of 0.76 eV. This yields an electric field in the capping layer ("capping field") of $F_{\text{cap}} = 140\,\text{kV/cm}$.

An electric field in a semiconductor leads to F-K absorption below the bandgap of the material:[84, 85] owing to the position-dependence of the band-edges, the electron and hole wavefunctions can be described by Airy functions (similar to a particle in a triangular well[97]) and acquire an exponential tail at energies within the bandgap. The electric field therefore creates an absorption processes at photon energies $E_{\text{photon}} < E_{\text{g}}$. The situation is schematically depicted in Fig. 4.7b.

According to the standard model,[86] F-K absorption at photon energy E due to the presence of an electric field F can be described via the absorption coefficient

$$\alpha(E,F) = \beta \cdot \frac{F^{1/3}}{E} \sum_{i=\text{lh,hh}} \left(\frac{\mu_i}{m_0}\right)^{4/3} \cdot |M_i|^2 \Big(|\text{Ai}'(x_i)|^2 - x_i |\text{Ai}(x_i)|^2\Big), \quad (4.2)$$

where

$$x_i = \frac{e \cdot (E_{\text{g}} - E)}{\hbar\theta_i}, \quad (4.3)$$

$$\hbar\theta_i = \Big(\frac{(eF\hbar)^2}{2\mu_i}\Big)^{1/3}. \quad (4.4)$$

In these equations, β is a constant (arbitrary units), e is the elementary charge (in SI units), $\hbar$ the reduced Planck's constant (in SI units), m_0 the free electron rest mass (in kg), $\mu_{\mathrm{lh}} = 0.037m_0$ ($\mu_{\mathrm{hh}} = 0.058m_0$) the reduced mass of an electron–light-hole pair (electron–heavy-hole pair), F is given in kV/cm, the energies E_g and E in eV and $|M_{\mathrm{lh}}|^2$ ($|M_{\mathrm{hh}}|^2$) the momentum matrix elements for the light-hole (heavy-hole). $\mathrm{Ai}(z)$ is an Airy function[iv] (with derivative $\mathrm{Ai}'(z)$).

We make use of the momentum matrix elements derived in Ref.[87] for different polarizations of the radiation field. For light polarized in the (x, y)-plane, the momentum matrix elements for the light- and heavy-holes read

$$|M_{\mathrm{lh}}|^2 = P^2/3, \tag{4.5}$$

$$|M_{\mathrm{hh}}|^2 = P^2, \tag{4.6}$$

where $P = 0.692$ (arbitrary units) is a typical value for GaAs.[87]

We use this model for F-K absorption to describe previously reported room-temperature experiments on a p-i-n double heterostructure[88] (Fig. 4.7c), and extract the value of constant β in Eq. 4.2, which is found to be $\beta = 2.5 \cdot 10^4$ (arbitrary units). These experiments extend to photon energies far below

---

[iv] The Airy function is defined as $\mathrm{Ai}(z) = \frac{1}{2\pi}\int_{-\infty}^{\infty} e^{i(zt+t^3/3)}dt$.

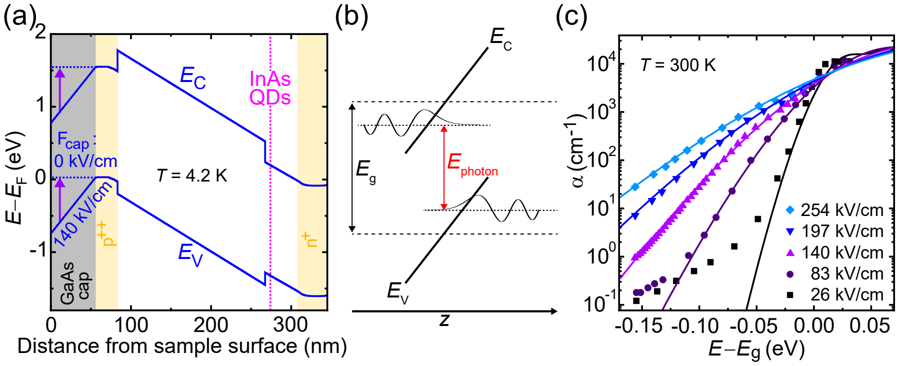

Figure 4.7: Band structure and Franz-Keldysh effect. (a) Simulation of the conduction and valence bands in the n-i-p diode (nextnano) at $T = 4.2\,\mathrm{K}$. The surface is modeled via a Schottky barrier of $E_g/2 = 0.76\,\mathrm{eV}$ reflecting the mid-gap Fermi-level pinning at the GaAs surface.[90] The effect of surface passivation is to eliminate the electric field at the capping layer. (b) Schematic of the F-K effect.[84,85] An electric field applied to a semiconductor allows both electrons and holes to tunnel into the forbidden energy, leading to below-gap absorption processes. (c) Room-temperature F-K absorption coefficients for different electric fields within a p-i-n double heterostructure (©2020 IEEE. Reprinted, with permission, from Ref.[88]). The solid lines correspond to the calculated absorption coefficients according to Ref.[86,87] (Eqs. 4.2–4.6).

the bandgap, the case of interest here. There is a compelling overlap between theory and experiment.

In order to estimate F-K absorption coefficients in our nip-DBR at 4.2 K (Fig. 4.3b,c and Fig. 4.4), we make use of Eqs. 4.2–4.6, taking the low-temperature GaAs bandgap of 1.519 eV and β extracted from fitting the data in Fig. 4.7c. We compare the results of the model for low-temperature F-K absorption to the experimental data presented in Fig. 4.3b,c, taking the electric field F as a fitting parameter. The exponential dependence of the absorption on the photon energy is well described with F-K absorption. However, in the unpassivated case, the capping field is $F_{\text{cap}} = 470\,\text{kV/cm}$ when not accounting for any surface roughness (Fig. 4.3) and $F_{\text{cap}} = 400\,\text{kV/cm}$ when accounting for a realistic value of surface roughness (Fig. 4.4). These values are between 3.4 and 2.8 above that expected from the 1D Poisson equation (Fig. 4.7a) respectively. The origin of this discrepancy is not understood at this point, but we note several points.

First, to the best of our knowledge, there are no F-K absorption experiments reported in the literature at low temperature (4.2 K) and at photon energies far below the bandgap E_{g} of GaAs (at $E - E_{\text{g}} \sim -0.17\,\text{eV}$ corresponding to $\lambda \sim 920\,\text{nm}$). Our approach here is to fit the theory presented in Ref.[86, 87] to the room temperature experiments of Ref.[88] (Fig. 4.7c) and then to extrapolate the absorption coefficients to photon energies $\sim 0.17\,\text{eV}$ below the bandgap. The change in temperature, from room-temperate to low temperature, is accommodated by a rigid shift in the absorption spectrum to account for the increase in the bandgap. It is conceivable that the standard F-K theory is inadequate at photon energies far below the bandgap – this point has not been tested experimentally.

Secondly, there are room-temperature experiments on F-K oscillations in doped GaAs heterostructures (a 25–80 nm thick, undoped GaAs capping layer on top of an n^+-doped $\text{Al}_{.32}\text{Ga}_{.68}\text{As}$ layer[98]) that also report surface electric field values a factor 1.8–3.8 above the expected ones[v].

Thirdly, the F-K model describes a bulk semiconductor in a uniform electric field. Obviously, it does not take into account the microscopic details of the surface, for instance surface reconstructions and oxidation. It is possible that the details of the surface layer are important here.

In the light of this analysis, our proposal is that surface passivation quenches surface-related absorption primarily by reducing the electric field in the capping

---

[v] In order to estimate the capping fields in Ref.,[98] we assume mid-gap pinning, dividing half the bandgap $E_{\text{g}}/2 = 0.71\,\text{eV}$ of GaAs at 300 K by the capping layer thicknesses there reported.

layer, thereby eliminating the F-K absorption (within the sensitivity of the experiment).

A remaining question is why the bare-wafer sample without passivation shows higher $\mathcal{Q}$-factors than the electrically contacted sample also without passivation (Fig. 4.3b,c). The contacting process may change the surface roughness, as revealed by the AFM measurements (Fig. 4.6). The surface roughness per se does not however account for the $\mathcal{Q}$-factors of the various samples. The main point is that surface scattering does not account for the exponential dependence of the loss process on photon energy (Fig. 4.3b,c). Instead, we speculate that the change in GaAs surface on forming the contacts results in a change of surface pinning, thereby increasing the capping field. One possibility is that the degradation of the surface on contacting spreads the available surface states to lower energies.

4.9 Model for the curved dielectric mirrors

An interpretation of the microcavity $\mathcal{Q}$-factors in terms of losses in the semiconductor heterostructure rests on an understanding of the top mirror. The top mirrors, dielectric-DBRs, are of very high quality with very low loss. To prove this point, we investigate a microcavity formed from DBR-I and a planar version of DBR-I. The coatings for the plane mirror and concave mirrors were applied to the substrates in the same run and are nominally identical. Fig. 4.8 shows the measured $\mathcal{Q}$-factors. At the stopband center of the top mirror ($\lambda_C = 976\,\text{nm}$), the $\mathcal{Q}$-factor is extremely high, $1.5 \cdot 10^6$. To describe the dielectric mirror accurately at the stopband center of the semiconductor-DBR, we analyze the dependence of the dielectric-dielectric $\mathcal{Q}$-factor and transmission as a function of wavelength. To describe the high transmission at short wavelengths, we are forced to red-shift the stopband center of the bottom mirror by 3 nm[vi]. A rough interface at the “lower” surface of the five “lowest” Ta_2O_5 layers shown in Fig. 4.1 (extinction coefficients corresponding to an interface roughness[95] of 0.25 nm) together with an increased absorption within the “lowest” Ta_2O_5 layer (extinction coefficient $k = 4k_{\text{Ta2O5}}$, where k_{Ta2O5} is defined in Sec. 4.10) are heuristically introduced in the model in order to describe the measured $\mathcal{Q}$-factors. This fit is very convincing (Fig. 4.8). This description of the top dielectric-mirror DBR-I is used to interpret the measurements on microcavi-

---

[vi] We note that reflectance spectra (Fig. 4.2a) on different samples with nominally the same dielectric coating exhibited up to 6 nm shifts in wavelength, most probably due to thickness variations across the wafer.

ties formed using the semiconductor-DBRs as bottom mirror (Fig. 4.3b,c and Fig. 4.5b).

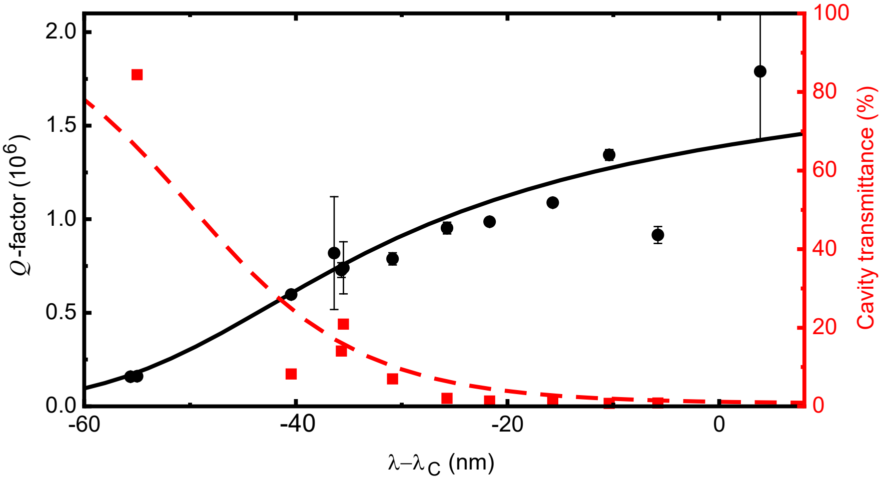

Figure 4.8: Measured $\mathcal{Q}$-factors and cavity transmittance of a purely dielectric microcavity. Dielectric top mirror ($\lambda_C = 973\,\mathrm{nm}$) paired with a dielectric bottom mirror (shifted to $\lambda_C = 976\,\mathrm{nm}$, nominally the same coating) at $T = 300\,\mathrm{K}$. The cavity transmittance is measured by relating the transmitted power at the cavity resonance to the laser power before the objective lens multiplied by a fitted in-coupling efficiency of 59%. The black solid (red dashed) line is a calculation of the $\mathcal{Q}$-factor (cavity transmittance) taking into account a material extinction coefficient of $k_{\mathrm{SiO2}} = 4 \cdot 10^{-7}$ and $k_{\mathrm{Ta2O5}} = 4.5 \cdot 10^{-7}$ for $\mathrm{SiO_2}$ and $\mathrm{Ta_2O_5}$, respectively.[99] Additionally, an interface roughness of $\sigma = 0.25\,\mathrm{nm}$ above each of the five last grown $\mathrm{Ta_2O_5}$ layers and $k = 4k_{\mathrm{Ta2O5}}$ in the last-grown $\mathrm{Ta_2O_5}$ layer are introduced heuristically in order to fit the experimental data.

4.10 1D transfer matrix model

We list the relevant parameters used for the $\mathcal{Q}$-factor calculations via a one-dimensional transfer-matrix method.

Extinction coefficients in the different materials are introduced as follows. For DBR-I, $k_{\mathrm{SiO2}} = 4 \cdot 10^{-7}$ for $\mathrm{SiO_2}$ (Ref.[99]), $k_{\mathrm{Ta2O5}} = 4.5 \cdot 10^{-7}$ for $\mathrm{Ta_2O_5}$ (Ref.[99]), and $k = 4k_{\mathrm{Ta2O5}}$ is used for the "lowest", i.e. the last-grown, $\mathrm{Ta_2O_5}$ layer (the layer closest to the vacuum-gap). For DBR-II, $k_{\mathrm{SiO2}} = 4 \cdot 10^{-6}$ for $\mathrm{SiO_2}$, $k_{\mathrm{Ta2O5}} = 4.5 \cdot 10^{-6}$ for $\mathrm{Ta_2O_5}$ (from fitting data taken with curved DBR-II and planar DBR-I microcavity). Finally, for the semiconductor nip-DBR, $k_{\mathrm{p++}} = 5.2 \cdot 10^{-4}$ for $\mathrm{p^{++}}$-GaAs, $k_{\mathrm{p+}} = 1.9 \cdot 10^{-4}$ for $\mathrm{p^{+}}$-GaAs, and

$k_{\mathrm{n+}} = 0.7 \cdot 10^{-4}$ for n^{+}-GaAs.[58] An extinction coefficient of $k = \alpha_{\mathrm{FK}}\lambda/(4\pi)$, where α_{FK} is a F-K absorption coefficient, is introduced in the capping layer; α_{FK} depends on the electric field. Surface roughness is described by introducing an additional layer of thickness $d = 2\sigma$, where σ is the rms surface/interface roughness.[95]

In analogy to the experiment, a $\mathcal{Q}$-factor is determined for a fixed "vacuum-gap" layer thickness by calculating a cavity transmittance spectrum. A Lorentzian fit to the calculated spectrum is used to determine the resonance frequency as well as the $\mathcal{Q}$-factor. This procedure is repeated for different vacuum-gaps, yielding a plot of $\mathcal{Q}$-factor versus wavelength. The resulting $\mathcal{Q}$-factors are presented in Fig. 4.3, Fig. 4.4, Fig. 4.5 and Fig. 4.8.

4.11 Conclusion

Significant surface-related losses in an open microcavity consisting of an nip-DBR and dielectric DBR are much reduced by passivating the GaAs surface. The passivation works primarily by eliminating the Franz-Keldysh-like absorption in the capping layer. Secondary benefit of the passivation is to reduce loss by surface scattering. With passivation, $\mathcal{Q}$-factors close to 10^6 can be achieved.

5

A NEAR-IDEAL SINGLE PHOTON SOURCE

Adapted from:

N. Tomm*, A. Javadi*, N. O. Antoniadis, D. Najer, M. C. Löbl, A. R. Korsch, R. Schott, S. R. Valentin, A. D. Wieck, A. Ludwig and R. J. Warburton,

“A bright and fast source of coherent single photons”,

Nature Nanotechnology **16**, 399 (2021)

5.1 Summary

A single photon source is an enabling technology in device-independent quantum communication,[100] quantum simulation,[51, 101] linear optics-based[102] and measurement-based quantum computing.[103] These applications employ many photons and place stringent requirements on the efficiency of single photon creation. The scaling on efficiency is typically an exponential function of the number of photons. Schemes taking full advantage of quantum superpositions also depend sensitively on the coherence of the photons, i.e. their indistinguishability.[104] Here, we report a single-photon source with a high end-to-end efficiency. We employ gated quantum dots in an open, tunable microcavity.[54] The gating provides control of the charge and electrical tuning of the emission

frequency, the high quality material ensures low noise, and the tunability of the microcavity compensates for the lack of control in quantum dot position and emission frequency. Transmission through the top mirror is the dominant escape route for photons from the microcavity, and this output is well-matched to a single-mode fiber. With this design, we can create a single photon at the output of the final optical fiber on-demand with a probability of 57% and with an average two-photon interference visibility of 97.5%. Coherence persists in trains of thousands of photons with single photon creation at a repetition rate of 1 GHz.

5.2 Introduction

A single emitter can be used as a single photon source. Unlike a cold atom or ion in vacuum,[12, 13] a semiconductor quantum dot is naturally trapped in space. Photonic engineering on a nano- or micro-scale is required to funnel the photons into one specific mode and to couple the photons from this mode into a single-mode fiber.[105] There are two established techniques. First, in a resonant microcavity, photons are emitted preferentially into the microcavity mode (the Purcell effect), and in an asymmetric microcavity, photon leakage from the microcavity acts as an out-coupler. Much success has been achieved with micropillars.[39, 40, 106] Second, in an on-chip waveguide, photons are emitted preferentially into a laterally-propagating mode.[17, 36] In terms of the end-to-end efficiency a record of 24% has been achieved with a quantum dot in a micropillar.[40]

Coherence depends sensitively on the noise in the device. Despite the complexity of the solid-state environment, quantum dot-based single photon sources have demonstrated close-to-unity coherence for the interference of successively-emitted photons.[39, 106] Ultimately, the coherence is limited by exciton-phonon scattering, but with a careful choice of microcavity, two-photon interference visibilities as high as 99% are predicted.[43] Experimentally, the coherence tends to drop on time-scales of a few hundred nanoseconds, for instance from 96% to 92%.[106] This is most likely a consequence of charge noise which results in a fluctuating emission frequency. Charge noise can also result in telegraph noise should the charge state of the quantum dot itself fluctuate – this problem can be solved by working with a gated device in which the quantum dot charge is locked by Coulomb blockade.[16] An additional benefit of a gated device is that, within a charge plateau, the emission frequency can be fine-tuned electrically via the Stark effect. With resonant excitation on a gated device of very high material quality, the charge noise has been shown to be extremely low.[30]

5.3 Semiconductor quantum dot in a microcavity

Here, we take the microcavity-route to generating single photons from single quantum dots, employing low-noise gated material. In the generic case (Jaynes-Cummings Hamiltonian with atom-cavity coupling g, cavity loss-rate κ, atom decay-rate into non-cavity modes γ), $\beta = F_{\mathrm{P}}/(F_{\mathrm{P}}+1)$ where the Purcell factor is $F_{\mathrm{P}} = 4g^2/(\kappa\gamma)$. Cavity loss channels comprise exit through the top mirror (rate κ_{top}) and unwanted loss processes (rate κ_{loss}), such as absorption, scattering and diffraction to the side: $\kappa = \kappa_{\mathrm{top}} + \kappa_{\mathrm{loss}}$. The conversion efficiency of an exciton in the quantum dot to a photon exiting the top mirror of the cavity is $\eta = \beta \cdot \kappa_{\mathrm{top}}/(\kappa+\gamma)$. For fixed g, γ and κ_{loss}, η exhibits a broad maximum around the condition $\kappa_{\mathrm{top}} = \sqrt{(1+\kappa_{\mathrm{loss}}/\gamma)(4g^2+\kappa_{\mathrm{loss}}\gamma)}$. Taking $g \gg (\kappa_{\mathrm{loss}}, \gamma)$, $\kappa_{\mathrm{opt}} \simeq 2g\sqrt{1+\kappa_{\mathrm{loss}}/\gamma}$. Taking a quantum dot with transform-limited linewidth ($\gamma/(2\pi) = 0.3\,\mathrm{GHz}$) in an open microcavity ($g/(2\pi) = 4.3\,\mathrm{GHz}$ and $\kappa_{\mathrm{loss}}/(2\pi) = 0.72\,\mathrm{GHz}$),[54] matching the condition on κ_{top} implies an efficiency η as high as 90% (Fig. 5.1b).

We use an open cavity,[54, 64, 73] a highly miniaturized Fabry-Perot cavity (Fig 5.1a). The top mirror has a concave shape and is micro-machined into a silica substrate; the bottom mirror is a highly reflective planar mirror, part of the semiconductor heterostructure.[64] Quantum dots in this structure exhibit close-to-transform-limited linewidths ($\gamma/(2\pi) = 0.30\,\mathrm{GHz}$).[54] To determine the unwanted photon loss-rate from the cavity, κ_{loss}, we employ a highly reflective, extremely low-loss top-mirror keeping the mirror radius the same. With the same heterostructure and processing procedure, but with the highly reflective top mirror, we measure a high $\mathcal{Q}$-factor at the stopband center, $\mathcal{Q} = (4.5 \pm 0.5) \times 10^5$ (as described in Chapter 2 and Fig. 2.1). We obtain an upper bound to $\kappa_{\mathrm{loss}}/(2\pi)$ of $(0.72 \pm 0.07)\,\mathrm{GHz}$ if we assume that only the unwanted losses determine the $\mathcal{Q}$-factor. This low value of κ_{loss} arises on account of the low absorption rate in the semiconductor heterostructure[54] and is only compatible with low diffraction losses. We verify this point by calculating the $\mathcal{Q}$-factor as a function of the mirror radius of curvature, R. These simulations presented in Chapter 2, Fig. 2.2 show that diffraction losses reduce the $\mathcal{Q}$-factor only for $R \lesssim 6$ μm. At the radius of curvature used here, $R = 12$ μm, the calculated $\mathcal{Q}$-factor is 99% of the $\mathcal{Q}$-factor in the large-R limit. These simulations back up the experimental result that κ_{loss} is small. With the highly reflective top mirror, the quantum dot–cavity system enters the strong coupling regime of cavity-QED[54] allowing a precise measurement of the coupling, $g/(2\pi) = 4.3$ GHz. In the experiments reported here, we use a modest reflectivity top mirror (transmission 10,300 ppm per round-trip according to the design) chosen such that κ lies close to the efficiency maximum (Fig. 5.1b). The measured $\mathcal{Q}$-factor is 12,600 ($\kappa/(2\pi) = 25.92$ GHz), matching closely the value expected from the design of the two mirrors in the large-R limit. This analysis shows that $\kappa_{\rm loss}/(\kappa+\gamma) \simeq 3\%$.

The semiconductor heterostructure contains thin n- and p-type layers with the quantum dots in tunnel contact with the n-type layer such that Coulomb blockade is established. Contacts to the n- and p-type layers are made at the edge of the chip, far from the microcavity itself. The chip is positioned relative to the top mirror *in situ* (Fig. 5.1a).

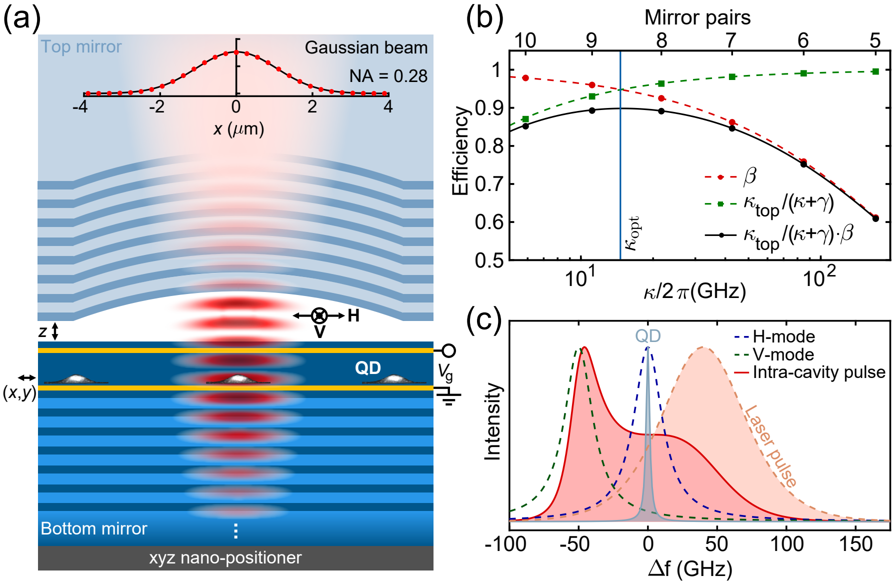

Figure 5.1: Concept of the single photon source. (a) The semiconductor heterostructure consists of a GaAs/AlAs Bragg mirror, the bottom mirror, and a p-i-n diode. The InGaAs quantum dots are located in the intrinsic region, in tunnel-contact with the Fermi sea in the n-layer. The position of the heterostructure can be adjusted (↔, ↕) with respect to the top mirror, a concave mirror in a silica substrate, using an XYZ-nanopositioner. A simulation (red points) shows that the output is very close to a Gaussian beam (black line, R^2=99.95%). (b) Calculated conversion efficiency, quantum dot exciton to photon exiting the top mirror, as a function of the decay rate through the top mirror $\kappa_{\rm top}$ for "atom"-photon coupling $g/(2\pi) = 4.3$ GHz, atom decay rate $\gamma/(2\pi) = 0.30$ GHz and rate of unwanted loss $\kappa_{\rm loss}/(2\pi) = 0.72$ GHz. The efficiency η is given by $\eta = \kappa_{\rm top}/(\kappa+\gamma)\cdot\beta$ (with $\kappa = \kappa_{\rm top} + \kappa_{\rm loss}$); $\beta = F_{\rm P}/(F_{\rm P}+1)$ with $F_{\rm P} = 4g^2/(\kappa\gamma)$. The number of mirror pairs refers to the top mirror. (c) Excitation scheme. The quantum dot is in resonance with the H-polarized microcavity mode; the laser is blue-detuned and V-polarized. The driving intensity as experienced by the quantum dot is shown.

A challenge in all optically-driven quantum dot single photon sources is to separate the single photon output from the driving laser light. A standard scheme is to excite and detect in a cross-polarized configuration. Applied to a charged exciton for which the transitions are circularly polarized, this scheme leads to a 50% loss in the collection efficiency. Here, we avoid this loss by exploiting the mode-splitting in the microcavity.[40] We work with the positively-charged exciton, X^+, which has circularly-polarized transitions (σ^+ for hole spin-$\Downarrow$, σ^- for hole spin-$\Uparrow$). The microcavity mode splits into two modes, H- and V-polarized, separated by 50 GHz, on account of a small birefringence arising mostly from some residual uniaxial strain in the semiconductor (Chapter 6); the spectrum of the laser pulses is larger than this splitting (Fig. 5.1c). The quantum dot is tuned into resonance with the higher-frequency, H-polarized mode. The laser is V-polarized and blue-detuned with respect to both microcavity modes such that the tails of the laser spectrum and the V-polarized microcavity mode overlap at the frequency of the H-polarized mode (Fig. 5.1c). The quantum dot emits preferentially into the H-polarized microcavity mode. The cross-polarized scheme (suppression 10^6 for pulsed excitation) now separates the V-polarized laser pulses from the H-polarized single photons with a loss depending only on the unwanted coupling of the quantum dot to the V-polarized mode (Chapter 2, Sec. 2.6). Provided that the mode-splitting is larger than the mode linewidths,[40] this loss is small.

5.4 Photon flux and end-to-end efficiency

We choose a quantum dot and maximize the coupling of the X^+-resonance to the microcavity. To do this, we record a decay curve following resonant excitation: the radiative decay rate is largest at maximum coupling. The quantum dot and microcavity frequencies are tuned to establish a resonance (Fig 5.2a). The Purcell-factor F_{P} is determined by scanning the microcavity frequency: on resonance with a microcavity mode, the decay time is 47.5 ps; far detuned, the decay time tends to 520 ps, resulting in $F_{\mathrm{P}} = 10$ for QD1 (12 for QD6) (Fig 5.2b). On resonance with the H-polarized microcavity mode, we determine β_{H}, the probability of emission into the H-polarized mode, to be $\beta_{\mathrm{H}} = 86\%$ (Fig 5.2b).

We now maximize the flux of single photons. Implementing the excitation scheme (Fig 5.1c), the central frequency of the laser is tuned to find the maximum signal. As a function of laser power, the quantum dot signal exhibits oscillations, indicative of Rabi oscillations (Fig 5.2c).

The main new feature over previous experiments is the high end-to-end efficiency Σ of the source. Σ is neither the β-factor of the microcavity nor the efficiency

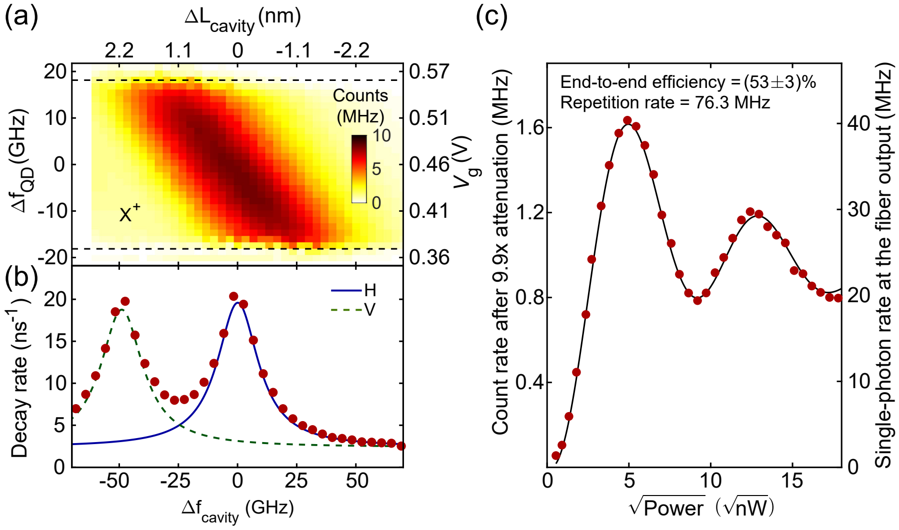

Figure 5.2: Measured flux of single photons (a) Quantum dot (QD1) signal versus z-piezo voltage (microcavity detuning) and bias voltage (quantum dot detuning). The positively charged trion X^+ is resonant with the microcavity; the dashed lines denote the boundaries of the Coulomb blockade plateau. The signal was recorded on a silicon detector at $\sqrt{P} = 3.13\ \sqrt{\text{nW}}$ (P is the laser power). The measurement is taken in a nonlinear regime of the photodetector. (b) Radiative decay rate (following pulsed resonant excitation) versus microcavity detuning for constant bias and constant (x, y)-position. The total Purcell factor F_P is determined to be 10 implying $\beta = 91\%$. Via Lorentzian fits, the β-factor specific to the H-polarized mode is determined: $\beta_H = 86\%$. (c) Measured signal versus square root of laser power for zero microcavity-X^+ detuning. The laser repetition frequency is 76.3 MHz; the detector has an efficiency of $(42 \pm 3)\%$. The signal is deliberately attenuated by a factor of 9.9 (left y-axis). The right y-axis shows the expected signal without the attenuation and with a perfect detector. The solid-line is the result of the calculation describing the response of the quantum dot to the driving field (Fig 5.1c).

after the first lens, both commonly used metrics. Instead, the end-to-end efficiency describes the efficiency of the entire chain: exciton creation, generation of a photon in the H-polarized microcavity mode, out-coupling of this photon through the top mirror, and finally transmission through the entire optical system. In other words, following excitation with a laser pulse, we obtain a single photon at the output of the collection fiber (a standard optical fiber) with a probability Σ. We determine Σ from the photon flux. At a repetition frequency of 76.3 MHz, we attenuate the beam by a factor of 9.9 (to avoid saturating the detector) and measure the count rate (Fig 5.2c). Taking account of the detector efficiency and a small non-linearity in the detector's response (described in detail in Chapter 2), we determine $\Sigma = (53 \pm 3)\%$ for QD1 ($\Sigma = (57 \pm 3)\%$ for QD6). We repeat the experiment by reducing the operation rate of the laser, employing a “pulse-picking” setup, in order to avoid the detector’s saturation and non-linear regimes. At a repetition frequency of 4.24 MHz the same end-to-end efficiency of $(57 \pm 3)\%$ at the equivalent π-power is measured for QD6 (Fig. 5.3a,b). A direct observation of the single photon flux and two-photon events is performed in Fig. 5.3c.

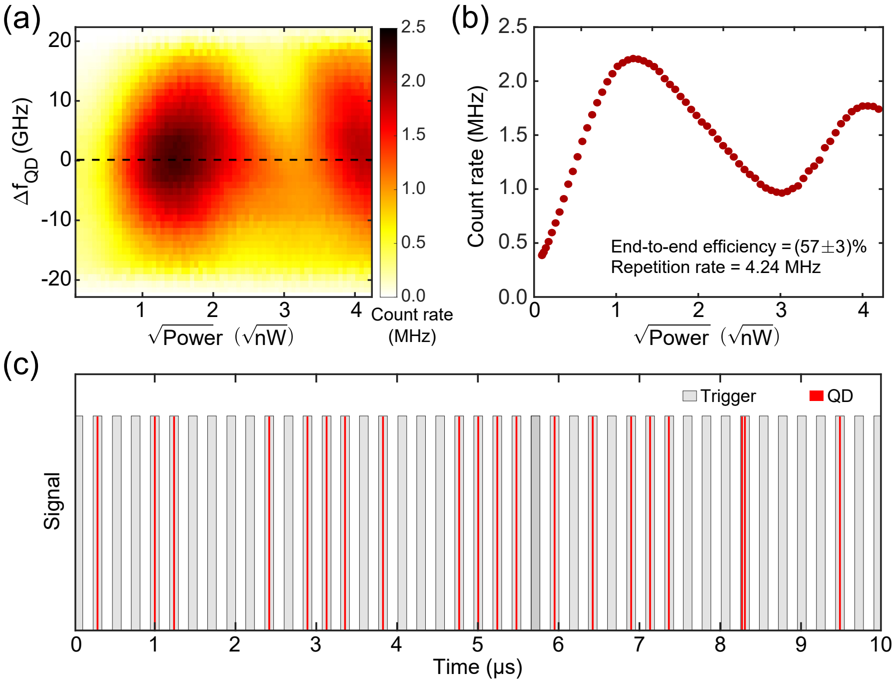

Figure 5.3: Single photon source efficiency measured at reduced operation rate. (a) Measured QD6 signal versus square root of laser power and detuning from QD resonance. The laser repetition frequency is reduced to 4.24 MHz in order to avoid saturation and non-linearities in the detector. The detector has an efficiency of $(82 \pm 5)\%$. The dashed line outlines the zero microcavity-X^+ detuning. (b) Cut-through measurement across the dashed line in (a). The deduced end-to-end efficiency for this QD is $\Sigma = (57 \pm 3)\%$. (c) Time-tag signal of excitation laser trigger (gray columns) and the signal from the quantum dot (red lines) over a period of 10 μs. The single photon flux and the presence of two-photon states, due to re-emission process, is directly observed.

5.5 Single photon purity and indistinguishability

The laser power is set at the maximum signal corresponding to the best implementation of a π-pulse. An intensity auto-correlation measurement demonstrates clear photon anti-bunching and a high purity of single photon generation, $g^{(2)}(0) = 2.1\%$ for QD1 (Fig 5.4a). The purity is limited by a small amount of laser light leaking into the detection channel (0.3% of total signal) and double-excitation events.

The coherence of the single photons is probed with two-photon interference, a Hong-Ou-Mandel (HOM) experiment. On creating two photons 1 ns apart in time, the HOM visibility is 91.6% (Fig 5.4b). Correcting for a small imperfection in the HOM interferometer, $V_{\text{raw}} = 92.5\%$. The HOM visibility is negatively

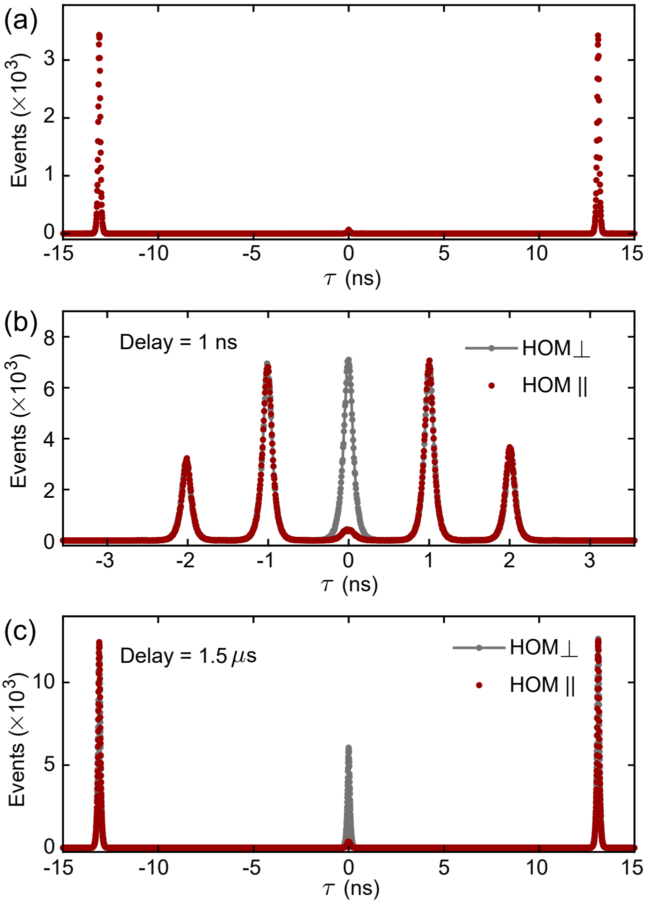

Figure 5.4: Quantum-optics characterization of the single photon source. (a) Autocorrelation $g^{(2)}$ versus delay τ (QD1): $g^{(2)}(0) = (2.1 \pm 0.1)\%$ (b), (c) Hong-Ou-Mandel (HOM) experiment (QD1) showing two-photon interference for photons created 1 ns and 1.5 μs apart in time, (b) and (c), respectively. For a delay of 1 ns, $V_{\text{raw}} = (91.6 \pm 0.1)\%$ ($V = (96.0 \pm 0.5)\%$); for a delay of 1.5 μs, $V_{\text{raw}} = (91.3 \pm 0.1)\%$ ($V = (97.5 \pm 0.5)\%$).

influenced by the finite $g^{(2)}(0)$: following the standard procedure,[107] the true photon overlap (derived in detail in Chapter 2, Sec. 2.5) can be estimated to be $V \simeq (1 + 2g^{(2)}(0)) \cdot V_{\text{raw}} = 96.7\%$. This demonstrates that successively generated photons are highly coherent. Crucial however is the coherence of photons separated much further apart in time. The HOM visibility on interfering two photons separated by 1.5 μs in time is equally high (Fig 5.4c). Given that photons can be created each with a ns interval (Fig 5.4b), these experiments demonstrate that the device can produce a string consisting of thousands of pure coherent single photons, as presented in Fig 5.5. The dephasing time of the source is much larger than 1.5 μs.

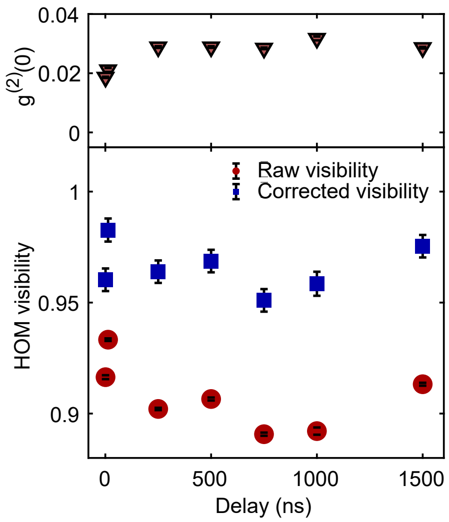

Figure 5.5: Single photon purity $g^{(2)}(0)$ and HOM visibility V versus delay in the interferometer. The error bars represent the 1-sigma random error.

5.6 Reproducibility and stability

The noise in the single photon flux is limited by shot-noise on time-scales of one hour (Fig 5.6a), increasing only slightly on time-scales of multiple hours (Fig 5.6b). The tunability of the microcavity enables us to bring multiple quantum dots one-by-one into resonance with the same microcavity mode. Six quantum dots were investigated in detail. All six have similar values of end-to-end efficiency (Fig 5.6c), coherence (Fig 5.6d), and purity (Fig 5.6e).

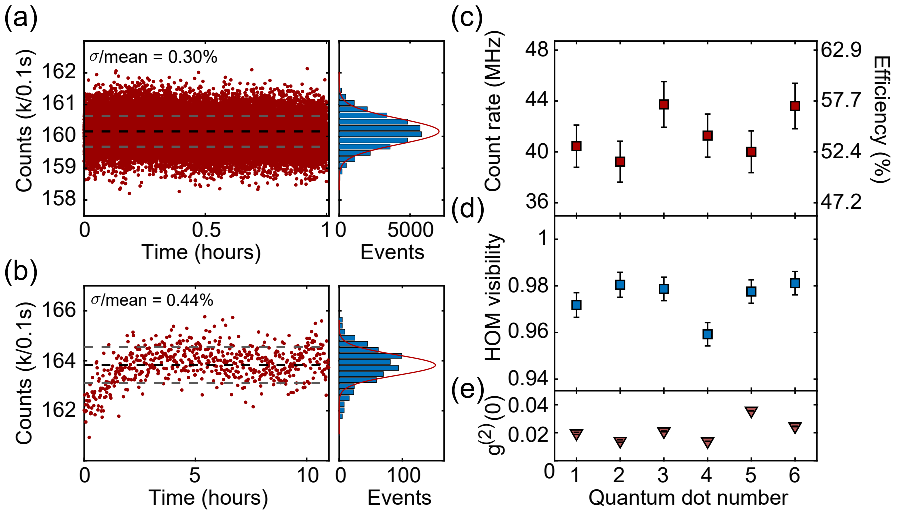

Figure 5.6: Stability and reproducibility of the single photon source. Single photon flux versus time and associated histogram recorded over one hour and over ten hours, (a) and (b), respectively, on QD1. Maximum count rates, HOM visibilities V_{HOM} and $g^2(0)$ values recorded on six separate quantum dots, (c), (d) and (e), respectively. The error bars represent the 1-sigma random error and do not include any systematic errors.

5.7 Conclusion and outlook

Σ is a product of factors, $\Sigma = \pi \cdot \beta_{\mathrm{H}} \cdot \kappa_{\mathrm{top}}/(\kappa+\gamma) \cdot \eta_{\mathrm{optics}}$, where π is the probability of producing a photon on excitation with a laser pulse; and η_{optics} represents the throughput of the entire optical system (from microcavity to the output of the final output fiber). β_{H} and $\kappa_{\mathrm{top}}/(\kappa+\gamma)$ are both determined in the experiment, $(86 \pm 2)\%$ and $(96 \pm 2)\%$ respectively. β_{H} matches theoretical expectations based on the optical dipole moment and the microcavity geometry. To determine π, we describe the excitation scheme, a detuned laser pulse followed by ring-down, and how it drives a two-level system, including an intensity-dependent phonon-related dephasing process[108] (Chapter 3). This calculation describes the Rabi oscillations (Fig 5.2c), enabling us to infer that at the peak signal, $\pi = (96.3 \pm 1.0)\%$. By building a replica of the optical setup and measuring its throughput (Chapter 2, Sec. 2.4), we estimate $\eta_{\mathrm{optics}} = (69.0 \pm 3.6)\%$. η_{optics} is determined by losses on coupling the single photons into the single-mode fiber, and by reflection losses at three surfaces (upper surface of top mirror, two fiber facets) which lacked an anti-reflection coating.

This analysis predicts $\Sigma = (54.9 \pm 8.6)\%$, equal within error to the measured values, and suggests that the main contribution to the overall losses lies in η_{optics}.

We point out that, first, based on our analysis, a single photon source with an end-to-end efficiency of more than 80% is within reach by eliminating the losses in the optical components. Second, the mode-splitting can be tuned to increase β_{H}. The mode-splitting can be controlled with the electro-optic effect[109] or by deliberately introducing birefringence to the top mirror.[110] Third, even better performance is conceivable by increasing the coupling via miniaturization of the top mirror and decreasing the bare decay rate via lateral structuring. Fourth, a more compact and stiffer device will be less susceptible to external noise and a monolithic device is conceivable by relying on strain tuning to bring a quantum dot into resonance with a fixed-frequency microcavity-mode.[111] Finally, in addition to the applications as a single photon source, a further broad area of application exploits the spin of the trapped hole. Implementing spin manipulation in the microcavity device, for instance by driving Raman transitions via lateral excitation,[112] may facilitate applications such as a single photon transistor,[113] the efficient and fast creation of spin-photon entangled pairs, and an efficient source of multi-photon cluster states.[114]

6

CAVITY MODE-SPLITTING TUNING USING THE PHOTOELASTIC EFFECT

Adapted from:

N. Tomm, A. R. Korsch, A. Javadi, D. Najer, R. Schott, S. R. Valentin, A. D. Wieck, A. Ludwig and R. J. Warburton,

"Tuning the mode splitting of a semiconductor microcavity with uniaxial stress",

Physical Review Applied **15**, 054061 (2021)

6.1 Summary

A splitting of the fundamental optical modes in micro/nano-cavities comprising semiconductor heterostructures is commonly observed. Given that this splitting plays an important role in the light-matter interaction and hence quantum technology applications, a method for controlling the mode-splitting is important. In this work we use an open microcavity composed of a "bottom" semiconductor distributed Bragg reflector (DBR) incorporating an n-i-p heterostructure, paired with a "top" curved dielectric DBR. We measure the mode-splitting as

a function of wavelength across the stopband. We demonstrate a reversible *in-situ* technique to tune the mode-splitting by applying uniaxial stress to the semiconductor DBR. The method exploits the photoelastic effect of the semiconductor materials. We achieve a maximum tuning of ∼11 GHz. The stress applied to the heterostructure is determined by observing the photoluminescence of quantum dots embedded in the sample, converting a spectral shift to a stress via deformation potentials. A thorough study of the mode-splitting and its tuning across the stopband leads to a quantitative understanding of the mechanism behind the results.

6.2 Introduction

Semiconductor quantum dots (QDs) coupled to optical microcavities represent an important platform to advance quantum information technologies. Semiconductor QD-cavity platforms, such as micropillars, photonic crystals and open microcavities, have been successfully employed to achieve highly efficient single-photon sources,[38,40] a coherent light-matter interaction,[54] generation of entangled photons,[115,116] and photon-photon switches.[117] Despite the history of successful cavity quantum-electrodynamics demonstrations in these systems, there are still partly unresolved technical questions that affect their performance. One such property is the almost ubiquitous observation that the fundamental cavity mode splits into two separate modes with linear, orthogonal polarizations. This lifting of the polarization degeneracy is desired and exploited in some cases, notably in efficient single-photon sources in order to avoid a 50% loss of signal in cross-polarized collection schemes.[38,40] In this scenario, a QD trion is excited via one cavity mode, and photons are preferentially emitted into the other cavity mode. In other cases however, polarization degenerate cavity modes are desirable. This is typically the case in experiments relying on circularly polarized excitation schemes,[118] for instance a single spin in a perpendicular magnetic field. Here, the linearly polarized cavity modes result in a reduced coupling to the quantum emitter.[119] It is not simple to control the bare mode-splitting precisely – it can depend on the local inbuilt strain in the material, and on fabrication imperfections. This suggests that a way of selectively tuning and controlling the mode-splitting is of great interest: the bare mode-splitting should be made large for a trion-based single photon source; the bare mode-splitting should ideally be eliminated for a single spin in an out-of-plane magnetic field. A tuning range in the range 10–50 GHz is sufficient in many cases.

6.3 Birefringence-induced cavity mode-splitting

The polarization splitting of a semiconductor microcavity's fundamental mode is the result of birefringence in the semiconductor between two orthogonal crystalline axes (which are themselves orthogonal to the optical axis). In zinc-blende type crystals there is *a priori* no intrinsic birefringence. Birefringence can be created however, often unintentionally, via two mechanisms. First, in heterostructures incorporating a diode or Schottky structure, the in-built electric field along the z direction (growth axis) breaks the inversion symmetry of the crystal and birefringence in the x-y plane arises via the linear electro optic effect.[120] Secondly, a uniaxial stress in the x-y plane, induced by microscopic imperfections in the heterostructure or post-growth processing, induces birefringence via the photoelastic effect.[121, 122] Contrarily, a biaxial stress does not result in observable birefringence on account of the symmetry of the zinc-blende crystal.

One can use the electro optic and photoelastic effects to reverse or enhance the birefringence in semiconductor cavities, as previously demonstrated in monolithic structures.[109, 123, 124] Also in dielectric cavities it was demonstrated that the birefringence can be engineered to obtain a large degree of control over the cavity's mode-splitting.[125, 126] Here, we present a way of tuning the mode-splitting of a hybrid dielectric-semiconductor open microcavity by making use of the photoelastic effect, i.e. the control of the birefringence upon application of uniaxial stress. A change in mode-splitting of $\sim 11\,\mathrm{GHz}$ is achieved. Moreover, application of uniaxial stress to an open microcavity results in control not only of the mode-splitting in the microcavity but also the absolute emission frequency of an embedded QD.[111, 127] In this microcavity embodiment, the full stress is experienced by the entire heterostructure. This is not necessarily the case for monolithic systems.

6.4 Experimental setup

We employ a miniturized Fabry-Pérot cavity.[38, 54, 62, 64] The bottom mirror is a 46-pair AlAs($\lambda/4$)/GaAs($\lambda/4$) semiconductor distributed Bragg reflector (DBR) grown on a [001] GaAs substrate, where λ refers to the wavelength of light in the material. The bottom mirror's stopband, shown in Fig. 6.1b, is centered at $\lambda = 918.7\,\mathrm{nm}$. The surface of the semiconductor heterostructure is passivated via an Al_2O_3 layer.[59] The top mirror is a 15-pair $SiO_2(\lambda/4)/Ta_2O_5(\lambda/4)$, Ta_2O_5-terminated, dielectric DBR where the layers are deposited onto a $\sim 600\,$nm-deep microcrater with a radius of curvature $\sim 15\,\mu$m in a silica substrate, and its stopband (Fig. 6.1a) is centered around $\lambda = 930.0\,$nm. The semiconductor heterostructure contains a layer of InAs QDs; the QDs themselves are embedded within an n-i-p heterostructure, allowing the QD charge to be controlled via a voltage (V_g) applied to the diode.[38, 54]

The sample is tightly glued onto a piezostack (PSt 150/7x7/7 cryo, Piezomechanik GmbH, Munich), as depicted in Fig. 6.2a. The $[1\bar{1}0]$ direction of the crystal aligns with the polarization axis of the pieozstack such that application of a voltage V_s to the piezostack induces a $[1\bar{1}0]$-stress in the semiconductor. The spring constant of the sample is small compared to that of the piezostack, $k_\mathrm{sample} \ll k_\mathrm{PZT}$, such that the extension of the piezo should be unaffected by the attached semiconductor. The piezo-sample assembly is mounted on a stack of xyz nanopositioners, which are used to to move it relative to the

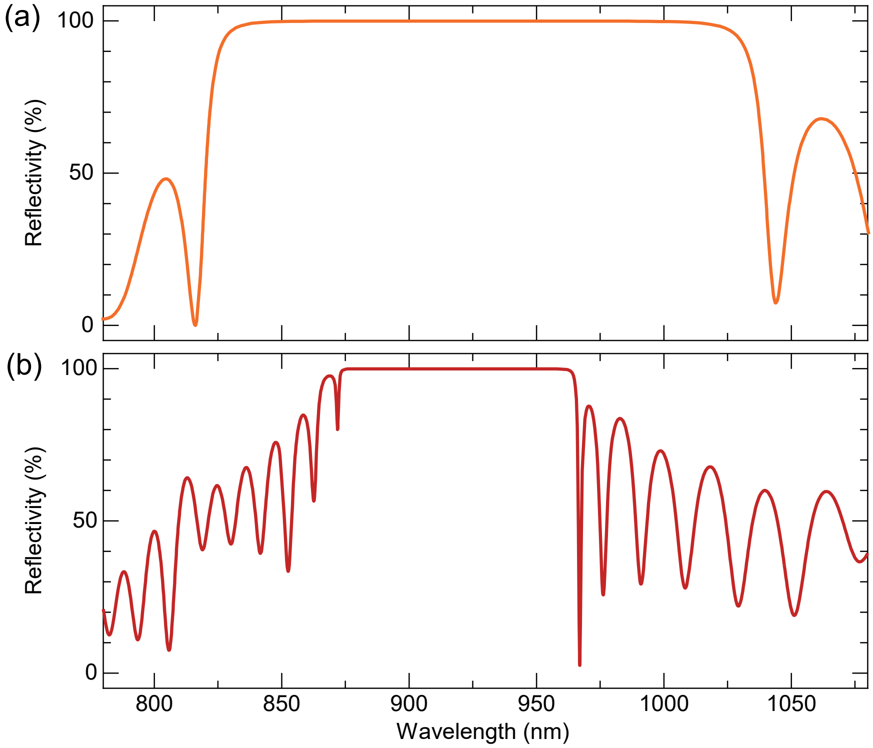

Figure 6.1: Reflectivity spectra modeling the (a) top and (b) bottom mirrors composing the microcavity. The respective stopbands are centered at $\lambda = 930.0\,$nm and $\lambda = 918.7\,$nm.

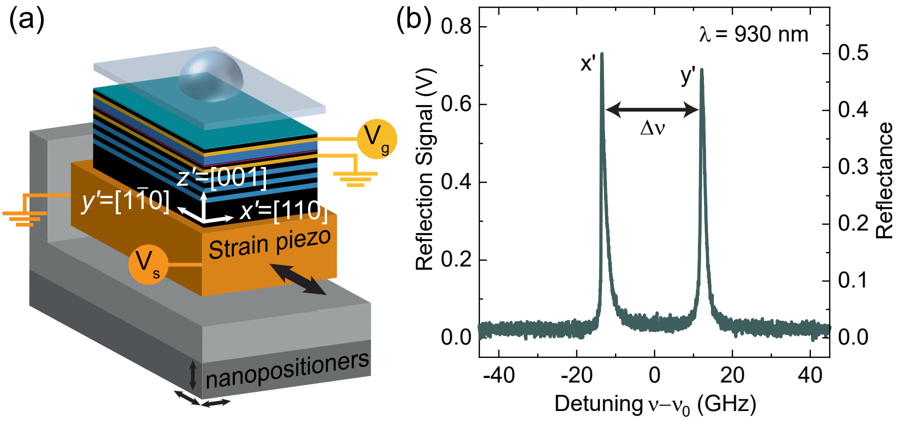

Figure 6.2: (a) Experimental setup depicting the microcavity composed of dielectric top mirror, and a semiconductor heterostructure, containing InAs QDs embedded in an n-i-p diode structure (applied voltage V_g), and the bottom mirror. The sample is glued onto a piezostack (applied voltage V_s), that stresses the sample along the y' crystalline direction. The sample is positioned both laterally and vertically relative to the top mirror via nanopositioners. (b) Dark-field reflectivity scan across a cavity resonance: the fundamental mode is split into two linearly and orthogonally polarized modes. The microcavity axes are aligned with respect to the sample's crystalline axes x' and y'. The x'-polarized (y'-polarized) mode is red (blue) detuned from the expected resonance ν_0. The orientation of the cavity modes is experimentally determined by aligning the polarization of the probing laser light to each cavity mode in turn, and by observing the alignment to the sample.

top mirror laterally, allowing different positions in the sample to be probed. The bottom mirror can also be moved vertically, changing the vacuum-gap separation between top and bottom mirrors, allowing a reflection spectrum of the microcavity to be recorded at fixed laser wavelength. We employ a cross-polarization confocal microscope,[66] where an added half-wave plate (HWP) allows the probe laser's polarization to be aligned with one or the other polarized cavity mode. The sample's orientation relative to the microscope axes is known; the cleaved edges of the semiconductor sample along the $x' = [110]$ and $y' = [1\bar{1}0]$ crystalline axes coincide with the microscope orientation to within few degrees. All experiments were carried out at a temperature $\mathrm{T} = 4\,\mathrm{K}$.

The fundamental cavity mode is probed by measuring the reflectivity of a narrowband laser in a polarization dark-field modus. Two closely spaced modes are observed as shown in Fig. 6.2b. When the HWP is set such that the probe laser's polarization is aligned to x' (y'), only the red (blue) detuned resonance is probed. When the HWP is set such that the probe laser is aligned at 45° to the x' and y' directions, both cavity modes can be seen (Fig. 6.2b). These are the characteristic features of a birefringence-induced mode-splitting. The fact that the axes of the cavity modes are consistently aligned with the cleaved edges of the sample implies that birefringence arises in the semiconductor heterostructure, and not in the top mirror. Should the origin of the birefringence lie in the top mirror, no link to the crystal axes of the semiconductor would be expected.

The mode-splitting is defined by $\Delta\nu = \nu_{x'} - \nu_{y'}$, where ν is the resonance frequency. It's important to note that the mode-splitting has a sign, negative in our case, meaning that the changes in refractive index along the x' and y' directions induce a red- and blue-shift, respectively, relative to the original resonance. The dynamic nature of the microcavity allows us to examine simultaneously the mode-splitting (Fig. 6.4a,b) and the $\mathcal{Q}$-factor across the microcavity's stopband (Fig. 6.3a,b). Both the bare mode-splitting and the $\mathcal{Q}$-factor have a dependence on wavelength with maximum amplitude centered around $\lambda = 918.7\,\mathrm{nm}$, at the stopband center of the bottom mirror.

6.5 Cavity characterization and modeling

We focus initially on the $\mathcal{Q}$-factors to demonstrate that we have a quantitative understanding of both the field confinement in the microcavity and the losses. We model the microcavity's stopband and $\mathcal{Q}$-factor dependence on wavelength (Fig. 6.3 dashed and solid lines) using a one-dimensional transfer-matrix simulation (Essential Macleod, Thin Film Center Inc.). In Fig. 6.3 the dashed lines depict the expected $\mathcal{Q}$-factor without any losses at the sample's surface. In practice, the measured $\mathcal{Q}$-factors are lower and this can be described very convincingly simply by including the effects of scattering at the Al_2O_3-vacuum interface.[59] The surface roughness was determined by comparing the experimental results and the theoretical model. We find that the maximum $\mathcal{Q}$-factor in this experiment depends on the exact lateral position, suggesting that the surface roughness changes across the sample.[59] A full wavelength dependence was acquired at two positions on the sample. A root-mean-square (rms) surface roughness of $\sigma = 1.60\,\mathrm{nm}$ ($\sigma = 0.65\,\mathrm{nm}$) at position 1 (position 2) provide a very good description of the wavelength dependence of the $\mathcal{Q}$-factor. These surface roughnesses are consistent with characterization of the surface at room temperature with atomic force microscopy.[59] The residual small discrepancy between experimental and modeled curves probably arises from an imperfect knowledge of the exact layer thicknesses in the DBRs.

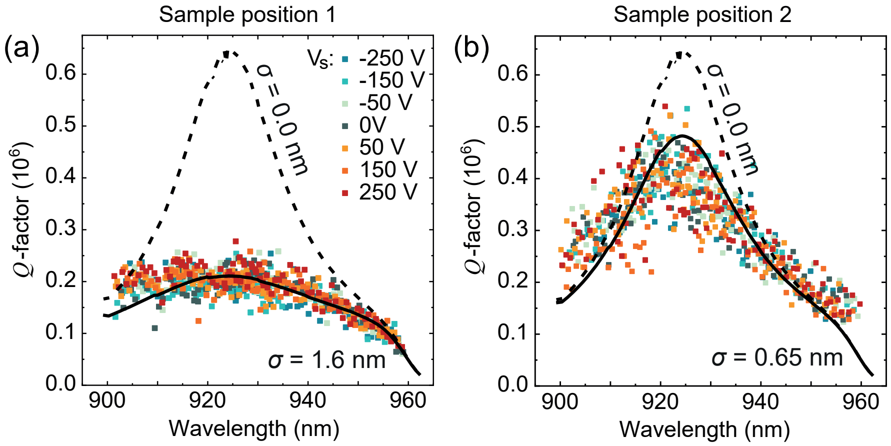

Figure 6.3: Q-factor as a function of probe wavelength and voltage V_s applied to the strain-tuning piezo at (a) position 1, where the root-mean-square surface roughness is $\sigma = 1.60\,\text{nm}$, and (b) position 2, where $\sigma = 0.65\,\text{nm}$. The solid (dashed) lines are the modeled Q-factor dispersion curves for this microcavity in the case with (without) surface scattering.

6.6 Tuning the mode-splitting with uniaxial stress

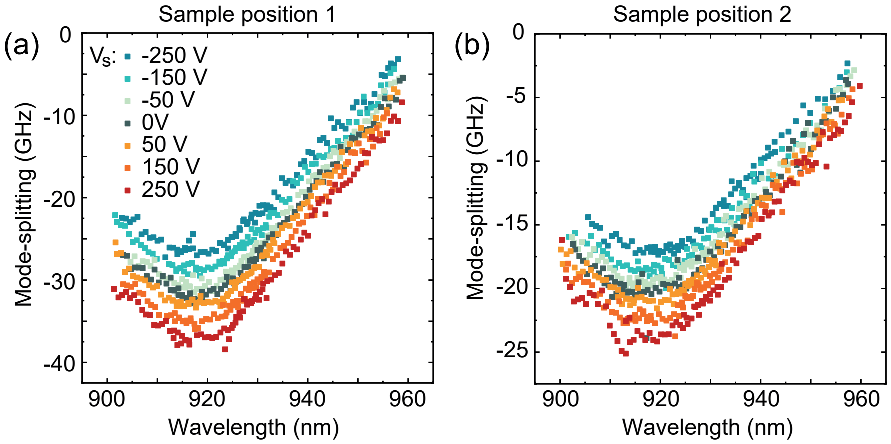

Figure 6.4: Cavity mode-splitting $\Delta\nu = \nu_{x'} - \nu_{y'}$ as a function of probe wavelength and voltage V_s applied to the piezo at (a) position 1, and (c) position 2.

We turn now to the behaviour on applying a uniaxial stress. We focus on position 1. Upon application of a voltage up to $V_\mathrm{s} = \pm 250$ V, the piezostack expands and contracts, thereby stressing the sample uniaxially along the y' direction. The mode-splitting responds to the applied stress. A maximum mode-splitting tuning of approximately 11 GHz (45 μeV) is achieved at the exact wavelength where $|\nu_{x'} - \nu_{y'}|$ is the largest, as can be observed in Fig. 6.4a. The tuning leaves the $\mathcal{Q}$-factor unaltered (Fig. 6.3b) indicating that the applied stress has no effect on the loss mechanisms in these high-$\mathcal{Q}$-factor cavities. The mode-splitting $\Delta\nu$ is a linear function of V_s (Fig. 6.7b); the response $\Delta\nu/\Delta V_\mathrm{s}$ is slightly smaller in magnitude at the edges of the bottom mirror's stopband with respect to its stopband center (Fig. 6.7d).

6.7 Photoelastic effect

We now attempt to describe quantitatively the stress-induced changes in the birefringence of the heterostructure.

The refractive index n of a crystal can be described by the indicatrix,[128] an ellipsoid in which the principal axes represent the components of the dielectric tensor,

$$\overline{\overline{B_{ij}}} = \varepsilon_0 \frac{\partial E_i}{\partial D_j} = \left(\frac{1}{n^2}\right), \tag{6.1}$$

where ε_0 is the vacuum's electric permittivity, E_i is the electric field component along direction i and D_j is the electric displacement field along j. An applied stress deforms the indicatrix components $\Delta\overline{\overline{B_{ij}}}$ via the operation

$$\Delta\overline{\overline{B_{ij}}} = \overline{\overline{\overline{\overline{q_{ijkl}}}}} \cdot \overline{\overline{\sigma_{kl}}}. \tag{6.2}$$

Here, $\overline{\overline{\overline{\overline{q_{ijkl}}}}}$ $(i,j,k,l = 1,2,3)$ is the fourth-rank piezo-birefringent tensor; the stress $\overline{\overline{\sigma_{kl}}}$ $(k,l = 1,2,3)$ is a second-rank tensor. From Eq. 6.1 and Eq. 6.2, it follows that the change in refractive index $\Delta\overline{\overline{n_{ij}}} = \overline{\overline{n_{ij}}} - n_0$ (where n_0 is the bare refractive index of the isotropic material) reads

$$\Delta\overline{\overline{n_{ij}}} = -\frac{\Delta\overline{\overline{B_{ij}}}}{2} \cdot n_0^3. \tag{6.3}$$

For zinc-blende type (cubic) crystals, symmetry simplifies the photoelastic tensor such that only three independent coefficients remain,[122] namely q_{1111}, q_{1122} and q_{2323}. A compressed notation can be adopted: 11 → 1, 22 → 2, 33 → 3, 23 → 4, 13 → 5, 12 → 6. In this way, the rank of the tensors is reduced and the expression in Eq. 6.2 becomes $\Delta\overline{B_m} = \overline{\overline{q_{mn}}} \cdot \overline{\sigma_n}$ $(m, n = 1, 2, 3, 4, 5, 6)$. In extended form,

$$\begin{bmatrix} \Delta B_1 \\ \Delta B_2 \\ \Delta B_3 \\ \Delta B_4 \\ \Delta B_5 \\ \Delta B_6 \end{bmatrix} = \begin{bmatrix} q_{11} & q_{12} & q_{12} & 0 & 0 & 0 \\ q_{12} & q_{11} & q_{12} & 0 & 0 & 0 \\ q_{12} & q_{12} & q_{11} & 0 & 0 & 0 \\ 0 & 0 & 0 & q_{44} & 0 & 0 \\ 0 & 0 & 0 & 0 & q_{44} & 0 \\ 0 & 0 & 0 & 0 & 0 & q_{44} \end{bmatrix} \begin{bmatrix} \sigma_1 \\ \sigma_2 \\ \sigma_3 \\ \sigma_4 \\ \sigma_5 \\ \sigma_6 \end{bmatrix} . \tag{6.4}$$

We now apply these general results to our problem. In the experiment, both the stress and the birefringence are applied/probed in the $(x'$,y',$z')$ system of coordinates. Therefore, a rotation in the frame of reference by $\pi/4$ around $z = z'$ is applied. We treat the canonical case of a stress applied along the x' direction.

In the $(x'$,y',$z')$ basis, the simplified stress tensor for a uniaxial stress along x' is self-evidently $\overline{\sigma'} = [1\,0\,0\,0\,0\,0]^{\mathsf{T}}$. We start by calculating $\overline{\sigma}$ in the usual basis $(x$,y,$z)$ from $\overline{\sigma'}$. The general rotation matrix for an arbitrary angle θ and with $\theta = \pi/4$ is

$$\overline{\overline{R}} = \begin{bmatrix} \cos\theta & \sin\theta & 0 \\ -\sin\theta & \cos\theta & 0 \\ 0 & 0 & 1 \end{bmatrix} \overset{\theta=\pi/4}{=} \begin{bmatrix} \frac{1}{\sqrt{2}} & \frac{1}{\sqrt{2}} & 0 \\ \frac{-1}{\sqrt{2}} & \frac{1}{\sqrt{2}} & 0 \\ 0 & 0 & 1 \end{bmatrix} . \tag{6.5}$$

In the $(x$,y,$z)$ basis, the stress is calculated via $\overline{\sigma} = \overline{\overline{R}}^{\mathsf{T}} \cdot \overline{\sigma'} \cdot \overline{\overline{R}}$ to be

$$\overline{\sigma_m} = \frac{\sigma}{2} \begin{bmatrix} 1 \\ 1 \\ 0 \\ 0 \\ 0 \\ 1 \end{bmatrix} , \tag{6.6}$$

where σ is the magnitude of the stress applied. We can now apply Eq. 6.4 to determine $\Delta\overline{B}$:

$$\Delta\overline{B_m} = \frac{\sigma}{2} \begin{bmatrix} q_{11} + q_{12} \\ q_{11} + q_{12} \\ 2\,q_{12} \\ 0 \\ 0 \\ q_{44} \end{bmatrix} . \tag{6.7}$$

Since, however, we want to probe the birefringence in the $(x'$,y',$z')$ basis, we apply the inverse rotation transformation ($\theta = \pi/4$) to determine $\Delta\overline{B'}$:

$$\begin{bmatrix} \Delta B'_1 \\ \Delta B'_2 \\ \Delta B'_3 \\ \Delta B'_4 \\ \Delta B'_5 \\ \Delta B'_6 \end{bmatrix} = \begin{bmatrix} \Delta B'_{x'x'} \\ \Delta B'_{y'y'} \\ \Delta B'_{z'z'} \\ \Delta B'_{y'z'} \\ \Delta B'_{x'z'} \\ \Delta B'_{x'y'} \end{bmatrix} = \frac{\sigma}{2} \begin{bmatrix} q_{11} + q_{12} + q_{44} \\ q_{11} + q_{12} - q_{44} \\ 2\,q_{12} \\ 0 \\ 0 \\ 0 \end{bmatrix}, \tag{6.8}$$

from which follows (using Eq. 6.3) a change in refractive index

$$\begin{bmatrix} \Delta n_{x'x'} \\ \Delta n_{y'y'} \\ \Delta n_{z'z'} \\ \Delta n_{y'z'} \\ \Delta n_{x'z'} \\ \Delta n_{x'y'} \end{bmatrix} = \begin{bmatrix} n_{x'x'} - n_0 \\ n_{y'y'} - n_0 \\ n_{z'z'} - n_0 \\ n_{y'z'} - n_0 \\ n_{x'z'} - n_0 \\ n_{x'y'} - n_0 \end{bmatrix} = -\frac{\sigma}{4} n_0^3 \begin{bmatrix} q_{11} + q_{12} + q_{44} \\ q_{11} + q_{12} - q_{44} \\ 2\,q_{12} \\ 0 \\ 0 \\ 0 \end{bmatrix}. \tag{6.9}$$

We are primarily interested in the birefringence between axes (x',y'), namely $\Delta n = \Delta n_{x'x'} - \Delta n_{y'y'} = n_{x'x'} - n_{y'y'}$. In the experiment, the stress is applied along y'. In this case, $\overline{\sigma'} = [0\,1\,0\,0\,0\,0]^\intercal$, and $\Delta n = n_{x'x'} - n_{y'y'} = \frac{n_0^3}{2} \cdot q_{44} \cdot \sigma$, where σ in this case has the inverse sign as in the case of stress applied along x', from which we obtain $\frac{\Delta n}{n_0} = -\frac{n_0^2}{2} \cdot q_{44} \cdot \sigma$, Eq. 6.14 in the following.

6.8 Piezo-optical coefficients q_{44} at T = 4 K

Data on the piezo-optical coefficient q_{44} of $\mathrm{Al}_x\mathrm{Ga}_{1-x}\mathrm{As}$ alloys can be found for measurements[129, 130] at $T = 298\,\mathrm{K}$, and for GaAs at $T = 77\,\mathrm{K}$.[129] However, this data is not available at $T = 4\,\mathrm{K}$ to the best of our knowledge. The dispersion of these coefficients is linked to the bandgap of the particular material. In particular, q_{44} shows a resonance behaviour at the bandgap itself. As the bandgap of these materials shifts with temperature, the q_{44} coefficients are temperature dependent. It is therefore necessary to estimate the q_{44} values at $T = 4\,\mathrm{K}$. We elaborate here the procedure.

Adachi[130] provides data – we extract the data from the plots with Webplotdigitizer[131] – on $\mathrm{Al}_x\mathrm{Ga}_{1-x}\mathrm{As}$ alloys, of particular relevance here the dispersion curve of the elasto optic coefficients p_{44}, related to the piezo-birefringent coefficients via $q_{44} = p_{44} \cdot S_{44}$. The room-temperature bandgap energies of the alloys of interest are also extracted ($E_{\mathrm{gap}}(\mathrm{GaAs}) = 1.424\,\mathrm{eV}$, $E_{\mathrm{gap}}(\mathrm{Al}_{.33}\mathrm{Ga}_{.67}\mathrm{As}) = 1.8355\,\mathrm{eV}$,

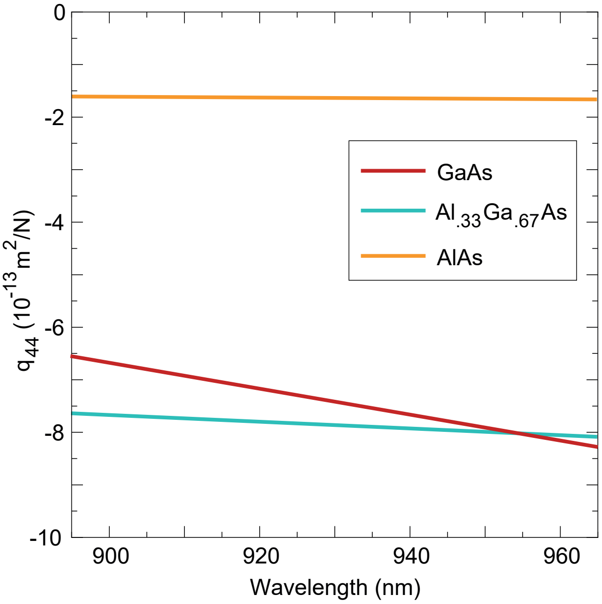

Figure 6.5: Piezobirefringent coefficients q_{44} at $T = 4\,\mathrm{K}$ for GaAs, Al$_{.33}$Ga$_{.67}$As and AlAs, estimated from their room temperature values by shifting the wavelength rigidly by an amount equal to the shift in bandgap with temperature.

E_{gap}(AlAs)$= 2.168\,\mathrm{eV}$). The optical properties of semiconductor crystals, such as the refractive index, are linked to the bandgap energy of the material.[132] The temperature dependence of the GaAs bandgap can be described via $E_{\mathrm{gap}}(T) = E_{\mathrm{gap}}(0) - 5.405 \cdot 10^{-4} T^2 / (T + 204)$ (with $E_{\mathrm{gap}}(T)$ in eV, T in K).[133] This equation was demonstrated to be valid also for Al$_x$Ga$_{1-x}$As alloys.[134]

From the room-temperature (298 K) bandgap energies, we can estimate the low-temperature bandgap energies of our materials, namely E_{gap}(GaAs)$= 1.519\,\mathrm{eV}$, E_{gap}(Al$_{.33}$Ga$_{.67}$As)$= 1.931\,\mathrm{eV}$, E_{gap}(AlAs)$= 2.263\,\mathrm{eV}$, representing a shift in bandgap energy of 95 meV for these materials. These shifts translate into a shift in wavelength of $\Delta\lambda = -54.45\,\mathrm{nm}$, $\Delta\lambda = -33.22\,\mathrm{nm}$ and $\Delta\lambda = -24.01\,\mathrm{nm}$, respectively. We now estimate q_{44} at 4 K for a particular wavelength λ by rigidly shifting the curve of q_{44} versus λ at 298 K by $\Delta\lambda$. We confirm that this method functions well by comparing translated $T = 298\,\mathrm{K}$ data[130] for q_{44} to $T = 77\,\mathrm{K}$ data[129] and verifying an overlap.

Finally, we comment that the dispersion of q_{44} of the semiconductor materials is rather small in the spectral band of interest, as exemplified in Fig. 6.5, such that we use their mean values in the model – we treat the small dispersion as a measure of the uncertainty in the parameters.

6.9 Bandgap shift with uniaxial stress

The photoluminescence spectra of excitonic transitions also shift as a result of uniaxial stress. Upon application of the uniaxial stress used to tune the birefringence of the semiconductor DBR, the embedded QDs also experience the exact same stress. Therefore, the spectral shift of the QD's emission can be used as a gauge to determine the amount of stress in the heterostructure.

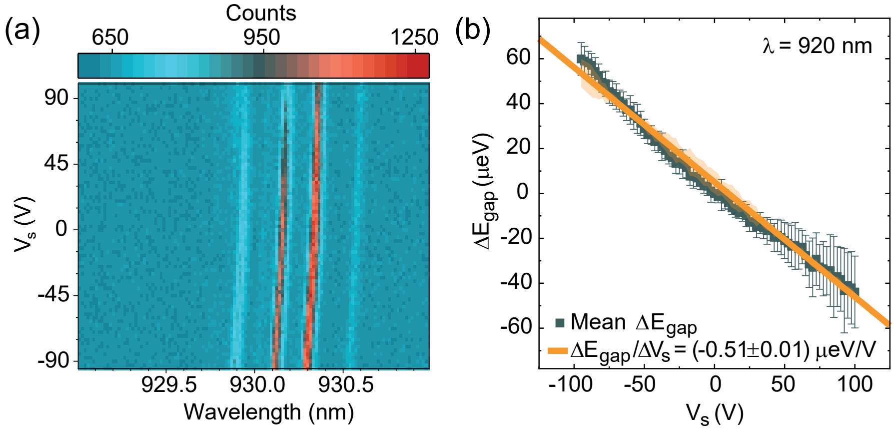

Figure 6.6: (a) Shift of the photoluminescence signal of a QD in the sample as a function of applied uniaxial stress. (b) Mean shift in bandgap energy as a function of voltage applied to the piezostack (V_s), as measured on 20 different excitonic lines in 10 QDs. A linear fit gives $\delta E_{\mathrm{gap}}/\delta V_{\mathrm{s}} = (-0.51 \pm 0.01)\mu\mathrm{eV/V}$.

In order to calculate the excitonic emission shift as a result of uniaxial stress (along x') we assume that the shift is determined solely by the shift in the bandgap of the host material, GaAs. We start with the Bir-Pikur expression[135] for the bandgap shift ΔE_{gap} with applied strain $\overline{\overline{\varepsilon_{ij}}}$ in the usual basis (x,y,z). The quantum dots themselves define the quantization axis, i.e. z = [001]. Assuming further that the valence state is of pure heavy-hole character, on account of the large heavy-hole–light-hole splitting,

$$\Delta E_{\mathrm{gap}} = a_\Gamma \,\mathrm{Tr}\,(\varepsilon_{ij}) + \frac{b}{2}(2 \cdot \varepsilon_{zz} - \varepsilon_{xx} - \varepsilon_{yy}), \tag{6.10}$$

where a_Γ and b are the deformation potential coefficients, and $\mathrm{Tr}(\varepsilon_{ij})$ is the trace of the strain tensor $\overline{\overline{\varepsilon_{ij}}}$.

We apply a stress, and thereby induce a strain. We use the strain–stress relation

$\overline{\varepsilon_m} = \overline{\overline{S_{mn}}} \cdot \overline{\sigma_n}$, where $\overline{\overline{S_{mn}}}$ is the compliance tensor, abbreviated in a similar way to Eq. 6.4 on account of symmetry. We now know also the expression for a uniaxial stress along x' in the usual basis (Eq. 6.6). The strain–stress relation reads

$$\begin{aligned} \begin{bmatrix} \varepsilon_{xx} \\ \varepsilon_{yy} \\ \varepsilon_{zz} \\ \varepsilon_{yz} \\ \varepsilon_{xz} \\ \varepsilon_{xy} \end{bmatrix} &= \frac{\sigma}{2} \begin{bmatrix} S_{11} & S_{12} & S_{12} & 0 & 0 & 0 \\ S_{12} & S_{11} & S_{12} & 0 & 0 & 0 \\ S_{12} & S_{12} & S_{11} & 0 & 0 & 0 \\ 0 & 0 & 0 & S_{44} & 0 & 0 \\ 0 & 0 & 0 & 0 & S_{44} & 0 \\ 0 & 0 & 0 & 0 & 0 & S_{44} \end{bmatrix} \begin{bmatrix} 1 \\ 1 \\ 0 \\ 0 \\ 0 \\ 1 \end{bmatrix} \\ &= \frac{\sigma}{2} \begin{bmatrix} S_{11} + S_{12} \\ S_{11} + S_{12} \\ 2\,S_{12} \\ 0 \\ 0 \\ S_{44} \end{bmatrix} . \end{aligned} \tag{6.11}$$

Now, $\mathrm{Tr}(\varepsilon_m) = \varepsilon_{xx} + \varepsilon_{yy} + \varepsilon_{zz} = (S_{11} + 2\,S_{12})\,\sigma$ and $2\,\varepsilon_{zz} - \varepsilon_{xx} - \varepsilon_{yy} = (S_{12} - S_{11})\,\sigma$. Transforming[128] $\overline{\overline{S_{mn}}}$ to the stiffness tensor $\overline{\overline{C_{mn}}}$, Eq. 6.10 gives us the bandgap shift as a function of a stress along [110]:

$$\delta E_{\mathrm{gap}}/\delta\sigma = \left(\frac{a_\Gamma}{C_{11} + 2\,C_{12}} - \frac{b}{2}\,\frac{1}{C_{11} - C_{12}} \right) . \tag{6.12}$$

We use the following numerical values for GaAs from literature[136–138] for the computation: $a_\Gamma = -8.33\,\mathrm{eV}$, $b = -2.00\,\mathrm{eV}$, $C_{11} = 122.3\,\mathrm{GPa}$ and $C_{12} = 57.1\,\mathrm{GPa}$. We finally arrive at $\delta E_{\mathrm{gap}}/\delta\sigma = -22.2\,\mu\mathrm{eV/MPa}$.

6.10 Quantifying the stress-induced birefringence

We now have all the ingredients to describe quantitatively the stress-induced change in mode-splitting. A crucial step is to determine the exact uniaxial stress applied. The extension per Volt of the piezostack depends strongly on temperature and unfortunately we do not know its exact value at T=4 K. We do not have an external stress gauge in the experiment. Instead, we determine the applied stress by measuring the frequency-shift of the photoluminescence from the QDs embedded in the sample.[111] This has the advantage of determining the stress experienced by the heterostructure itself, exactly the stress which induces the birefringence. We determine the mean bandgap shift as a function of applied voltage V_s by observing the photoluminescence signal of 20 different excitonic lines in 10 QDs in the sample, as depicted in Fig. 6.6a, and find $\Delta E_\mathrm{gap}/\Delta V_\mathrm{s} = (-0.51 \pm 0.01)\,\mu\mathrm{eV/V}$ equivalently $(-0.123 \pm 0.002)\,\mathrm{GHz/V}$ (Fig 6.6b), a value comparable to a previously achieved[111] tuning of $-0.82\,\mu\mathrm{eV/V}$. The dominant effect of an applied differential uniaxial stress $\delta\sigma$ on the emission frequency of the QDs is to induce a change in the bandgap δE_gap of the host semiconductor GaAs,[139–141] described by $\delta E_\mathrm{gap}/\delta\sigma$. The influence of uniaxial stress on the bandgap can be derived (Sec. 6.9) from the material's deformation potentials to be $\delta E_\mathrm{gap}/\delta\sigma = -22.2\ \mu\mathrm{eV/MPa}$, under the assumption that the valence state is pure heavy-hole. Finally, from

$$\Delta\sigma/\Delta V_\mathrm{s} = \frac{\delta E_\mathrm{gap}/\delta V_\mathrm{s}}{\delta E_\mathrm{gap}/\delta\sigma} \tag{6.13}$$

we infer $\frac{\Delta\sigma}{\Delta V_\mathrm{s}} = (22.97 \pm 0.45)\,\mathrm{kPa/V}$, from which we are able to deduce the amount of stress applied to the sample $\sigma = \frac{\Delta\sigma}{\Delta V_\mathrm{s}}\,V_\mathrm{s}$.

The next step is to calculate the birefringence in each layer in the heterostructure. Stress-induced transformations to the dielectric function of a crystal are quantified by the so-called piezobirefringent tensor[122, 128, 141, 142] q_{ijkl}. Due to the symmetry of zinc-blende crystals,[122, 128] and our system of coordinates $x' = [110]$, $y' = [1\bar{1}0]$, $z' = z = [001]$, the induced birefringence $\Delta n/n_0 = (n_{x'} - n_{y'})\,/n_0$ on stressing a semiconductor along x' by an amount σ is given by

$$\frac{\Delta n}{n_0} = -\frac{n_0^2}{2} \cdot q_{44} \cdot \sigma, \tag{6.14}$$

where n_0 is the bare refractive index of the particular material, and q_{44} is a material parameter, $q_{44} = p_{44} \cdot S_{44}$, where p_{44} is an element of the photoelastic tensor and S_{44} an element of the compliance tensor. See Sec. 6.7 for complete derivation.

Given that the sample is composed of layers of three different semiconductor materials (GaAs, $\mathrm{Al_{.33}Ga_{.67}As}$ and AlAs), the influence of uniaxial stress in each layer must be considered. The coefficients q_{44} for GaAs, $\mathrm{Al_{.33}Ga_{.67}As}$ and AlAs at low temperature T = 4 K are estimated (Sec. 6.8) from literature room-temperature values[130] and found to be respectively $q_{44} = (-7.4 \pm 1.2) \cdot 10^{-13}\,\mathrm{m^2/N}$, $q_{44} = (-7.9 \pm 0.3) \cdot 10^{-13}\,\mathrm{m^2/N}$ and $q_{44} = (-1.64 \pm 0.02) \cdot 10^{-13}\,\mathrm{m^2/N}$.

Finally, we determine the mode-splitting by calculating the exact mode frequency for each polarization separately, including the subtle changes to the refractive indexes in the one-dimensional transfer-matrix simulation. Specifically, we use Eq. 6.14 to calculate the induced birefringence Δn in each layer

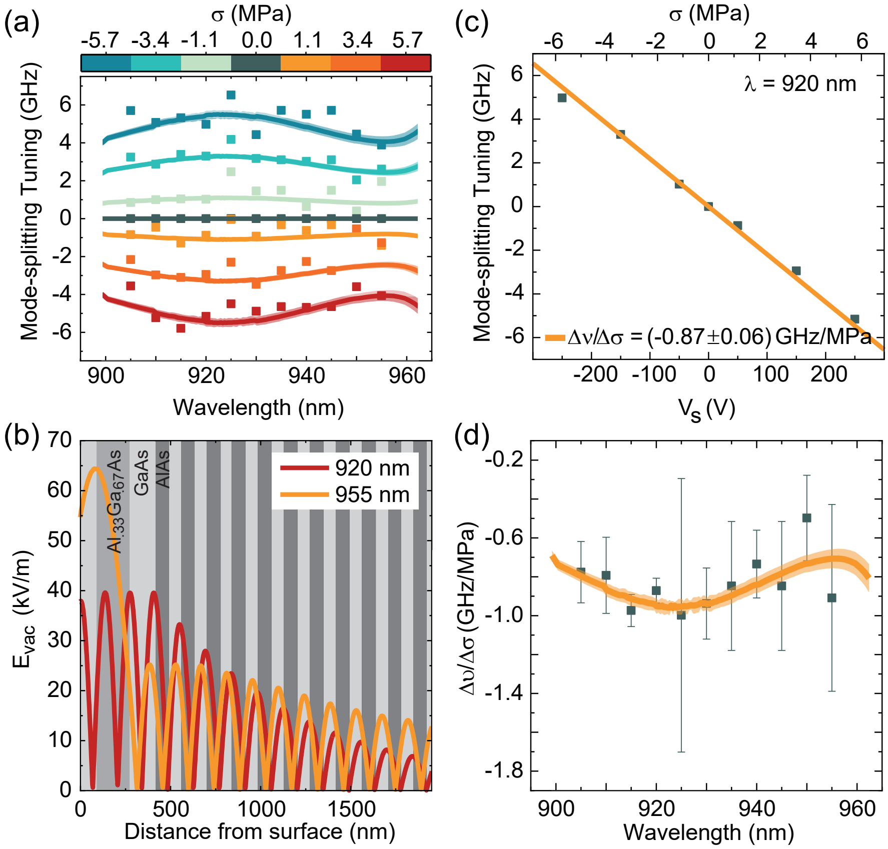

Figure 6.7: (a) Change in mode-splitting as a function of wavelength and applied uniaxial stress σ from experimental data (dots) and theoretical model (solid lines). The model involves adjusting the refractive index of each layer in the heterostructure using Eqs. 6.13 and 6.14 and then calculating the exact resonance frequency in a one-dimensional transfer matrix simulation. The error bars in the model arise from uncertainties in the coefficients q_{44} and in the calculation of $\delta E_{\text{gap}}/\delta V_{\text{s}}$. (b) Vacuum electric field distribution along the first few hundred nanometers below the sample's surface at wavelengths of 920 nm and 955 nm, indicating the dispersive influence of each layer's birefringence on the mode-splitting. (c) The mode-splitting tuning at $\lambda = 920$ nm as a function of applied stress voltage V_{s} (and respective stress σ). A linear fit determines the tuning rate $\Delta\nu/\Delta\sigma = (-0.87 \pm 0.06)$ GHz/MPa at this wavelength. (d) The tuning rate $\Delta\nu/\Delta\sigma$ as a function of wavelength across the the entire stopband: experiment (black symbols); model (orange line).

of the heterostructure upon application of uniaxial stress σ, which is itself calculated with Eq. 6.13. For $V_{\text{s}} = 250$ V, $\sigma = 5.74$ MPa, the induced relative birefringence $\Delta n/n_0$ is as small as 26 ppm in GaAs (25 ppm in $\text{Al}_{.33}\text{Ga}_{.67}\text{As}$, 4 ppm in AlAs). The stress-tuning of the mode-splitting is shown in Fig. 6.7a (solid lines) for each applied stress voltage V_s as a function of wavelength (spanning the stopband). The results can be directly compared to the experimental results (symbols). Evidently from Fig. 6.7a, the amount of tuning itself presents a dispersion, i.e. it depends on wavelength. The calculation captures this detail precisely and explains it: subtle shifts in the standing wave in the microcavity change the net birefringence as each layer of the heterostructure does not contribute equally. Figure 6.7b illustrates this point by showing the vacuum electric field as a function of distance from the sample's surface at a wavelength close to the bottom mirror's stopband center, at 920 nm, and at a wavelength far away, at 955 nm. As a consequence, the mode-splitting tunes linearly with stress, as depicted in Fig. 6.7c for $\lambda = 920\,\text{nm}$, but with different slopes $\Delta\nu/\Delta\sigma$ across the stopband (Fig. 6.7d). Across the entire spectral range examined here, experimental data (points) and model (solid lines) present excellent agreement.

6.11 Conclusions and outlook

Our method proves to be an effective way of controlling the intrinsic polarization splitting of an open semiconductor microcavity by up to ±5.5 GHz. The mode-splitting can be tuned across the entire stopband in a predictable, reversible manner. The present microcavity has a rather large intrinsic mode-splitting. Nevertheless, the tuning capability allows us to achieve near-degeneracy of the cavity modes at the high-wavelength end of the stopband. For a microcavity with a lower intrinsic mode-splitting, it should be possible to eliminate the mode-splitting. Of relevance here is the fact that the intrinsic mode-splitting and the applied stress are aligned along the same axes. The applied stress induces a small birefringence, on the order of a few ppm, and does not influence the microcavity's $\mathcal{Q}$-factor. The slight emission shift of the QDs embedded in the heterostructure can be compensated for in the present setup simply by exploiting the spectral tunability of the microcavity: a resonance with the cavity mode is easily maintained.

Naturally, it is desirable to achieve a higher degree of mode-splitting tunability: perfect degeneracy of the polarized modes would be desirable for any experiments relying on circularly polarized transitions;[118, 119] a further increase in the mode-splitting until the two cavity modes overlap only weakly in frequency is sought in experiments which hinge on the vacuum field of just one of the cavity modes.[38, 40] An optimized architecture of the sample holder could increase the tuning rate[127] by a factor of 20. The incorporation of a back-gate would allow an electric field to be applied across the bottom mirror, thereby making use of the electrooptic effect.[109] Employing these two methods simultaneously would grant an even higher degree of control of the birefringence. Additionally, inspired by liquid-crystal tuning of microcavities at room temperature,[126] it might be possible to include a thin layer of a highly piezobirefringent layer in the present device. As a final comment, we note that while a quantitative understanding of the origin of the intrinsic mode-splitting has not yet been attained, the mode-splitting dispersion curve can be used as a diagnostic tool as it indicates in which layers of the heterostructure birefringence is strong.

7

CONCLUSIONS AND OUTLOOK

This thesis reports the technological steps to achieve a world-record efficiency in deterministic single photon creation. We pursue the route of exploiting atom-like structures, InAs quantum dots (QDs), that naturally emit single photons by the process of spontaneous emission. The QDs are embedded in a semiconductor heterostructure, within a p-i-n type diode, which ensures low-noise operation and fine-tuning of the transition energy in the QD. This kind of gated structure is not straight-forward to implement in combination with photonic nanostructures, necessary to enhance the rate of spontaneous emission. We break with the established paradigms pursued in other devices, and use an open tunable Fabry-Perot type microcavity. The “bottom” mirror of the Fabry-Perot cavity is a semiconductor distributed Bragg reflector (DBR), on top of which the QDs are grown. The “top” mirror is a silica chip onto which micrometer-sized “craters” are created, and coated with a dielectric DBR. Such an open system facilitates the implementation of gated QDs and gives all spacial degrees of freedom to couple resonantly, with the same cavity, many QDs in the sample.

We guide the reader step-by-step on the design, fabrication and characterization of the sample and the cavity. A cavity with very well characterized optical losses is key to achieving high quantum efficiency in the single photon creation process. Passivating the surface of the semiconductor heterostructure is shown to mitigate surface-related optical losses. The fundamental cavity mode is split into two orthogonal linear polarizations. This splitting in frequency is exploited in combination with a circular optical transition of the QD to avoid losing half of the produced single photons on a cross-polarization confocal microscope. The classical losses in the optical setup and the efficiency of the detectors also had to be thoroughly characterized in order to estimate correctly the end-to-end efficiency of the envisioned single photon source. The probability of bringing the QD into an excited state with a short pulse of light, usually assumed to be unity, is demonstrated to be influenced both by the filtering operation performed by the cavity and by dephasing provoked by phonons.

The created single photon source presents a (to date) record end-to-end efficiency, able to create a photon every 50 ps at the output of the entire system with a 57% probability upon a triggering signal. This represents an improvement of 2.3 times over the previous state-of-the-art.[73] Furthermore, the source creates single photons with a purity of about 98% reaching the theoretical limit,[143] given the re-excitation and re-emission process that can happen within the finite pulse length of the excitation laser. Also, the successively produced single photons present a very high degree of indistinguishability, deduced from the Hong-Ou-Mandel visibility of approximately 98%, limited only by phonon-induced decoherence.[43] The demonstration of high indistinguishability values maintained for photons emitted more than 1.5 μs apart is novel for semiconductor QD based single photon sources, and we attribute it to the low-noise environment and charge control resulting from the gated p-i-n diode structure in which the QDs are embedded. The coherence of the system is clearly much longer than that. If a single photon is created every ns, such long coherence times allow for the creation of streams of thousands of indistinguishable photons, an essential characteristic for quantum information processing relying on demultiplexing from a single source of photons.

In the saga to create a high-efficiency single photon source, every photon counts. In resonant excitation schemes, the way to separate the emitted single photons from background laser light relies on employing a cross-polarization microscope. A key development in this work was to exploit the rather large intrinsic birefringence in the semiconductor sample to avoid this losing 50% of the polarized photons at the microscope's polarizing beam-splitter. The birefringence leads to the splitting in frequency of the fundamental cavity mode into two orthogonal linear polarizations. The laser light is V-polarized, the created single photons are collected via the the H-polarized cavity mode, detuned from the laser. For this scheme, large mode-splittings are desired. We demonstrate a technique to tune the cavity's mode-splitting by up to 11 GHz upon application of uniaxial stress to the semiconductor crystalline sample. This method can provide even higher control of the polarization splitting in combination with an improved strain-tuning device design. In the single photon source core to this thesis about 5% of the emitted single photons are emitted with the V-polarized cavity mode, implying they will be deflected from the collection channel. This rate could be decreased by achieving a larger splitting between the two fundamental cavity modes. Furthermore, a larger mode-splitting would mean that the excitation pulse of light would suffer a smaller amount of spectral filtering by the cavity, approximating the excitation pulse to the textbook Gaussian-pulse description, at the cost of having to operate at higher laser powers.

The highly tunable nature of the device constructed in this thesis opens the possibility to applying the device to different quantum emitters and for a variety of quantum protocols. For instance, GaAs QDs in an AlGaAs matrix emit at wavelengths between 700 nm and 800 nm, an important band coinciding spectrally with rubidium emission lines (795 nm and 780 nm), that are commonly used as a quantum memory.[144] In order to achieve a deterministic storage-and-retrieval of single photons from a QD in a rubidium vapor quantum memory, an enhanced emission of single photons from the GaAs QDs at these wavelengths is essential. Another landmark in quantum networking would be the development of efficient single photon sources at the telecom wavelengths (1300 nm and 1550 nm), where optical fibers present ultra low loss and the necessary infrastructure to transport light is already established world-wide. Should QDs emitting at these wavelengths be developed, our device design could be readily implemented for efficient telecom single photon production.

The current system can be further improved. One could reduce the optical absorption in the gates in the semiconductor heterostructure, with improved design with narrower gates, for instance. However, according to our analysis, the largest source of loss in the system lies not in the "quantum optics", but in the "classical optics" part of the experiment. About 30% of the photons are lost from the QD-cavity system to the output of the optical fiber. A few percent can be readily gained by adding an anti-reflection coating to the glass-air interfaces. This includes the top surface of the silica chip that comprises the top mirror of the cavity and the facets of the optical fibers. A collecting lens with ideally optimized focal length would imply a perfect mode overlap at the fiber input, implying in a 10% gain in photon collection into the fiber. It would be possible to eliminate altogether the cross-polarized microscope, which comprises many optical elements, by implementing an *atom drive* scheme, launching light into the QD via another channel other than the cavity mode. This would allow the elimination of all loss-inducing optical elements in the collection microscope, except for two lenses and the fiber itself, promoting another 12% improvement in single photon transmission through the system.

We propose that the atom drive can be readily achieved with the same semiconductor heterostructure used in this work. Via numerical simulations we predict that a waveguide-like optical mode is formed between the DBR and the sample's surface. The QDs are located in the sample within the extent of this optical mode, so pulses of light traveling in this waveguide could easily be used to excite the QDs. Light can be coupled into this mode in a few ways: one can launch it via the side of the sample, a "lateral excitation"; one can redirect light launched perpendicular to the sample's surface with the help of gratings etched onto the sample; or one can couple light from a tapered fiber placed next to the sample's surface evanescently. This proposal, in addition, opens the possibility of working with a 3-level Λ-system of the QD, in which one arm of the transition is coupled to the cavity. This concept can be implemented by placing a QD spin in a magnetic field. With the atom drive scheme, one would have the capability of initializing the spin and performing spin rotations in the microcavity. In combination with the high photon emission quantum efficiency presented in this work, the precisely clocked spin manipulation would allow for spin-photon entanglement, empowering the creation of an efficient source of cluster-states.[145] In combination with a top mirror with higher reflectivity that allows coherent exciton-photon interaction before the photon escapes the cavity, a photon-photon gate would be within reach.[146]

This work is a landmark in the path to quantum information processing using single photons. It is the first single photon source to surpass a 50% end-to-end efficiency. It operates at high rates, emitting streams of pure single photons with high coherence maintained over unprecedented timescales. The next steps on this journey are promising and exciting: demonstrating quantum advantage in quantum simulation algorithms (for instance with a boson sampling setup), creating cluster-states efficiently and employing them in a universal quantum computer, encoding information into single photons and transmitting them across the world, etc. The future is bright. Bright like photons.

8

ACKNOWLEDGEMENTS

As in every successful endeavor, one never walks the path alone. In fact, I dare to claim that nothing is achieved at all by walking alone. I would like to express my gratitude to the people who, one way or the other, were walking along with me in the past three and a half years, allowing me to reach this moment.

Firstly, I am immensely grateful to my supervisor, Richard Warburton. He has given me the opportunity to join his group, and join an amazing project. He trusted my skills and capabilities in some moments that I myself didn't. He has supported me in the challenging moments in the past years, and encouraged me in the fortunate times. In absolutely every conversation I've had with him I've learned something new, be it about physics or about life. I cannot find better words to describe his contribution to my career and my life than 'mentor' and 'inspiration'.

I am thankful to my colleagues, who worked with me in this project.

I'd like to thank Ben Petrak, who was my first Post-Doc, and the person who introduced me to the initial experimental steps necessary for my project. For teaching me the steps of nanofabrication of the top mirrors, how to mount and align the cavity, and how to escape 40-degree summers by measuring noise spectra in the cold lab. But more than that, for always making the lab a fun place to be.

To my great friend and predecessor in the cavity project, Daniel Najer (a.k.a. Danny-boy). From the start he shared all his knowledge with me with an incredible amount of patience. He taught me how to model cavities, answered my questions with an incredible amount of detail, showed me how to assemble and measure cavities. Without him, I would still be trying to couple light and measure the resonance of a piece of dirt! Towards the end, we had the pleasure – and pain – of working together on the never-ending 'surface-passivation project', and it was a moment of intense emotions. But he has always made it easy and laughable. I will carry in my heart forever the fun moments we had together sharing an office: all the gossips, all the Indian-accent Schwizer-Dütsch conversations, all the physics discussions, all the business ideas, all the cute kids pictures.

I would absolutely not be here without my Post-Doc, Alisa Javadi. I know that wherever his career takes him, he will be successful. He is an incredibly knowledgeable and didactic physicist. I struggle to remember a single question I had, that Alisa wouldn't know the answer to immediately, or, in a very structured manner try to decipher the answer together. He was the person who introduced me to all quantum optics techniques and measurements. He has never denied showing me in a very gentle way how to perform an experiment. More than that, we spent uncountable evenings together measuring single-photon indistinguishabilities until 11 pm, and he was certainly the person keeping my motivation and excitement going. I am so lucky and could not have had a better Post-Doc than him. For that I'm grateful.

I need to thank also Alex Korsch. He was the first Master student I've supervised. It was a challenging new task for me, but that has taught me so much. During his time in our group, we have had numerous measurements, physics discussions and explanations. He was also such an easy person to be around, making work in the lab a pleasant task. I wish him a lot of success in his PhD in the Netherlands and China.

Next, I'd like to acknowledge my girl-pall in the lab, Nadia Antoniadis. First, she joined our project as a Master student when I brought her to "the light side of the force". Again, supervising her was a great learning process for myself. Very quickly it became more than that. We have also spent uncountable hours together aligning optical setups, running between the Mira-laser and lab 3.27, connecting and disconnecting optical fibres, cleaning up the lab and being angry at the mess together. We've become buddies not only with the common goal of having successful and exciting results with our QD-cavity system. We've found each other sharing also gossip, girly talks, beers and cocktails, slow-skiing, politics discussions, southern exaggerated behavior, and much more. I know she will do a great job continuing this project.

To my third Master student, Willy Stehl, with whom I had the pleasure of working on the last mini-project of my PhD. I thank him for being so inquiring and so curious, and for understanding my little availability towards the end of my PhD. Also, I need to thank him for the great taste music played in the lab, while we worked together. I wish him a successful Master thesis ahead!

I cannot appreciate enough the people who shared the office with me: Nadine Leisgang, Viktoria Yurgens and Nam Nguyen. Besides, the people with whom I did not share an office, but at times if felt like it: Jonas Roch, Clemens

Spinnler, Yannik Fontana and Liang Zhai. With all these people I shared daily amounts of coffee/tea, gossip, laughter, support, nuts and snacks, help on each other's projects, cute animal memes, bouldering sessions. These people were many times, especially during Corona times, the only reason I would want to not do home-office. Also, they were so understanding and supportive towards me the entire time, and most specially towards the end of my PhD, with all the drama and stress that came with it.

To the Nano-photonics group as a whole, who has created this very pleasant and friendly work-place. We have shared uncountable beers, coffee breaks, Rhine-swimming, pizzas, cakes, barbecues, game nights, hikes, skiing. Not every working group can have such a amiable atmosphere, supporting each other despite the differences, and I certainly know how to appreciate that we've had this! For this, besides the people mentioned above, I am grateful to Daniel Riedel, Jan-Philipp Jahn, Immo Söllner, Tomek Jakubczyk, Andreas Kuhlmann, Matthias Löbl, Sigurd Flågan, Lukas Sponfeldner, Simon Geyer, Andrea Corazza, Marcel Erbe and Mark Hogg.

Moving on, I'd like to acknowledge the external people with whom I've collaborated in different projects. Firstly, I have to mention Arne Ludwig. Besides growing amazing samples for us, he is one of the most generous professionals I've met, always with kind and optimistic words of incentive. I also must mention Sahand Mahmoodian, who has patiently discussed with us about bound-states of light and whose theory motivated the final experiments of my PhD. I would also like to acknowledge Yizhong Huang, for the pleasant collaboration on coupling rare-Earth ions to open microcavities.

Finally, a warm thanks goes to all the people on my private sphere. To my parents and brothers, for being there for me even from a distance, and for always believing in my capability. To David Martinez-Martín, for being a so-loving and supportive partner, not ever letting me give up on my dreams. To my WG-flatmates, who were my family in Basel, for the constant support and all the good times together. To my old-time friends, who understand my physical absence from their lives and cheer for me – even when they don't understand what I do. To the new friends I've made in the last years, who have made my time in Switzerland a time full of adventure, laughter and comfort. To all the people who somehow have made me who I am and cheered for my success, I am grateful.

Natasha Tomm

Basel, Switzerland, May 2021

List of Publications

- N. Bart, C. Dangel, P. Zajac, N. Spitzer, J. Ritzmann, M. Schmidt, H. G. Babin, R. Schott, S. R. Valentin, S. Scholz, Y. Wang, R. Uppu, D. Najer, M. C. Löbl, N. Tomm, A. Javadi, N. O. Antoniadis, L. Midolo, K. Müller, R. J. Warburton, P. Lodahl, A. D. Wieck, J. J. Finley and A. Ludwig, *Wafer-scale epitaxial positioning of quantum dots*, arXiv:2011.10632 (2020), *submitted*

- N. Tomm, A. R. Korsch, A. Javadi, D. Najer, R. Schott, S. R. Valentin, A. D. Wieck, A. Ludwig and R. J. Warburton, *Tuning the mode splitting of a semiconductor microcavity with uniaxial stress*, Phys. Rev. Appl. **15**, 054061 (2021)

- D. Najer*, N. Tomm*, A. Javadi, A. R. Korsch, B. Petrak, D. Riedel, V. Dolique, S. R. Valentin, R. Schott, A. D. Wieck, A. Ludwig and R. J. Warburton, *Suppression of surface-related loss in a gated semiconductor microcavity*, Phys. Rev. Appl. **15**, 044004 (2021)

- N. Tomm*, A. Javadi*, N. O. Antoniadis, D. Najer, M. C. Löbl, A. R. Korsch, R. Schott, S. R. Valentin, A. D. Wieck, A. Ludwig and R. J. Warburton, *A bright and fast source of coherent single photons*, Nat. Nanotechnol. **16**, 399 (2021)

- N. Tomm*, A. Javadi*, D.Najer* and R. J. Warburton*. (2020). *Single photon source for generating bright and coherent single photons*, European Patent No. EP20187758, *patent pending*

Publications in preparation:

- N. Tomm, S. Mahmoodian, W. Stehl, N. O. Antoniadis, R. Schott, S. R. Valentin, A. D. Wieck, A. Ludwig, A. Javadi and R. J. Warburton, *Direct observation of photon-number dependent Wigner delay from a quantum emitter*, (2021) *in preparation*

- N. Tomm, N. O. Antoniadis, R. Schott, S. R. Valentin, A. D. Wieck, A. Ludwig, R. J. Warburton and A. Javadi, , *Near-ideal extinction in transmission of an artificial atom coupled to a microcavity*, (2021) *in preparation*

- A. Javadi, N. Tomm, N. O. Antoniadis, R. Schott, S. R. Valentin, A. D. Wieck, A. Ludwig and R. J. Warburton, *Cavity-mediated excitation of a quantum dot in the picosecond regime*, (2021) *in preparation*

- N. O. Antoniadis, N. Tomm, R. Schott, S. R. Valentin, A. D. Wieck, A. Ludwig, R. J. Warburton and A. Javadi, *Strong non-reciprocal and non-linear transport of single-photons mediated by a single quantum emitter in a microcavity*, (2021) *in preparation*

Publication prior PhD:

- N. Tomm*, L. Ahnen*, H. Isler*, S. Kleiser, T. Karen, D. Ostojic, M. Wolf and F. Scholkmann, *Characterization of the optical properties of color pastes for the design of optical phantoms mimicking biological tissue*, J. Biophotonics **12**, 4 (2019)

*Equal contribution

Bibliography

[1] Feynman, R. P. Simulating physics with computers. *Int. J. Theor. Phys.* **21**, 467–488 (1982).

[2] Shor, P. W. Polynomial-time algorithms for prime factorization and discrete logarithms on a quantum computer. *SIAM J. Comput.* **26**, 1484–1509 (1997).

[3] Koppens, F. H. L. *et al.* Driven coherent oscillations of a single electron spin in a quantum dot. *Nature* **442**, 776–771 (2006).

[4] Yang, C. H. *et al.* *Nature* **580**, 350–354 (2020).

[5] Leibfried, D., Blatt, R., Monroe, C. & Wineland, D. Quantum dynamics of single trapped ions. *Rev. Mod. Phys.* **75**, 281–324 (2003).

[6] Duan, L.-M. & Monroe, C. Colloquium: Quantum networks with trapped ions. *Rev. Mod. Phys.* **82**, 1209–1224 (2010).

[7] Devoret, M. H. & Schoelkopf, R. J. Superconducting circuits for quantum information: An outlook. *Science* **339**, 1169–1174 (2013).

[8] Senellart, P., Solomon, G. & White, A. High-performance semiconductor quantum-dot single-photon sources. *Nat. Nanotechnol.* **12**, 1026–1039 (2017).

[9] Preskill, J. Quantum computing and the entanglement frontier. *arXiv:1203.5813* (2012).

[10] Arute, F. *et al.* Quantum supremacy using a programmable superconducting processor. *Nature* **574**, 505–510 (2019).

[11] Zhong, H.-S. *et al.* Quantum computational advantage using photons. *Science* **370**, 1460–1463 (2020).

[12] McKeever, J. *et al.* Deterministic generation of single photons from one atom trapped in a cavity. *Science* **303**, 1992–1994 (2004).

[13] Meraner, M. *et al.* Indistinguishable photons from a trapped-ion quantum network node. *Phys. Rev. A* **102**, 052614 (2020).

[14] Doherty, M. W. *et al.* The nitrogen-vacancy colour centre in diamond. *Phys. Rep.* **528**, 1–45 (2013).

[15] Calusine, G., Politi, A. & Awschalom, D. D. Silicon carbide photonic crystal cavities with integrated color centers. *Appl. Phys. Lett.* **105**, 011123 (2014).

[16] Warburton, R. J. *et al.* Optical emission from a charge-tunable quantum ring. *Nature* **405**, 926–929 (2000).

[17] Arcari, M. *et al.* Near-unity coupling efficiency of a quantum emitter to a photonic crystal waveguide. *Phys. Rev. Lett.* **113**, 093603 (2014).

[18] Mirhosseini, M., Sipahigil, A., Kalaee, M. & Painter, O. Superconducting qubit to optical photon transduction. *Nature* **588**, 599–603 (2020).

[19] Fiaschi, N. *et al.* *arXiv:2104.02080* (2021).

[20] Hong, C. K., Ou, Z. Y. & Mandel, L. Measurement of subpicosecond time intervals between two photons by interference. *Phys. Rev. Lett.* **59**, 2044–2046 (1987).

[21] Pan, J.-W. *et al.* Multiphoton entanglement and interferometry. *Rev. Mod. Phys.* **84**, 777–838 (2012).

[22] Kaneda, F. & Kwiat, P. G. High-efficiency single-photon generation via large-scale active time multiplexing. *Sci. Adv.* **5**, eaaw8586 (2019).

[23] Fox, M. *Quantum optics: an introduction* (Oxford University Press, 2006).

[24] Wilk, T., Webster, S. C., Specht, H. P., Rempe, G. & Kuhn, A. Polarization-controlled single photons. *Phys. Rev. Lett.* **98**, 063601 (2007).

[25] Walker, T., Kashanian, S. V., Ward, T. & Keller, M. Improving the indistinguishability of single photons from an ion-cavity system. *Phys. Rev. A* **102**, 032616 (2020).

[26] Aharonovich, I., Englund, D. & Toth, M. Solid-state single-photon emitters. *Nat. Photon.* **10**, 631–641 (2016).

[27] Stranski, I. N. & Krastanov, L. Zur Theorie der orientierten Ausscheidung von Ionenkristallen aufeinander. *Sitz. Ber. Akad. Wiss. Math.-Naturwiss. Kl. Abt. IIb* **146**, 797–810 (1938).

[28] Ediger, M. *et al.* Peculiar many-body effects revealed in the spectroscopy of highly charged quantum dots. *Nat. Phys.* **3**, 774–779 (2007).

[29] Dalgarno, P. A. *et al.* Coulomb interactions in single charged self-assembled quantum dots: Radiative lifetime and recombination energy. *Phys. Rev. B* **77**, 245311 (2008).

[30] Kuhlmann, A. V. *et al.* Charge noise and spin noise in a semiconductor quantum device. *Nat. Phys.* **9**, 570–575 (2013).

[31] Kuhlmann, A. V. *et al.* Transform-limited single photons from a single quantum dot. *Nat. Commun.* **6** (2015).

[32] Kurtsiefer, C., Mayer, S., Zarda, P. & Weinfurter, H. Stable solid-state source of single photons. *Phys. Rev. Lett.* **85**, 290–293 (2000).

[33] Babinec, T. M. *et al.* A diamond nanowire single-photon source. *Nat. Nanotechnol.* **5**, 195–199 (2010).

[34] Sipahigil, A. *et al.* Indistinguishable photons from separated silicon-vacancy centers in diamond. *Phys. Rev. Lett.* **113**, 113602 (2014).

[35] Eliseev, P. G. *et al.* Transition dipole moment of InAs/InGaAs quantum dots from experiments on ultralow-threshold laser diodes. *Appl. Phys.s Lett.* **77**, 262–264 (2000).

[36] Uppu, R. *et al.* Scalable integrated single-photon source. *Sci. Adv.* **6**, eabc8268 (2020).

[37] Javadi, A. *et al.* Single-photon non-linear optics with a quantum dot in a waveguide. *Nat. Commun.* **6**, 8655 (2015).

[38] Tomm, N. *et al.* A bright and fast source of coherent single photons. *Nat. Nanotechnol.* **16**, 399–403 (2021).

[39] Somaschi, N. *et al.* Near-optimal single-photon sources in the solid state. *Nat. Photon.* **10**, 340–345 (2016).

[40] Wang, H. *et al.* Towards optimal single-photon sources from polarized microcavities. *Nat. Photon.* **13**, 770–775 (2019).

[41] Ismail, N., Kores, C. C., Geskus, D. & Pollnau, M. Fabry-pérot resonator: spectral line shapes, generic and related airy distributions, linewidths, finesses, and performance at low or frequency-dependent reflectivity. *Opt. Express* **24**, 16366–16389 (2016).

[42] Cui, G. & Raymer, M. G. Quantum efficiency of single-photon sources in the cavity-QED strong-coupling regime. *Opt. Express* **13**, 9660–9665 (2005).

[43] Iles-Smith, J., McCutcheon, D. P. S., Nazir, A. & Mork, J. Phonon scattering inhibits simultaneous near-unity efficiency and indistinguishability in semiconductor single-photon sources. *Nat. Photon.* **11**, 521 (2017).

[44] Gustin, C. & Hughes, S. Pulsed excitation dynamics in quantum-dot–cavity systems: Limits to optimizing the fidelity of on-demand single-photon sources. *Phys. Rev. B* **98**, 045309 (2018).

[45] Gustin, C. & Hughes, S. Efficient pulse-excitation techniques for single photon sources from quantum dots in optical cavities. *Adv. Quantum Technol.* **3**, 1900073 (2020).

[46] Denning, E. V., Iles-Smith, J., Gregersen, N. & Mork, J. Phonon effects in quantum dot single-photon sources. *Opt. Mater. Express* **10**, 222–239 (2020).

[47] Rahimi-Keshari, S., Ralph, T. C. & Caves, C. M. Sufficient conditions for efficient classical simulation of quantum optics. *Phys. Rev. X* **6**, 021039 (2016).

[48] Wigner, E. On the quantum correction for thermodynamic equilibrium. *Phys. Rev.* **40**, 749–759 (1932).

[49] Nielsen, M. A. Quantum computation by measurement and quantum memory. *Phys. Lett. A* **308**, 96–100 (2003).

[50] Knill, E., Laflamme, R. & Milburn, G. A scheme for efficient quantum computation with linear optics. *Nature* **409**, 46–52 (2001).

[51] Aaronson, S. & Arkhipov, A. The computational complexity of linear optics. *Proceedings of the ACM STOC (New York)* 333–243 (2011).

[52] Reimer, M. E. *et al.* Overcoming power broadening of the quantum dot emission in a pure wurtzite nanowire. *Phys. Rev. B* **93**, 195316 (2016).

[53] García-Patrón, R., Renema, J. J. & Shchesnovich, V. Simulating boson sampling in lossy architectures. *Quantum* **3**, 169 (2019).

[54] Najer, D. *et al.* A gated quantum dot strongly coupled to an optical microcavity. *Nature* **575**, 622–627 (2019).

[55] Lalanne, P., Hugonin, J.-P. & Gèrard, J.-P. Electromagnetic study of the quality factor of pillar microcavities in the small diameter limit. *Appl. Phys. Lett.* **84**, 4726–4728 (2004).

[56] Gregersen, N. *et al.* Numerical and experimental study of the Q factor of high-Q micropillar cavities. *IEEE J. Quantum Electron.* **46**, 1470–1483 (2010).

[57] Wasilewski, Z., Fafard, S. & McCaffrey, J. Size and shape engineering of vertically stacked self-assembled quantum dots. *J. Cryst. Growth* **201-202**, 1131–1135 (1999).

[58] Casey, H. C., Sell, D. D. & Wecht, K. W. Concentration dependence of the absorption coefficient for n- and p-type GaAs between 1.3 and 1.6 eV. *J. Appl. Phys.* **46**, 250–257 (1975).

[59] Najer, D. *et al.* Suppression of surface-related loss in a gated semiconductor microcavity. *Phys. Rev. Appl.* **15**, 044004 (2021).

[60] Guha, B. *et al.* Surface-enhanced gallium arsenide photonic resonator with quality factor of 6×10^6. *Optica* **4**, 218–221 (2017).

[61] Hunger, D., Deutsch, C., Barbour, R. J., Warburton, R. J. & Reichel, J. Laser micro-fabrication of concave, low-roughness features in silica. *AIP Adv.* **2**, 012119 (2012).

[62] Greuter, L. *et al.* A small mode volume tunable microcavity: Development and characterization. *Appl. Phys. Lett.* **105**, 121105 (2014).

[63] Nagourney, W. *Quantum Electronics for Atomic Physics* (2010).

[64] Barbour, R. J. *et al.* A tunable microcavity. *J. Appl. Phys.* **110**, 053107 (2011).

[65] Greuter, L., Starosielec, S., Kuhlmann, A. V. & Warburton, R. J. Towards high-cooperativity strong coupling of a quantum dot in a tunable microcavity. *Phys. Rev. B* **92**, 045302 (2015).

[66] Kuhlmann, A. V. *et al.* A dark-field microscope for background-free detection of resonance fluorescence from single semiconductor quantum dots operating in a set-and-forget mode. *Rev. Sci. Instrum.* **84**, 073905 (2013).

[67] Santori, C., Fattal, D., Vučković, J., Solomon, G. S. & Yamamoto, Y. Indistinguishable photons from a single-photon device. *Nature* **419**, 594 (2002).

[68] Thomas, S. E. *et al.* Bright polarized single-photon source based on a linear dipole. *arXiv:2007.04330* (2021).

[69] Reindl, M. *et al.* Highly indistinguishable single photons from incoherently excited quantum dots. *Phys. Rev. B* **100**, 155420 (2019).

[70] He, Y.-M. *et al.* Coherently driving a single quantum two-level system with dichromatic laser pulses. *Nat. Phys.* **15**, 941 – 946 (2019).

[71] Wei, Y.-J. *et al.* Deterministic and robust generation of single photons from a single quantum dot with 99.5% indistinguishability using adiabatic rapid passage. *Nano Lett.* **14**, 6515–6519 (2014).

[72] Wu, Y. *et al.* Population inversion in a single ingaas quantum dot using the method of adiabatic rapid passage. *Phys. Rev. Lett.* **106**, 067401 (2011).

[73] Wang, D. *et al.* Turning a molecule into a coherent two-level quantum system. *Nat. Phys.* **15**, 483–489 (2019).

[74] Redfield, A. The theory of relaxation processes. vol. 1 of *Advances in Magnetic and Optical Resonance*, 1–32 (Academic Press, 1965).

[75] Breuer, H.-P. & Petruccione, F. *The Theory of Open Quantum Systems* (Oxford University Press, 2002).

[76] Cohen-Tannoudji, C., Dupont-Roc, J. & Grynberg, G. *Atom-Photon interactions: Basic processes and applications* (Wiley, 1998).

[77] Johansson, J., Nation, P. & Nori, F. Qutip: An open-source python framework for the dynamics of open quantum systems. *Comput. Phys. Commun.* **183**, 1760 – 1772 (2012).

[78] Johansson, J., Nation, P. & Nori, F. Qutip 2: A python framework for the dynamics of open quantum systems. *Comput. Phys. Commun.* **184**, 1234 – 1240 (2013).

[79] Reithmaier, J. *et al.* Strong coupling in a single quantum dot-semiconductor microcavity system. *Nature* **432**, 197–200 (2004).

[80] Ding, X. *et al.* On-demand single photons with high extraction efficiency and near-unity indistinguishability from a resonantly driven quantum dot in a micropillar. *Phys. Rev. Lett.* **116**, 020401 (2016).

[81] Yoshie, T. *et al.* Vacuum Rabi splitting with a single quantum dot in a photonic crystal nanocavity. *Nature* **432**, 200–203 (2004).

[82] Kuruma, K., Ota, Y., Kakuda, M., Iwamoto, S. & Arakawa, Y. Surface-passivated high-q gaas photonic crystal nanocavity with quantum dots. *APL Photonics* **5**, 046106 (2020).

[83] Demanet, C. M. & Marais, M. A. A multilayer model for GaAs oxides formed at room temperature in air as deduced from an XPS analysis. *Surf. Interface Anal.* **7**, 13–16 (1985).

[84] Franz, W. Einfluß eines elektrischen Feldes auf eine optische Absorptionskante. *Z. Naturforsc. A* **13**, 484 (1958).

[85] Keldysh, V. L. Behaviour of non-metallic crystals in strong electric fields. *J. Exp. Theor. Phys. (USSR)* **33**, 994 (1957).

[86] Aspnes, D. E. Electric-field effects on optical absorption near thresholds in solids. *Phys. Rev.* **147**, 554–566 (1966).

[87] Hader, J., Linder, N. & Döhler, G. H. k·p theory of the Franz-Keldysh effect. *Phys. Rev. B* **55**, 6960–6974 (1997).

[88] Knupfer, B. *et al.* Polarization-insensitive high-contrast GaAs/AlGaAs waveguide modulator based on the Franz-Keldysh effect. *IEEE Photon. Technol. Lett.* **5**, 1386–1388 (1993).

[89] Liu, J. *et al.* Single self-assembled InAs/GaAsquantum dots in photonic nanostructures: The role of nanofabrication. *Phys. Rev. Appl.* **9**, 064019 (2018).

[90] Xuan, Y., Lin, H. & Ye, P. D. Simplified surface preparation for GaAs passivation using atomic layer-deposited high-κ dielectrics. *IEEE Trans. Electron Devices* **54**, 1811–1817 (2007).

[91] Rebaud, M. *et al.* Chemical treatments for native oxides removal of GaAs wafers. *ECS Trans.* **69**, 243–250 (2015).

[92] Yablonovitch, E., Sandroff, C. J., Bhat, R. & Gmitter, T. Nearly ideal electronic properties of sulfide coated GaAs surfaces. *Appl. Phys. Lett.* **51**, 439–441 (1987).

[93] Ohno, T. Sulfur passivation of GaAs surfaces. *Phys. Rev. B* **44**, 6306–6311 (1991).

[94] Robertson, J., Guo, Y. & Lin, L. Defect state passivation at III-V oxide interfaces for complementary metal–oxide–semiconductor devices. *J. Appl. Phys.* **117**, 112806 (2015).

[95] Carniglia, C. K. & Jensen, D. G. Single-layer model for surface roughness. *Appl. Opt.* **41**, 3167–3171 (2002).

[96] Bennett, J. M. Recent developments in surface roughness characterization. *Meas. Sci. Technol.* **3**, 1119–1127 (1992).

[97] Davies, J. *The Physics of Low-dimensional Semiconductors: An Introduction* (Cambridge University Press, 1997).

[98] Zamora Peredo, L. *et al.* Photoreflectance and Raman study of surface electric states on AlGaAs/GaAs heterostructures. *J. Spectrosc.* **2016**, 1–8 (2016).

[99] Beauville, F. & The VIRGO Collaboration. The VIRGO large mirrors: a challenge for low loss coatings. *Class. Quantum Gravity* **21**, S935–S945 (2004).

[100] Barrett, J., Hardy, L. & Kent, A. No signaling and quantum key distribution. *Phys. Rev. Lett.* **95**, 010503 (2005).

[101] Wang, H. *et al.* Boson sampling with 20 input photons and a 60-mode interferometer in a 10^{14}-dimensional Hilbert space. *Phys. Rev. Lett.* **123**, 250503 (2019).

[102] Wang, J., Sciarrino, F., Laing, A. & Thompson, M. G. Integrated photonic quantum technologies. *Nat. Photon.* **14**, 273–284 (2020).

[103] Raussendorf, R. & Harrington, J. Fault-tolerant quantum computation with high threshold in two dimensions. *Phys. Rev. Lett.* **98**, 190504 (2007).

[104] Sangouard, N. & Zbinden, H. What are single photons good for? *J. Mod. Opt.* **59**, 1458–1464 (2012).

[105] Lodahl, P., Mahmoodian, S. & Stobbe, S. Interfacing single photons and single quantum dots with photonic nanostructures. *Rev. Mod. Phys.* **87**, 347–400 (2015).

[106] Wang, H. *et al.* Near-transform-limited single photons from an efficient solid-state quantum emitter. *Phys. Rev. Lett.* **116**, 213601 (2016).

[107] Santori, C., Fattal, D., Vuckovic, J., Solomon, G. & Yamamoto, Y. Indistinguishable photons from a single-photon device. *Nature* **419**, 594–597 (2002).

[108] Ramsay, A. J. *et al.* Damping of exciton Rabi rotations by acoustic phonons in optically excited InGaAs/GaAs quantum dots. *Phys. Rev. Lett.* **104**, 017402 (2010).

[109] Frey, J. A. *et al.* Electro-optic polarization tuning of microcavities with a single quantum dot. *Opt. Lett.* **43**, 4280–4283 (2018).

[110] Uphoff, M., Brekenfeld, M., Rempe, G. & Ritter, S. Frequency splitting of polarization eigenmodes in microscopic Fabry-Perot cavities. *New J. Phys.* **17** (2015).

[111] Seidl, S. *et al.* Effect of uniaxial stress on excitons in a self-assembled quantum dot. *Appl. Phys. Lett.* **88**, 203113 (2006).

[112] Muller, A. *et al.* Resonance fluorescence from a coherently driven semiconductor quantum dot in a cavity. *Phys. Rev. Lett.* **99**, 187402 (2007).

[113] Chang, D. E., Sorensen, A. S., Demler, E. A. & Lukin, M. D. A single-photon transistor using nanoscale surface plasmons. *Nat. Phys.* **3**, 807–812 (2007).

[114] Schwartz, I. *et al.* Deterministic generation of a cluster state of entangled photons. *Science* **354**, 434–437 (2016).

[115] Dousse, A. *et al.* Ultrabright source of entangled photon pairs. *Nature* **466**, 217–220 (2010).

[116] Liu, J. *et al.* A solid-state source of strongly entangled photon pairs with high brightness and indistinguishability. *Nat. Nanotechnol.* **14**, 586–593 (2019).

[117] Fushman, I. *et al.* Controlled phase shifts with a single quantum dot. *Science* **320**, 769–772 (2008).

[118] Lodahl, P. *et al.* Chiral quantum optics. *Nature* **541**, 473–480 (2017).

[119] Söllner, I. *et al.* Deterministic photon-emitter coupling in chiral photonic circuits. *Nat. Nanotechnol.* **10**, 775–778 (2015).

[120] van Exter, M. P., Jansen van Doorn, A. K. & Woerdman, J. P. Electro-optic effect and birefringence in semiconductor vertical-cavity lasers. *Phys. Rev. A* **56**, 845–853 (1997).

[121] van der Ziel, J. P. & Gossard, A. C. Absorption, refractive index, and birefringence of AlAs-GaAs monolayers. *J. Appl. Phys.* **48**, 3018–3023 (1977).

[122] Raynolds, J. E., Levine, Z. H. & Wilkins, J. W. Strain-induced birefringence in GaAs. *Phys. Rev. B* **51**, 10477–10488 (1995).

[123] Bonato, C. *et al.* Tuning micropillar cavity birefringence by laser induced surface defects. *Appl. Phys. Lett.* **95**, 251104 (2009).

[124] Gerhardt, S. *et al.* Optomechanical tuning of the polarization properties of micropillar cavity systems with embedded quantum dots. *Phys. Rev. B* **101**, 245308 (2020).

[125] Garcia, S., Ferri, F., Ott, K., Reichel, J. & Long, R. Dual-wavelength fiber fabry-perot cavities with engineered birefringence. *Opt. Express* **26**, 22249–22263 (2018).

[126] Rechcińska, K. *et al.* Engineering spin-orbit synthetic hamiltonians in liquid-crystal optical cavities. *Science* **366**, 727–730 (2019).

[127] Zhai, L. *et al.* Large-range frequency tuning of a narrow-linewidth quantum emitter. *Appl. Phys. Lett.* **117**, 083106 (2020).

[128] Nye, J. F. *Physical Properties of Crystals* (Oxford University Press, 1957).

[129] Feldman, A. & Horowitz, D. Dispersion of the piezobirefringence of GaAs. *J. Appl. Phys.* **39**, 5597–5599 (1968).

[130] Adachi, S. GaAs, AlAs, and $\mathrm{Al}_x\mathrm{Ga}_{1-x}\mathrm{As}$: Material parameters for use in research and device applications. *J. Appl. Phys.* **58**, R1–R29 (1985).

[131] Rohatgi, A. Webplotdigitizer: Version 4.3 (2020). URL `https://automeris.io/WebPlotDigitizer`.

[132] Ravindra, N. M., Ganapathy, P. & Choi, J. Energy gap-refractive index relations in semiconductors - an overview. *Infrared Phys. Technol.* **50**, 21–29 (2007).

[133] Blakemore, J. S. Semiconducting and other major properties of Gallium Arsenide. *J. Appl. Phys.* **53**, R123–R181 (1982).

[134] Lourenço, S. A. *et al.* Temperature dependence of optical transitions in AlGaAs. *J. Appl. Phys.* **89**, 6159–6164 (2001).

[135] Bir, G. L. & Pikus, G. E. *Symmetry and strain-induced effects in semiconductors* (Wiley, 1974).

[136] Burenkov, Y. A., Burdukov, Y. M., Davidov, S. Y. & Nikaronov, S. P. Temperature dependences of the elastic constants of Gallium Arsenide. *Sov. Phys. Solid State* **15**, 1175–1177 (1973).

[137] Van de Walle, C. G. Band lineups and deformation potentials in the model-solid theory. *Phys. Rev. B* **39**, 1871–1883 (1989).

[138] Sun, Y., Thompson, S. E. & Nishida, T. Physics of strain effects in semiconductors and metal-oxide-semiconductor field-effect transistors. *J. Appl. Phys.* **101**, 104503 (2007).

[139] Bhargava, R. N. & Nathan, M. I. Stress dependence of photoluminescence in GaAs. *Phys. Rev.* **161**, 695–698 (1967).

[140] Pollak, F. H. & Cardona, M. Piezo-electroreflectance in Ge, GaAs, and Si. *Phys. Rev.* **172**, 816–837 (1968).

[141] Higginbotham, C. W., Cardona, M. & Pollak, F. H. Intrinsic piezobirefringence of Ge, Si, and GaAs. *Phys. Rev.* **184**, 821–829 (1969).

[142] Levine, Z. H., Zhong, H., Wei, S., Allan, D. C. & Wilkins, J. W. Strained silicon: A dielectric-response calculation. *Phys. Rev. B* **45**, 4131–4140 (1992).

[143] Hanschke, L. *et al.* Quantum dot single-photon sources with ultra-low multi-photon probability. *npj Quantum Inf.* **4**, 43 (2018).

[144] Zhai, L. *et al.* Low-noise gaas quantum dots for quantum photonics. *Nat. Commun.* **11**, 4745 (2020).

[145] Lindner, N. H. & Rudolph, T. Proposal for pulsed on-demand sources of photonic cluster state strings. *Phys. Rev. Lett.* **103**, 113602 (2009).

[146] Duan, L.-M. & Kimble, H. J. Scalable photonic quantum computation through cavity-assisted interactions. *Phys. Rev. Lett.* **92**, 127902 (2004).

CURRICULUM VITAE

- 2018-2021, *Ph.D. Physics*
  Universität Basel, Switzerland

- 2014-2016, *M.Sc.(hons) Advanced Optical Technologies*
  Friedrich-Alexander Universität Erlangen-Nürnberg, Germany

- 2010-2014, *B.Sc. Physics*
  Universidade Estadual de Campinas, Brazil